Eidgenössische Technische Hochschule Zürich
Swiss Federal Institute of Technology Zurich

EIDGENÖSSISCHE TECHNISCHE HOCHSCHULE ZÜRICH
FLUXiM AG

MASTER'S THESIS

Hybrid Master Equation Model for Exciton Dynamics in OLEDs

Author:
Simon ZEDER
13-916-291
zeders@student.ethz.ch

Supervisors:
Prof. Dr. Beat RUHSTALLER
CEO FLUXiM AG
beat.ruhstaller@fluxim.com

Prof. Dr. Christoph KIRSCH
ICP ZHAW
kirs@zhaw.ch

Prof. Dr. Ralf HIPTMAIR
SAM ETHZ
ralf.hiptmair@sam.math.ethz.ch

April 9, 2019

Abstract

Organic light emitting diodes (OLEDs) have enjoyed a strong interest in recent years. Such devices have a wide area of application such as flexible and low-cost screens as well as for indoor lighting. If the reverse process is desired organic materials can also be used to create organic photovoltaic devices. In both of these cases molecular excitations, also called excitons, play an extremely important role as they emerge right at the photon-matter interface and therefore determine the interaction of the semiconductor with light. In order to achieve highly efficient organic optoelectronic devices understanding of the exciton dynamics is crucial and is often modeled either in a continuum approximation or by stochastic methods. In both cases the system can be numerically simulated, by discretizing the continuum equations in the former and employing kinetic Monte-Carlo methods in the latter case in order to support the research in this field.

In this work, a different approach will be investigated which can be found somewhere in between continuum models and kinetic Monte-Carlo, namely the formulation of exciton dynamics as Master equations. This Master equation model describes the time-evolution of exciton occupation for each molecule in a 3D grid under the assumption that only strongly localized Frenkel-excitons need to be considered, where the model contains all commonly dominant mechanisms such as (non-)radiative decay, (reverse) inter-system crossing, polaron quenching, triplet-triplet annihilation and generation by charge carrier recombination and optical absorption. Furthermore, transport is modeled as hopping by Förster resonance energy transfer as well as Dexter electron transfer using their physically derived rate expressions. Diagonal disorder is considered as either uncorrelated or correlated Gaussian noise in the local energy levels.

The model is implemented as highly parallelized `C++` code and coupled to a charge carrier simulation using the 1D continuum approach provided by the commercial software setfos. The solver solves for both steady-state using a full Newton iteration algorithm as well as transient conditions where the integration over time is numerically achieved using explicit and implicit Runge-Kutta methods with integrated stepsize control. Some examples are simulated using the new code for both cases where the numerical results show very good agreement with literature. Furthermore, the model is compared to the distinct approach of using a diffusion-based continuum model for excitons which shows the benefits of the Master equation approach, namely very easy modeling of multi-layer devices, spatial resolution of mixed host-guest systems as well as physically more sound transport taking into account asymmetry in the transport rates and interactions beyond the nearest neighbor.

Acknowledgments

First and foremost, I would like to express my gratitude to FLUXiM and especially Prof. Dr. Beat Ruhstaller as its CEO for giving me the opportunity to tackle this project and the autonomy while working on it. It was a new field for me as well as for the company, therefore I am very grateful for all the support and advice I received from my colleges at FLUXiM. Special thanks go to the whole software development team, Andreas Schiller, Alexandre Stous, Roman Hiestand, Oliver Hess and the two newcomers Stefano Weidmann and Yannick Masson for helping me with various programming questions. Special thanks also to Lidia Stepanova, who unfortunately has left the company by now, for making work much more cheerful (and of course also for her technical advice)! Furthermore, I'd like to thank Dr. Urs Aeberhard and Dr. Sandra Jenatsch for always giving me helpful advice about the underlying physical mechanisms.

Very special thanks go to Prof. Dr. Christoph Kirsch from ZHAW, who always was very supportive and helped a lot not only with mathematical and numerical advise, but also with general guidance through the project and very fruitful discussions in our regular meetings. I could count on his support, even for short-notice meetings and visits as well as weekend email conversations when time was running out! Further thanks also go to Prof. Dr. Ralf Hiptmair from ETH Zurich, for supporting my work with many ideas to take into consideration during our regular meetings.

Many thanks also go out to the numerous anonymous contributors to internet-forums clarifying questions about MATLAB, `C++`, LaTeX etc., as well as to my friends for proof-reading some parts of the thesis and to my family for supporting me during this time.

Contents

List of Tables

List of Figures

List of Acronyms & Names

Acronyms

BiCGSTAB	Bi-Conjugate Gradient Stabilized
CDM	Correlated Disorder Model
DD	Drift-Diffusion
DOS	Density of States
DSSC	Dye-Sensitized Solar Cell
EL	Electroluminescence
(E)SDIRK	(Explicit) Singly-Diagonal Implicit Runge-Kutta
ETL	Electron Transport Layer
FL	Fluorescence
GDM	Gaussian Disorder Model
GMRES	Generalized Minimum Residual
HIL	Hole Injection Layer
HOMO	Highest Occupied Molecular Orbital
HTL	Hole Transport Layer
ISC	Inter-System Crossing
IVP	Initial Value Problem
kMC	kinetic Monte-Carlo
LUMO	Lowest Unoccupied Molecular Orbital
ME	Master Equation
ODE	Ordinary Differential Equation
OLED	Organic Light Emitting Diode
OPV	Organic Photovoltaics
PL	Photoluminescence
RK	Runge-Kutta
ROW	Rosenbrock-Wanner
VdW	Van-der-Waals

List of Symbols

Disclaimer: This is not an exhaustive list and symbols which were considered important and are used throughout the thesis are collected here to the best of knowledge.

Symbol	Value / Unit [ ]	Description
$\boldsymbol{A}, \boldsymbol{b}, \hat{\boldsymbol{b}}, \boldsymbol{c}$	–	Runge-Kutta coefficients
$\boldsymbol{c}$	s^{-1}	Constant terms of the Master equation
D	*var*	Diffusion coefficient, Fokker-Planck coefficient
E	J	Energy
E_b	J	Exciton binding energy
E^et	J	Exciton energy
E_F	J	Fermi energy
E_g	J	HOMO-LUMO energy gap
E_mean	J	Mean energy for Gaussian distribution
F	Vm^{-1}	Electric field
$\boldsymbol{f}_\mathrm{nlin}$	s^{-1}	Nonlinear terms of the Master equations
g	–	Generation efficiency
G	s^{-1}	Optical generation rate
h	s	Integration stepsize
$\boldsymbol{J}$	s^{-1}	Jacobian of the Master equations
k_0^D	s^{-1}	Dexter jump-attempt frequency in the zero-distance limit
k_B	$1.381 \times 10^{-23}\,\mathrm{J\,K^{-1}}$	Boltzmann constant
k^F	s^{-1}	Förster rate (later ω^F)
L^D	m	Dexter wavefunction radius
m, m_0	kg	Electron mass
n	–	Refractive index
p	–	Integration method order
$p^\mathrm{s,t,e,h}$	–	Occupation numbers / densities
q	$1.602 \times 10^{-19}\,\mathrm{C}$	Elementary charge
$R, r, \boldsymbol{r}$	m	Distance / radius, location vector
R_0^F	m	Förster radius
R_c	m	Cutoff radius
S_n	–	$\mathrm{n^{th}}$ singlet state
T	K	Temperature
T_n	–	$\mathrm{n^{th}}$ triplet state
V	J	Potential energy

Symbol	Value / Unit [ ]	Description
α	–	Absolute tolerance
β	–	Relative tolerance
β_s	–	Safety factor
$\boldsymbol{\delta}$	–	Relative error
ε_0	$8.854 \times 10^{-12}\,\mathrm{F\,m^{-1}}$	Vacuum permittivity
ε_a	$\mathrm{m^{-1}}$	Absorption coefficient
ε	$\mathrm{F\,m^{-1}}$	Permittivity $\varepsilon_r\varepsilon_0$
ε_r	–	Relative permittivity
η	–	Relative Krylov tolerance
μ	$\mathrm{m^2\,V^{-1}\,s^{-1}}$	Mobility
ξ	J	Random energy
ρ	–	Relative density
σ	J	Gaussian standard deviation
τ	s, –	Lifetime, Newton tolerance
Φ	V	Electric potential
Φ_{im}	V	Image potential
Φ_m	J	Metal workfunction
Ψ	–	Total wavefunction
ψ	–	Electron wavefunction
ω	$\mathrm{s^{-1}}$	State transition rate
$\hbar$	$1.055 \times 10^{-34}\,\mathrm{m^2\,kg\,s^{-1}}$	Reduced Planck constant
∇	–	Gradient operator

Chapter 1

Introduction

In this introductory chapter the motivation for the topic of this thesis is explained. Various applications in real-world problems are shown as well as a short overview over different approaches to modeling exciton dynamics is given. After that, the goals of the project are presented and elaborated in order to understand the resulting structure of the thesis and different challenges that come with those goals. Finally, an overview over the structure of the thesis is given with a short outline about what the different chapters tackle.

1.1 Motivation

Organic semiconducting materials have been attracting a lot of attention over the recent years. As the name suggests, these semiconductors use organic materials as opposed to the already widely used inorganic semiconductors like Si, GaAs, InGaN and many more. While they often have electrically less favorable properties compared to inorganic semiconductors such as charge carrier mobilities, their manufacturing costs are lower and they can be applied in a range of applications such as flexible electronics and optoelectronics. A more detailed description of the properties of organic semiconductors is given in chapter 2 (page 5) along with a more elaborate comparison with inorganic semiconductor materials.

The most interesting use of the organic semiconductors in the scope of this thesis are optoelectronics where the light-matter interaction drives the whole application. The two most famous technologies in this field are most probably organic solar cells where incident photons generate mobile charge carriers which can be extracted and used as a renewable source of energy and the inverse process where an injection of current into an organic semiconductor leads to recombination of oppositely charged carriers releasing a photon and thus producing light. Devices exploiting the latter physical process are commonly denoted as *organic light emitting diodes*, or *OLEDs*, which will be the main focus of this work.

Excitons emerge right at the photon-matter interface and are therefore of utmost importance in understanding and developing such efficient optoelectronic technologies. A more detailed description of the governing physics will be given in chapter 3 on page 25. As the diverse mechanisms and interactions driving these dynamics can be quite complex and often exact analytical laws are only available for very basic or simplified systems, computational methods have to be used to support the development process by numerical simulation. Two major modeling approaches which are used widely are continuum models such as drift-diffusion (DD) models [1, 2, 3] and discrete probabilistic models such as kinetic Monte-Carlo (kMC) [4, 5]. While the DD approach is computationally highly efficient, the models can often not represent exactly the underlying physics. On the other hand, kMC methods can simulate basically any physical process to the desired accuracy given the state transition rates are known, however, they are computationally very expensive.

Exciton simulation using a Master equation (ME) approach can be found somewhere in between the DD and kMC approaches, as the basic model is still probabilistic in nature as in kMC, however, the possible realizations of the system are not explicitly followed but for all states a certain *occupation probability* is calculated. As a result, the method is computationally still more expensive than a DD model, yet cheaper than a full kMC simulation. The feasibility of such a ME approach shall be investigated as an additional tool which can still be used on standard hardware but providing a sounder physical basis than the DD approach.

1.2 Project goals

As already hinted in the preceding section, the main goal of the project is to investigate the feasibility of employing such a 3D-ME approach to model and numerically simulate exciton dynamics in organic semiconductors for OLED applications. An expanded list of objectives is shown below.

- **Write a solver prototype which solves the ME model for exciton dynamics in organic semiconductors.**
  - **Include commonly accepted excitonic and efficiency loss effects like annihilation, polaron quenching etc.**
  - **Solve the resulting model in steady-state as well as in transient conditions.**
- **Analyze the feasibility of such a solver for usage on a “normal” personal computer workstation.**
- **Couple the ME exciton simulation to a DD charge carrier simulation to achieve a hybrid ME-DD solver.**

Master equation models have already been used in modeling organic semiconductors mostly in the scope of charge carrier dynamics, i.e. electron and hole transport by intermolecular hopping (see for example [6, 7, 8]) using the Miller-Abrahams hopping formalism. For exciton migration however, this approach is not yet as widely used, therefore it will be interesting to investigate the possible benefits and drawbacks of such an approach, especially considering the novelty to combine a Master equation simulation for excitons with the well-known DD method for charge carriers.

This coupling will be also of interest, one needs to be aware of the fundamental differences of the two approaches and has to take those into account when combining them. One major difference is of course the mathematical description of the underlying physics, requiring different input data to characterize the system. On the other hand, the numerical differences are also of importance as a DD model is numerically solved very differently from a Master equation model with long-range interactions.

Finally, the results using such an approach should also be compared to the results of a pure 1D-DD approach to identify the similarities and of course the possible advantages and disadvantages of the ME model compared to the DD model.

1.3 Thesis structure

The thesis is generally organized into four parts:

1. Introduction
2. Implementation
3. Numerical description and analysis
4. Results and discussion

In the first part, an introductory overview over the underlying physics is given. This includes the general physical basics of organic semiconductors with a comparison to inorganic semiconductors and relevant physics for some applications (chapter 2). This is followed by a more detailed description of the governing physics regarding exciton dynamics where the relevant processes represented in the model are explained (chapter 3). Both of these chapters rely strongly on the textbooks of Köhler and Bässler [28], Valeur and Berberan-Santos [58] and Schwoerer and Wolf [49]. As already mentioned, this description will lead to the mathematical model where the various processes explained before will be combined to a mathematical model of a system of ordinary differential equations (ODEs) describing the evolution in time of state occupation probabilities. A more detailed look at the resulting model, its properties and auxiliary formulations, such as boundary conditions and disorder models, will be given in chapter 4.

The second part will address the actual code implementation. A schematic overview over the code is given with a description of the most important functions and how the numerical methods are implemented where the details of these methods is then given afterwards. The general workflow on how the code solves the model along with used data structures is explained as well.

As mentioned, the third part of the thesis will be tackling the numerical methods used to actually solve the mathematical models. This part will be mostly split into two sections, a description of methods for solving under steady-state conditions on the one hand (section 6.2) and a description of numerical approaches and stability under transient conditions on the other (section 6.3).

The fourth and final part will deal with the actual results of the simulations. Some examples from literature will be reproduced to check the physical validity of the results and a comparison to a different model (1D-DD) will be examined. This gallery will be split into three sections representing the three different solutions of the model, namely 1D steady-state (section 7.1), 3D steady-state (section 7.2) and 3D transient (section 7.3).

Finally, the performance and usefulness of this ME approach will be examined, and a final conclusion is drawn. Some additional ideas are given regarding the model which could be explored in the future.

Chapter 2

Physical Basis of Organic Semiconductors

In this chapter an overview over the physical basis of organic semiconductors is given for a better understanding of the processes that affect the exciton dynamics which will be described later on. The first section 2.1 will introduce some different types of organic materials used for optoelectronic devices and some examples will be given. Also, the distinct molecular structure of these different materials used as organic semiconductors will be examined and compared to the molecular structure of inorganic semiconductors.

This structure is of high importance to the properties of the material, as it determines the energetic landscape in which not only charged particles such as electrons and holes, but also photons, will move, and therefore gives rise to specific electrical and thermodynamic properties of the material. These resulting electrical properties are discussed in the subsequent section 2.2.

After that, in section 2.3, some experimental methods used to understand and extract certain physical parameters are described, as they give some basic idea on the strength of physical processes which are used as input data for the mathematical systems which describe the physical mechanisms. These are the systems one wishes to solve numerically by using simulation tools.

In the last section 2.4 finally some application-specific physical basics are described. As this thesis is mainly concerned with excitonics, only optoelectronic applications are considered, namely organic solar cells and OLEDs.

2.1 Materials and structure

In this section the materials which are used in organic optoelectronics shall be presented and their molecular structure is discussed. Also, some concepts from organic materials are presented such as positional and energetic disorder and molecular orbitals.

2.1.1 Materials used in organic optoelectronics

As the name suggests, this type of semiconductor consists out of *organic* materials. Organic materials are characterized by a backbone consisting of carbon (C) atoms with an often large number of hydrogen (H) atoms attached to them. However, also other elements are often present in such organic molecules such as nitrogen (N), sulfur (S), oxygen (O) and even metallic elements.

First observations of photoelectric behavior in organic materials already started in the early 20th century using anthracene [9]. Research on using small organic molecules for optoelectronic applications started in the 1950s, when Bernanose published a paper about observed electroluminescence using for example brilliant acridine orange E [10]. Since then, a lot of progress in material design and manufacturing was made, see for example the introduction of vacuum deposition which enabled the manufacturing of very thin electron and hole transport layers in the 1980s [11].

Until the 1980s mostly such small organic molecules were considered. A broad second type of molecules has also been discovered at this time which provided many beneficial characteristics, the type of organic polymers. The use of such polymers like polyacetylene for organic photovoltaics (OPV) started in the 1980s but with still extremely low power conversion efficiencies (<0.1 %). Polymeric materials have also experienced an increased application for OLED devices since the successful use of poly(p-phenylene vinylene) as active layer in a green-yellow OLED [12].

In the following, these two types of molecules are described using some widely used materials for OLEDs and OPV today as examples.

Small molecules

The name "small molecule" comes from the fact that the carbon backbone of the molecule only consists of a short sequence and/or polycyclic aromatic compounds. These materials are normally deposited by vacuum sublimation but may also be processed in solution or dispersion [13].

One such example used for OPV is Phenyl-C61-butyric acid methyl ester (PCBM) and is considered an organic n-type semiconductor material, while Alq_3 is a material used as an electron transport layer (ETL) in OLEDs. The chemical structure of both molecules is depicted in fig. 2.1a and 2.1b, respectively. In both cases the carbon atoms are bonded into a stable individual molecular unit.

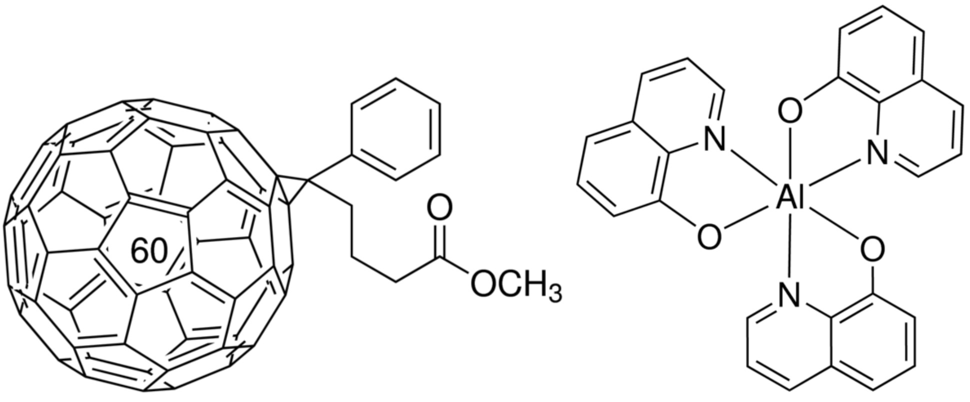

(a) PCBM. **(b)** Alq_3.

Figure 2.1: Molecular structure of two small molecule materials used as semiconductors (Source: Sigma-Aldrich).

Polymers

The second type of organic materials used for OPV and OLEDs are the polymers, which in contrast to the small molecules consist generally of many smaller identical molecular building blocks covalently bonded together forming a very long chain. These long molecular chains show some interesting electrical properties which are not present in small molecules, as will be shown later. These are normally very soluble which enables them being processed in solution and even being printed [13].

Two examples for such materials are given in fig. 2.2. Poly(3-hexylthiophen-2,5-diyl) (P3HT) is a p-type organic semiconductor used in OPV as hole transport (HTL) and hole injection layer (HIL), whereas Poly(3,4-ethylenedioxythiophene)-poly(styrenesulfonate) (PEDOT:PSS), which is actually a mixture of two ionomers, is used as a HIL or even as transparent electrode for OLEDs.

In both cases the figure shows a single building block of the long polymer chain, as denoted by $[\ ]_n$.

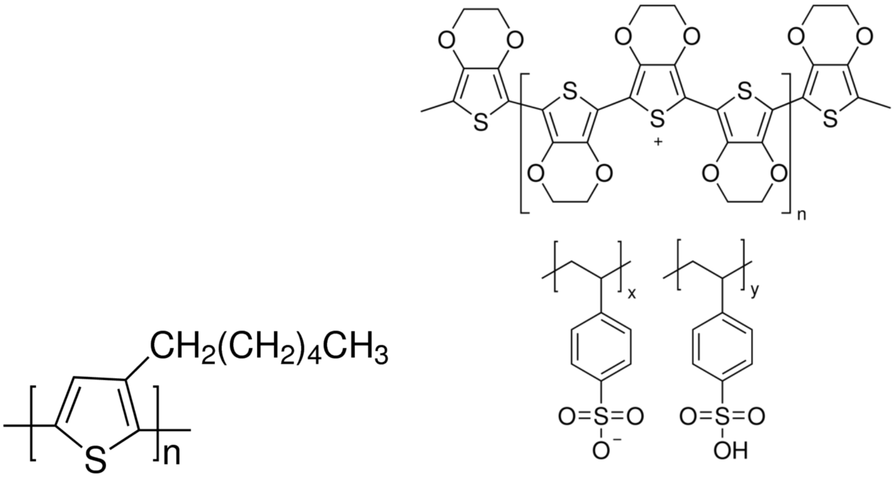

(a) P3HT.

(b) PEDOT:PSS.

Figure 2.2: Molecular structure of two polymer materials used as semiconductors (Source: Sigma-Aldrich).

2.1.2 Supermolecular structure of organic semiconductors

The organization of single molecules in the macroscopic matrix which forms the solid-state material is one of the main differences between organic semiconducting materials and inorganic ones. Inorganic semiconductors in general form covalent bonds (electrons are shared between two atoms) chained together over large scales forming a *well-ordered crystal structure* (see fig. 2.3a), or at least patches of such ordered crystals with imperfect atomic connections at their interfaces (so-called *dangling bonds*). Sometimes inorganic materials are even used in amorphous form, where no such regular crystal lattice exists. These strong covalent bonds on large scales lead to certain macroscopic characteristics such as increased hardness, melting temperature and thermal conductivity.

In contrast to that, organic materials almost always do not form covalent bonds on larger scales, instead, the molecular matrix is held together by *Van-der-Waals* (VdW) or *dispersive* forces (the molecules themselves are of course still made up of covalently bonded atoms). This much weaker interaction is not based on shared electrons, instead, it is an attractive interaction by induced dipoles. Even though the atoms in the organic molecules are electrically neutral and the molecule itself does not carry any permanent electric dipole, random quantum-mechanical fluctuations in electron density can give rise to a temporary electric dipole on the molecule. Through electrostatic interactions this induces an opposite dipole in the neighboring atoms which leads to an attractive force between the two.

At some point this attractive force is overcome by repulsive ones such as quadrupolar interactions and repulsion of electrons due to the Pauli-exclusion principle. This combination leads to an equilibrium distance between the molecules where the energy is minimized. This is often modeled as a *Lennard-Jones potential* [14]:

$$V_{\mathrm{LJ}}(r_{ij}) = -4\epsilon_{\mathrm{LJ}} \left[\left(\frac{\sigma_{LJ}}{r_{ij}} \right)^{6} - \left(\frac{\sigma_{LJ}}{r_{ij}} \right)^{12} \right] \tag{2.1}$$

where σ_{LJ} and ϵ_{LJ} in (2.1) denote the intermolecular distance where $V_{\mathrm{LJ}} = 0$ and the depth of the potential well, respectively. The first term in the bracket represents “long-range” attractive VdW forces, whereas the second term represents the short-range repulsive forces. In conjugated molecules (see section 2.2.1) the intermolecular interactions are often so-called *π–π interactions*, where the π-bonds of two different molecules interact with one another [15]. These π–π interactions, which are very important in organic semiconductors, result in certain specific molecular arrangements. One example of such an arrangement is shown in fig. 2.3b.

2.1.3 Energy levels

One of the most important quantities in physics governing dynamic systems is energy, this of course also applies to charges in organic materials. As a system tends to evolve towards a state with minimum energy, knowledge about the shape of the energetic landscape in a semiconductor is of tremendous interest. First a very quick recap about single-atom energy levels are given followed by an energetic description of a multi-atom system which leads to the LUMO and HOMO, a crucial concept in organic semiconducting materials.

Electronic energy states of a single atom

An electron which moves around an atomic nucleus in equilibrium is described by the *time-independent Schrödinger equation*

$$\hat{H}\psi = E\psi \tag{2.2}$$

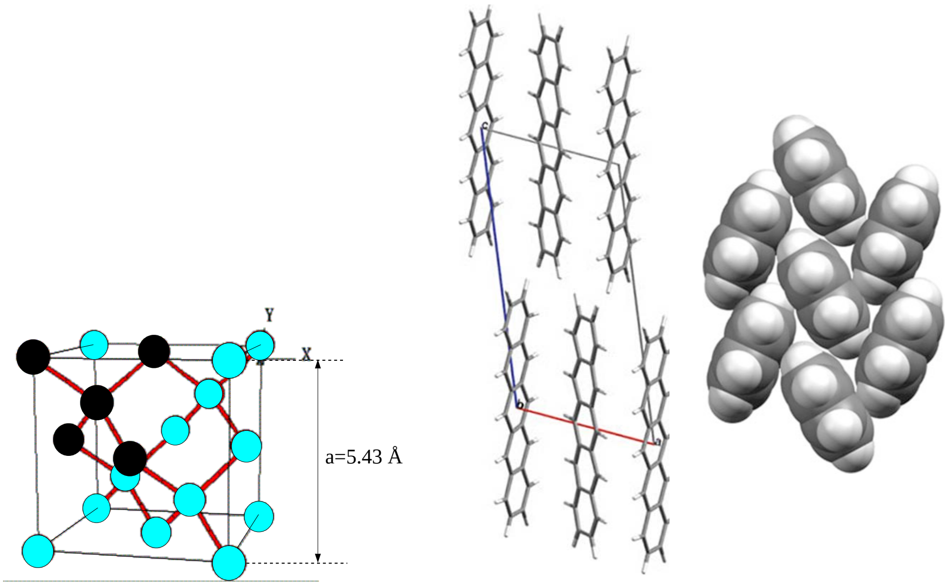

(a) Unit cell of a Si *diamond* structure. Adapted from [16].

(b) Unit cell of a Pentacene *herringbone* structure. Adapted from [17].

Figure 2.3: Comparison of the molecular structures of an inorganic material (Si) and an organic one (Pentacene).

where $\hat{H}$ in (2.2) describes the *Hamiltonian operator*, which in 3D is given by

$$\hat{H} = -\frac{\hbar^2}{2m}\nabla^2 + V(x\,, y,\, z)$$

An easy example showing some important result is the *particle in a box*, where the electron is confined inside a 3D box with equal side lengths a, resulting in a potential which is given by

$$V(x,\, y,\, z) = \begin{cases} 0 & \text{for } -a < x,\, y,\, z < a \\ \infty & \text{otherwise} \end{cases}$$

The solution to the time-independent Schrödinger equation is then given by

$$\psi_{nml} = \sqrt{\frac{8}{a^3}}\sin(\frac{n\pi}{a}x)\sin(\frac{m\pi}{a}y)\sin(\frac{l\pi}{a}z) \tag{2.3}$$

where the boundary condition $\psi = 0$ at the box faces at $-a$, a leads to the result that $n,\, m,\, l \in \mathbb{N}$. Therefore from (2.3) only certain *discrete modes* are allowed. The solution for an actual atomic nucleus behaves similarly, where the potential is then given by the Coulomb potential in spherical coordinates

$$V(r) = -\frac{Zq^2}{4\pi\varepsilon_0 r}$$

with Z the atomic number. After solving again the Schrödinger equation in this case, the solutions will describe the so-called *atomic orbitals* which describe the probability of finding an electron in a certain volume of space by taking $|\psi|^2$. These eigenstates are fully characterized by the three (plus one) quantum numbers n, l and m which represent electron energy, angular momentum and the projection of the angular momentum along a specified axis of the electron. Each orbital characterized in this way can be filled by two electrons due to spin-degeneracy, characterized by the spin quantum number $s = \pm 1/2$. According to the *Aufbau principle*, all these orbitals are filled from lower to higher energies with electrons. Some resulting shapes are depicted in fig. 2.4.

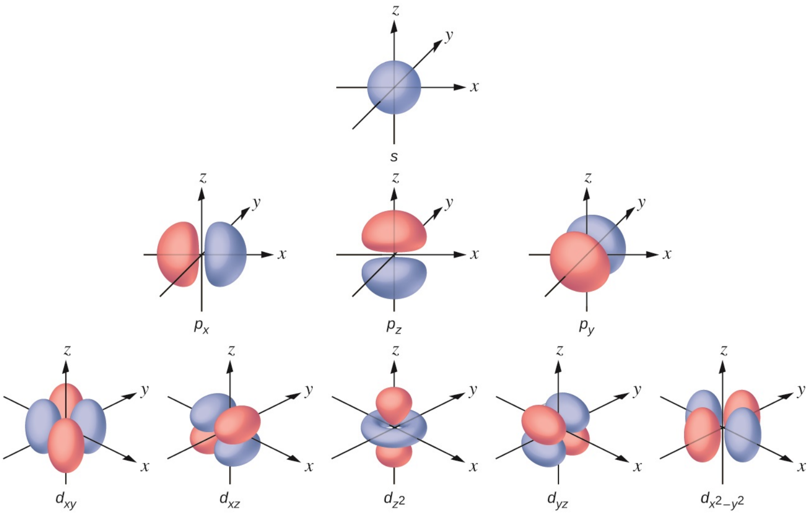

Figure 2.4: Atomic orbitals for an H-like atom. Source: chem.libretexts.org.

Energy states with bonded atoms

Because a material is not comprised out of single independent atoms but rather molecules which consist of many atoms covalently bonded to one another, it is important to go one step further and look at the resulting energy levels when two atoms bond. As already mentioned, covalent bonds result from sharing electrons between two atoms. This can happen when two atoms come together each with an orbital which is incompletely filled (i.e. only one electron). Let's take the simple case of two hydrogen atoms bonding to form an H_2 molecule.

Before a bond forms, a *hybridization* of the atomic orbitals occurs where a new set of orbitals form consisting of linear combinations of the original atomic orbitals. This allows for the adjustment of the geometry to the respective number and types of bonds the atom is engaged in. The bond then forms at an equilibrium distance between the two atoms according to the principle of energy minimization, where the resulting molecular wavefunction is approximated as a linear combination of the atomic orbitals (LCAO approach). As the number of orbitals needs to be conserved, there are two resulting molecular orbitals by taking the linear combination of the two atomic orbitals either in phase (both wavefunctions having the same sign) or out of phase (different sign). This results in an energy splitting, where in the case of the H_2 molecule two $1s$ orbitals with equal energy form a σ-bond (single bond) with a *bonding* (σ) and an *antibonding* (σ^*) state with different energies. This is schematically shown in fig. 2.5.

Another type of bond which is of particular interest in organic semiconductors are π-bonds which are present in double or triple bonds, such as in ethene. These bonds form between p-orbitals which are perpendicular to the bonding axis and therefore, in contrast to σ-bonds, there is no rotational symmetry. Again bonding (π) and antibonding (π^*) states form

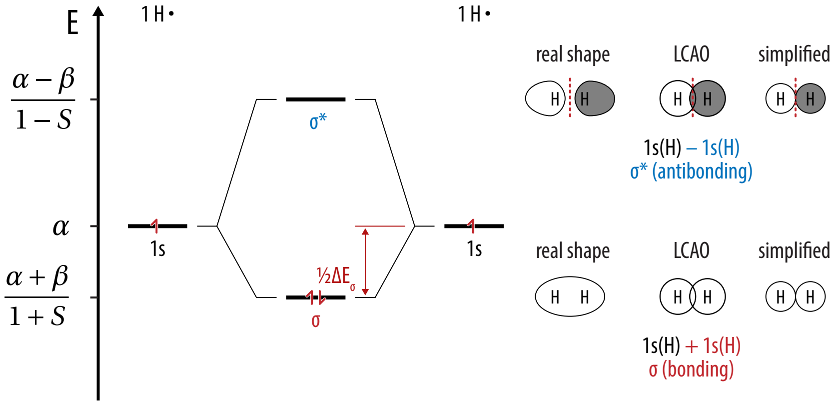

Figure 2.5: Resulting energies for a single σ-bond in H_2. α is the energy of a single s-orbital, β the resonance integral and S the overlap integral. Source: [30].

depending on if the p-orbitals interacting are in or out of phase, where these states lie energetically in between the σ and σ^* states because of the weaker overlap (interaction). The energies of the resulting states for such an ethene double bond (consisting of one σ-bond and one π-bond) are shown in fig. 2.6.

Note again the energy splitting, which is the main point of this explanation. The state with highest energy which is occupied by electrons is called HOMO (highest occupied molecular orbital) and the state with the lowest energy which is still unoccupied by electrons is the so-called LUMO (lowest unoccupied molecular orbital). The energetic difference between them can be seen as the organic pendant to the *bandgap* of inorganic materials which determines e.g. the onset of light absorption and is therefore of utmost importance for optoelectronic applications.

Table 2.1: HOMO – LUMO gaps for some organic semiconductors [18].

Material	$E_{\text{optical gap}}$ [eV]	$E_{\text{HOMO-LUMO}}$ [eV]
Alq_3	2.79	3.07
TPD	3.11	3.81
Anthracene	3.20	3.58

2.1.4 Disorder in organic semiconductors

As explained in section 2.1.2, organic materials often do not feature a highly ordered crystal structure like inorganic materials. While inorganic materials form energetic bands with a very sharp band edge due to the pronounced periodicity and symmetry of the crystal structure, organic materials exhibit *disorder* with energetic states fluctuating around a certain mean energy. There are two types of disorder:

Off-diagonal disorder

This type of disorder results directly from the fact that the organic molecules in the matrix are not perfectly homogeneously arranged in the crystal. This leads to a fluctuation of the

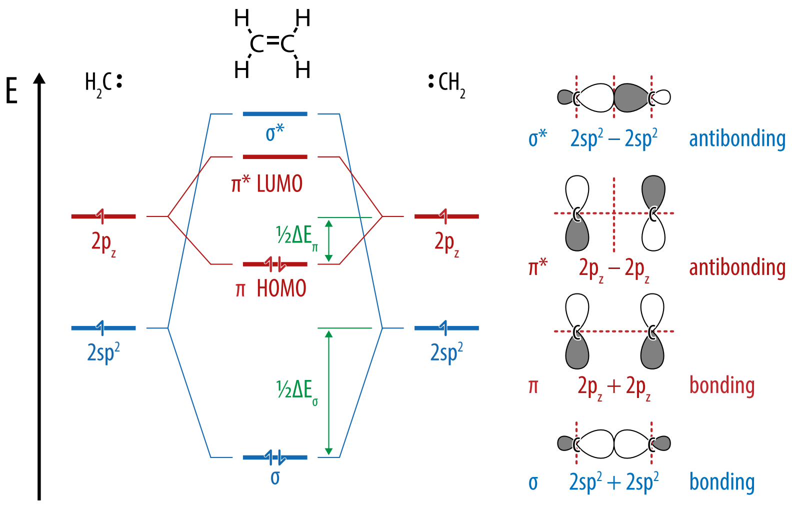

Figure 2.6: Resulting energies for a double bond in C_2H_4 consisting of one σ- and one π-bond. Source: [30].

intermolecular distances and therefore of the wavefunction overlap between adjacent sites [19]. This has a strong impact on charge transport throughout the material.

Diagonal disorder

Diagonal disorder directly affects the local molecular electronic states by altering their energy. This can be induced by the inhomogeneous electrostatic environment due to the already mentioned non-uniformity of the spatial distribution of molecules [20], but also other factors such as variations of molecular conformations and size of conjugated segments, chemical defects, impurities etc. [21].

These fluctuations lead to strongly localized states. Compared to the band-like transport in inorganic semiconductors where the electronic states are strongly delocalized in the conduction band, transport in organic materials is better described by a hopping from one localized state to another. For further details see section 2.2.3.

In general, these fluctuations are modeled by a Gaussian probability distribution [7]

$$g(E) = \frac{1}{\sqrt{2\pi}\sigma} \exp\left(-\frac{(E - E_{\text{mean}})^2}{2\sigma^2}\right) \tag{2.4}$$

While the density of states (DOS) for inorganic materials is commonly approximated using parabolic bands, organic materials commonly use (2.4) as their DOS because of the above-mentioned reasons. Depending on the material this Gaussian distribution can be spatially correlated or not, where the correlation may be induced by the interaction of electric dipoles [22, 23] or thermally induced torsions of the polymer chains [24]. In literature this is commonly called the *Gaussian disorder model* (GDM).

2.2 Electrical properties

Following the last section where molecular concepts of organic semiconductors were introduced, this section will use these findings to discuss some emerging properties of the material when considering interactions between adjacent molecules.

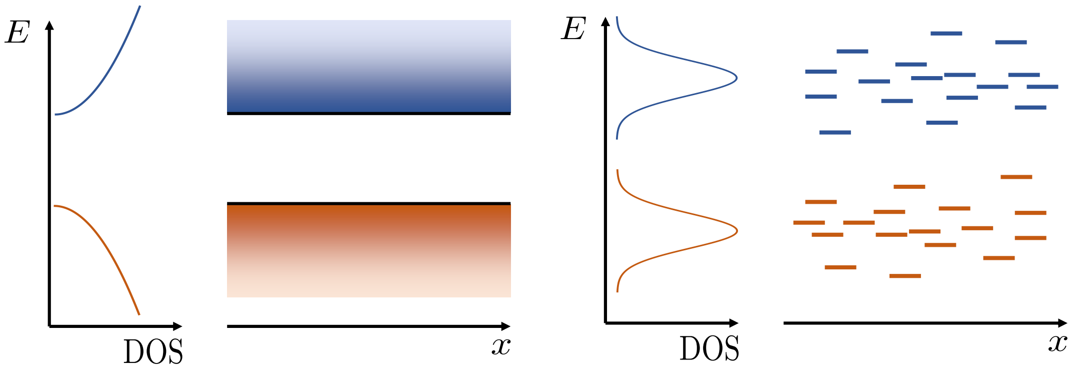

(a) Inorganic semiconductor.

(b) Organic semiconductor with Gaussian disorder.

Figure 2.7: Comparing energy levels and DOS for organic and inorganic semiconductors.

2.2.1 Molecular electron delocalization

As we've seen, the atomic orbitals merge to molecular orbitals when covalent bonds are formed which can be described by taking a linear combination of the atomic orbitals (LCAO). In reality most molecules consist of more than just two atoms and therefore also have many covalent bonds. *Conjugated* π-bonds are a special case, i.e. the case where a molecule features alternating single- and double-/triple-bonds. In such an arrangement, the p-orbitals engaged in the π-bonds line-up along the bond axis and start interacting strongly with one another.

This is not the case for different arrangements! If two double-bonds are located in direct vicinity to one another, the p-orbitals lie perpendicular to one another, and if there are more than one single-bonds in between the double- or triple-bonds, the p-orbitals lie in arbitrary planes to one another. Both of these arrangements lead to none or very limited electronic interaction between the p-orbitals.

There are two different ways how such π-conjugated systems mostly appear in nature, namely linear and cyclic systems (cyclic conjugated systems are also-called *aromatic*) or even polycyclic where cyclic conjugated systems are connected linearly to one another (e.g. tetracene). In all these systems, the resulting bandgap depends on the number of interacting bonds. If one applies the Hückel-approximation [25] the eigenvalues (energies) are given by

$$E_n = \alpha + 2\beta \cos\left(\frac{n\pi}{N+1}\right) \tag{2.5}$$

$$E_n = \alpha + 2\beta \cos\left(\frac{2n\pi}{N}\right) \tag{2.6}$$

where equation (2.5) is valid for the linear and (2.6) for the cyclic case. For both we can see that $\lim_{N\to\infty} \Delta E = 0$, i.e. for very long interacting systems orbitals start to interact strongly and band-like states emerge, where the bandgap also decreases. In the limit of large N, the bandgap vanishes, and the polymer would act like a metal, however, in reality this is prevented as geometric distortion of the molecule will occur prohibiting complete delocalization [26].

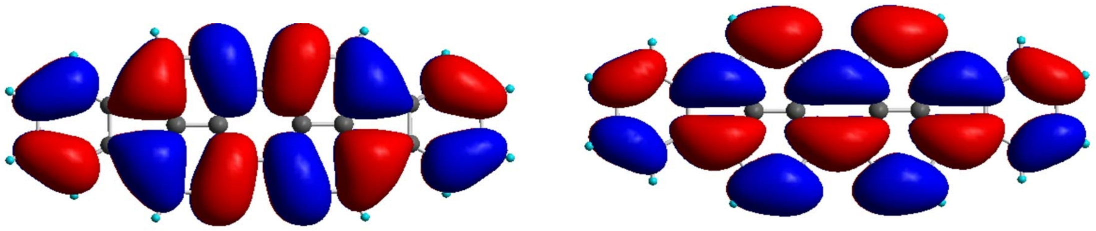

(a) HOMO. **(b)** LUMO.

Figure 2.8: Molecular HOMO and LUMO for DIP. Adapted from [27].

2.2.2 Charge carriers on organic molecules

In order to have electrical conductivity, one needs besides good transport properties also charge carriers which are free to move. To increase the number of mobile carriers, similarly to inorganic semiconductors, organic semiconductors are chemically doped. This is necessary as the energetic gap between HOMO and LUMO is too high in general for thermal activation (see tab. 2.1). During this process, an oxidant (like I_2, AsF_5) for p-type doping or a reductant (like Na, K) for n-type doping are applied to reduce or increase the number of electrons in the molecular orbitals. This is different from the inorganic impurity doping where no chemical reaction takes place and instead an atom at a regular lattice site is replaced.

These added mobile charges influence the molecule and induce geometric changes of the bonds which leads to sharp energy levels in the HOMO – LUMO gap. Therefore, even though the unperturbed π-bonds form very delocalized orbitals, the mobile charge is actually more localized. The combination of charge carrier and its influence on its surroundings through electrostatic interactions is called *polaron* and is an important quasi particle as we will see in the so-called polaron quenching mechanism for excitons in section 3.3.4.

The correlation length (polaron delocalization) of these polarons on the organic molecule is further reduced by the introduced types of disorder (see section 2.1.4). This includes dynamic disorder such as torsion of single σ-bonds at higher temperatures and higher molecular flexibility, as well as static disorder like structural defects.

2.2.3 Electric transport in organic semiconductors

The mobility of charge carriers in a solid-state material is mainly governed by five different terms of the single-electron Hamiltonian, namely

- The electron transfer term H_1 (electronic interaction between two sites)
- The diagonal dynamic disorder term H_2 (vibration induced changes in site energy)
- The off-diagonal dynamic disorder term H_3 (vibration induced changes of the intersite coupling)
- The diagonal static disorder term H_4 (distribution of site energies)
- The off-diagonal static disorder term H_5 (distribution of intersite couplings)

The type of transport regime is then governed by the relative magnitudes of these terms which can be roughly categorized in three types.

Band transport

Band transport is characterized by very strong coupling between transport sites [28], i.e.

$$H_1 > H_2,\, H_3,\, H_4,\, H_5$$

This transport regime is most frequently observed in inorganic molecular crystals at low temperatures due to the long-range homogeneous and periodic structure held together by strong covalent bonds, as this results in widely delocalized coherent Bloch waves throughout the crystal. It can also be observed in highly ordered organic molecular crystals at low temperatures.

The confinement to low temperatures of this type of transport results from the fact that in such an environment the density of phonons is low (low H_2, H_3). A characteristic therefore is a temperature dependency of the mobility of the form

$$\mu \propto T^{-n}$$

as electron-phonon scattering increases with increasing temperature.

Band-like transport

In case where the dynamic off-diagonal disorder increases to the same order of magnitude as the interaction term

$$H_1 \approx H_3$$

the carriers get localized due to thermal motion of the molecules. Transport is therefore achieved by a series of incoherent jumps from site to site, but as dynamic off-diagonal disorder decreases with decreasing temperature and therefore mobility increases it follows again a power law dependence (band-like)

$$\mu \propto T^{-n}$$

Incoherent transport

This type of transport occurs when the dynamic and/or static disorder dominates, i.e.

$$H_1 < H_2,\, H_3,\, H_4,\, H_5$$

Transport is then completely governed by sequential incoherent hopping events between sites. This is a very important transport mechanism in organic materials at elevated temperatures and is also significant then later for exciton transport mechanisms considered in the model. In the case of strong dynamic disorder, *polaronic transport* describes rates as thermally assisted tunneling where the *reorganization energy* λ, which consists of an inner (intramolecular distortion upon charging) and outer (intermolecular displacement and polarization) part, plays an important role, see fig. 2.9. In rigid solid-state we have $\lambda_{\text{inner}} \gg \lambda_{\text{outer}}$. Using *Fermi's golden rule* this leads to transfer rates of the form of the *semiclassical Marcus rate* [29]

$$k = \frac{J^2}{\hbar}\sqrt{\frac{\pi}{\lambda k_B T}}\exp\left(-\frac{\lambda}{4k_B T}\right) \tag{2.7}$$

where J is the electronic coupling element. The hopping rate from (2.7) leads to a mobility of the form

$$\mu \propto (k_B T)^{-\frac{3}{2}}\exp\left(-\frac{\lambda}{4k_B T}\right)$$

which is an Arrhenius type temperature dependence up to $\lambda/4k_BT \ll 1$ from where on it follows the $T^{-3/2}$ dependency.

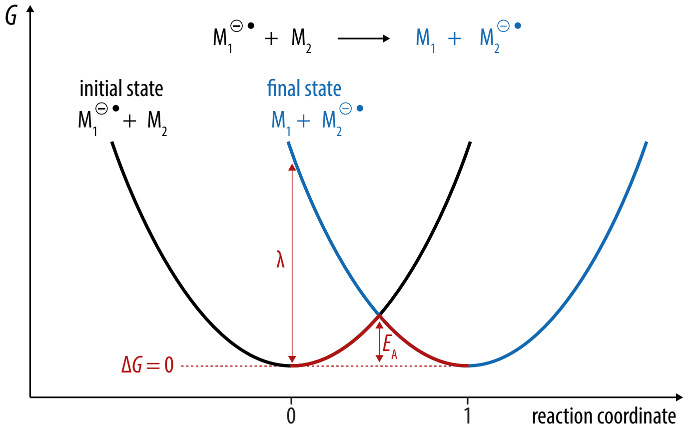

Figure 2.9: Thermally assisted tunneling if no static disorder is present. Adapted from [30].

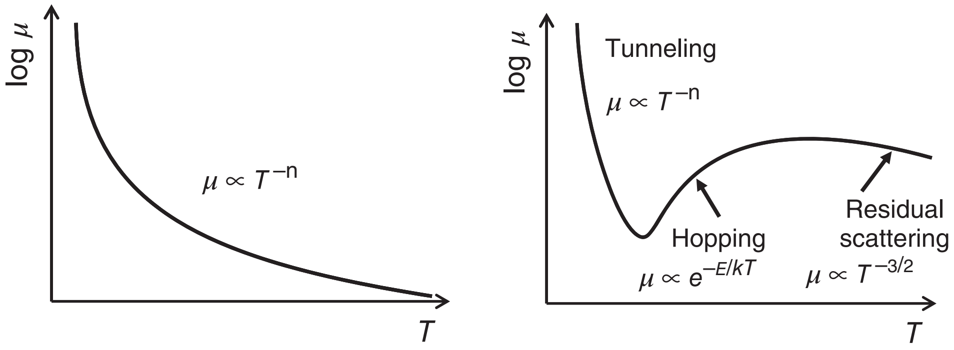

(a) Weak electron-phonon coupling. **(b)** Strong electron-phonon coupling.

Figure 2.10: Transport regimes for different strengths of the electron-phonon coupling. Adapted from [28].

A second type of incoherent transport is the case where static disorder is dominant. Then the energies in the system are described by statistical distributions (often Gaussian, see section 2.1.4) and carrier transport becomes a "random-walk". Because now hops are not energetically symmetric anymore, one needs to introduce a Boltzmann factor if the hop is from lower to higher energy. The electronic coupling can be either a dipole coupling (as will be used for Förster transport rates, see section 3.2.1) or an exchange coupling which is the appropriate choice for charge carriers.

This leads to so-called *Miller-Abrahams* hopping rates [31]

$$w_{ij} = \nu_0 \exp\left(-2\gamma r_{ij}\right) \cdot \begin{cases} \exp\left(-\frac{E_j - E_i}{k_B T}\right) & \text{if } E_j > E_i \\ 1 & \text{if } E_j \leq E_i \end{cases} \tag{2.8}$$

where ν_0 is the hopping prefactor and γ the inverse localization radius of the electron wavefunction.

If such a type of transport model is used with a Gaussian DOS, it can be shown from Monte-Carlo simulations [32] that the mobility follows a non-Arrhenius type dependence

$$\mu \propto \exp\left(-c\left(\frac{\sigma}{k_B T}\right)^2\right)$$

where σ is the width of the Gaussian distribution, and a *Poole-Frenkel* electric field dependence

$$\mu \propto \exp\left(\gamma(T)\sqrt{F}\right)$$

which may be used to model the mobility in the electronic part of the solver used in this thesis. This mobility regime is different from band-transport as mobility increases with increasing temperature instead of decreasing.

2.3 Experimental techniques

In this section a short description of a few experimental techniques is given which are used to determine electron and hole mobilities. Further experimental techniques for different parameters such as HOMO/LUMO levels and recombination will be discussed in section 3.4.

2.3.1 Time-of-flight (TOF)

The simplest experiment is based on the idea of applying a constant DC voltage to a film of the material under investigation. The film is then excited by a laser pulse which generates free charge carriers close to one of the electrodes, where one species of carriers (electrons or holes) is directly captured, while the other one starts moving through the material to the opposite electrode. The initial spike (see fig. 2.11) appears due to relaxation of excess carriers which are not yet in equilibrium with the DOS of the material.

By measuring the mean time of flight for the traveling species the mobility of the material for the respective species can be estimated by

$$\mu = \frac{d}{t_{\mathrm{tr}} F}$$

with d the thickness of the film. However, this method has some drawbacks, especially the fact that thin films cannot be examined by this method because the assumption that the charge carriers are generated completely at one interface is not valid anymore (due to the exponential absorption the resulting charge carrier density will be spatially spread over a significant fraction of the film thickness). Other requirements include time-independent mobility and small RC time constants compared to t_{tr}.

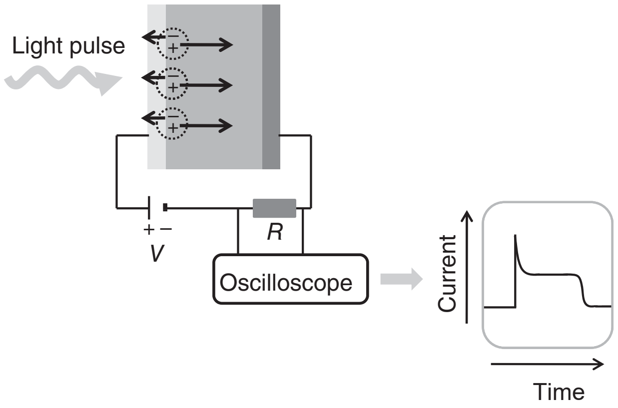

Figure 2.11: Typical TOF experiment. Source: [28].

2.3.2 Charge extraction by linearly increasing voltage (CELIV)

CELIV is an improved method over TOF which can also be applied to thin films as the measurement can also be taken without the need of photoexcitation of carriers. Again, the resulting current transients through a film of the material of interest are measured upon imposed voltage pulses where the voltage now linearly increases.

After discarding measurements from the first voltage pulse (charging of electrodes), the mobility can be calculated using the time until the maximum current flow is reached and the relative change of this maximum current, see fig. 2.12.

$$\mu = \frac{2d^2}{3At_{\max}^2\left(1 + 0.36^{\Delta j}/_{j(0)}\right)}$$

where $A = {}^{\mathrm{d}V}/_{\mathrm{d}t}$ the slope of the voltage transient. Because here charge carriers in equilibrium are probed, relaxation is not an issue and the resulting mobility is more accurate, however, one still needs to be cautious if e.g. the mobility is field dependent or bimolecular recombination is present.

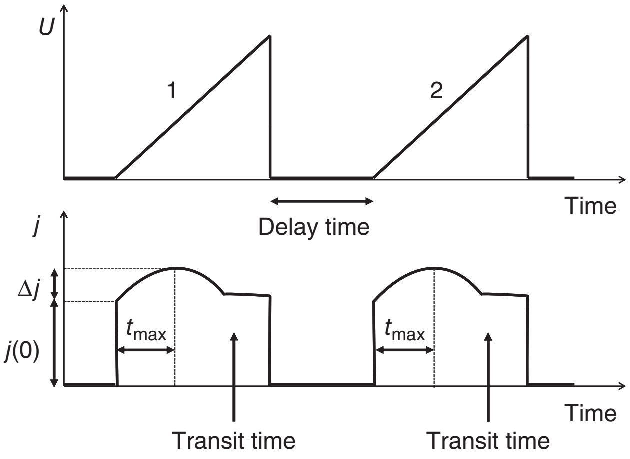

Figure 2.12: Course of a CELIV experiment. Source: [28].

2.4 Applications of organic semiconductors

After discussing some of the basic mechanisms of electronic transport in organic semiconductors some applications of these processes will be presented. The discussion shall be limited to the organic pendant of inorganic LEDs and solar cells, namely OLEDs and OPV, especially as we will see that excitons play a crucial role in both of them.

2.4.1 Organic photovoltaics (OPV)

Photovoltaic generators are widespread today, they are present on roofs, facades and even backpacks. Almost always these are wafers made from crystalline Si which is obvious when considering that Si wafer-based technology still has a market share of $\sim 95\%$ [33]. This is mostly thanks to the abundant availability of Si in nature and the very high efficiencies that can be reached using this material for PV (record cell efficiency 26.7% for mono-crystalline Si [33]).

Organic solar cells cannot (yet) compete with Si cells efficiency wise due to the much lower carrier mobilities, however, they feature other benefits such as the possibility to use thin films of organic material as absorber layers due to high absorption coefficients and therefore allow for cost-efficient roll-to-roll processing. Also, the resulting bandgap (LUMO - HOMO) can be easily tuned by engineering the molecules of the material to have certain features, e.g. length of the conjugated π-systems. Finally, disposal is very easy because of the much lower toxicity of the employed materials. One of the biggest drawbacks of organic cells, however, is the quick cell degradation which is still a difficult challenge and makes extraordinary insulation necessary.

Structure

The general structure of an organic solar cell is similar to the structure of inorganic ones. There is an absorber layer where the main photon absorption takes place combined with an interface for dissociation of electron hole pairs, sandwiched between electrodes made out of metal or metal oxides for transparency.

A typical structure of such an organic solar cell featuring a so-called *bulk heterojunction* is depicted in fig. 2.13a. Light absorption takes place in the absorber layer, where an electron-hole pair is generated which diffuses through the layer until it reaches a donor-acceptor interface where it dissociates. The separated charges then drift to their respective electrodes where they are collected and used to transfer energy. Charge selective layers prevent diffusion of carriers to the wrong electrodes. These processes are explained a bit further in the following.

Light absorption

As mentioned in earlier sections, due to the weaker delocalization of the electron wavefunctions in organic semiconductors, the formation of bands is reduced and only thin bands form. This leads to mostly narrow absorption spectra with a very pronounced and strong

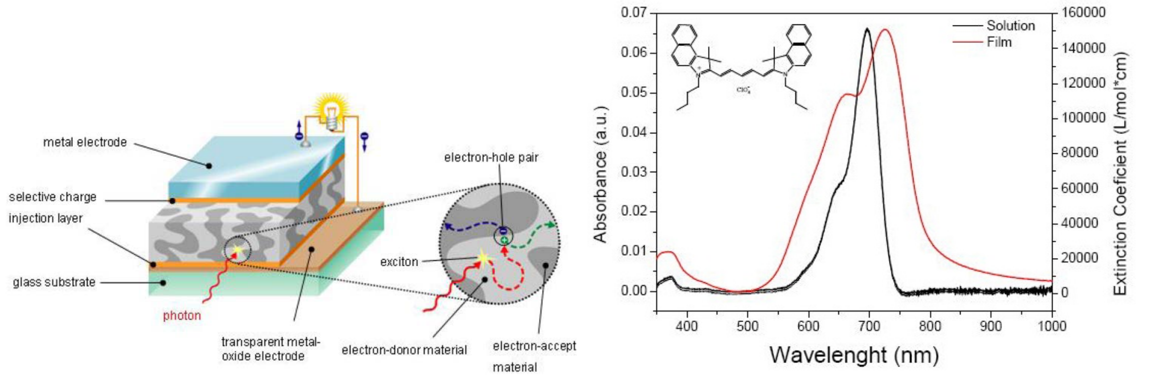

(a) General structure of an OPV cell.

(b) Wavelength dependent extinction coefficient of ICG.

Figure 2.13: Structure and absorption of OPV cells. Adapted from [34].

peak (see fig. 2.13b) compared with inorganic materials where the absorption spectra are much broader due to their large bandwidth.

On the other hand, the extinction coefficient featured by organic absorbers is very high, in the order of $\alpha \sim 10^5$-$10^6\,\mathrm{cm}^{-1}$ compared to inorganic extinction coefficients of $\alpha \sim 10^3$-$10^5\,\mathrm{cm}^{-1}$. This allows for thin films as most of the light is already absorbed after some 100 nm.

After a photon is absorbed, it creates an electron hole pair which is still coulombically bounded. Due to the lower dielectric constant in organic materials, this Coulomb interaction is strong and the binding energy of the pair high. Therefore, the intrinsic electric field is not strong enough to separate the pair into free charge carriers by itself and a charge separating interface is needed.

Charge separation

For this discussion the spatial energy diagram depicted in fig. 2.14a is helpful. The electron-hole pair is generated in the p-type polymer layer and is still strongly bounded. To make sure that the pair dissociates quickly and does not recombine radiatively or non-radiatively, the interface with the electron-accepting material PCBM is spread throughout the absorber layer (bulk heterojunction, compared to planar heterojunction). At the interface, it is energetically favorable for the electron to move into the electron-accepting material due to the lower energy of the LUMO level there, while the hole energetically favors the polymer with the higher HOMO.

One drawback of the bulk heterojunction is the subsequent drift and diffusion of the free carriers to their respective electrodes. Because the paths are intertwined and not well ordered, it can happen that a carrier is trapped in an isolated region or that it recombines again while moving towards its electrode close to the interface, see fig. 2.14b. This architecture is still much better performing than planar heterojunctions, though.

To make sure that carriers do not diffuse to the wrong electrodes where they'd recombine with the opposite charge, charge selective layers are deposited which act as an energetic barrier for the unwanted charge type, preventing its further transport.

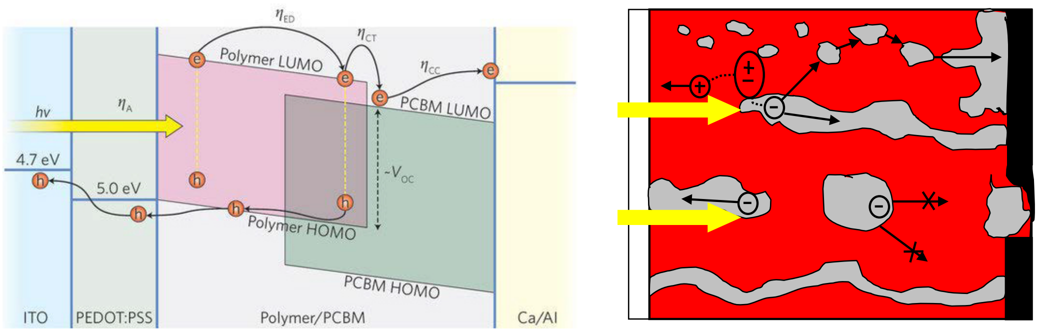

(a) Spatial energetic structure of an OPV cell.

(b) Resulting interfaces for a bulk heterojunction.

Figure 2.14: Energy diagram and interfaces for an OPV cell. Adapted from [34].

Organic - inorganic hybrid cells

As we've seen, both organic and inorganic materials have their distinct benefits and drawbacks. Organic-inorganic hybrid cells try to combine the best of both worlds, namely the good electrical properties like high mobility of inorganic and good optical properties like tunable bandgap and thin film absorption of organic semiconductors. The two most widely known types are dye-sensitized solar cells (DSSC) and perovskite cells.

DSSC

In DSSCs, a porous inorganic semiconductor is coated with an organic small molecule dye as shown in fig. 2.15a. Photon absorption happens in the strongly absorbing organic dye from where the electron is transferred directly over to the inorganic mesoporous material where it begins to move towards the transparent electrode. The hole is transported to the opposite electrode by oxidation of a (usually) liquid organic electrolyte.

Possible recombination can happen by either direct deactivation of the organic dye ("fall back" of the electron), recombination of a conduction electron with an oxidized dye molecule or recombination by reaction with the oxidized electrolyte. Record efficiencies at the moment of up to 15% were achieved where the dye itself is actually composed of a perovskite material (see below) [35].

Perovskite cells

Recently an extraordinary research interest emerged concerning this type of cell as they promise very high possible efficiencies with the record cell efficiency achieved in the lab of 20.9% [36]. The name comes from the particular crystal structure that they share with the basic generic formula ABX_3, depicted in fig. 2.15b. One example of such a material is $CH_3NH_3PbI_3$ (Methylammonium - Lead - Iodide).

Some reasons why perovskite cells perform so well are assumed to be

- High crystallinity and large grains (reduced grain boundary scattering)
- High absorption coefficient
- Long carrier diffusion length $>1\,\mu m$

  - “Intermediate” bandgap between direct and indirect
  - High open-circuit voltage

A big challenge with perovskite cells is their long-term stability as they lose power-conversion efficiency quite quickly. A second challenge are the hysteresis effects in their IV characteristics due to interfacial defects, unbalanced charge transport and migration of slow interstitial ions.

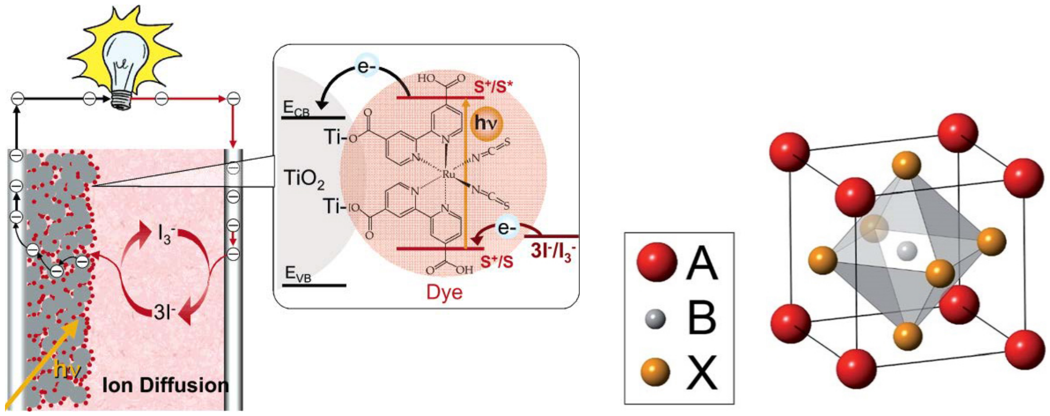

(a) Internal structure of a DSSC. Source: [37].

(b) The generic structure of a perovskite unit cell. Adapted from [38].

Figure 2.15: Structures of organic-inorganic hybrid cells.

2.4.2 Organic light emitting diodes (OLEDs)

While OPV absorbs light and produces a current for electric power generation, an OLED provides the inverse process. A current is injected into an organic semiconductor stack where the carriers recombine and emit photons. These can be used for flexible and high-contrast screens as well as general lighting applications.

Structure

An efficient OLED consists out of a sequence of layers, each specialized for a specific task which increases the performance of the device. Such a stack is depicted in fig. 2.16 alongside its electronic band diagram under bias. There is not one design of such an OLED stack and often less or even more layers (electron/hole blocking layers) are used. In the following the function of these layers is described in the order the carriers move through them from injection at the electrodes to final recombination in the emitter layer.

Charge injection

In order to achieve efficient charge injection, the energetic barrier for the carriers should be low, ideally the LUMO (HOMO) should line up with the metal Fermi-level E_F (equal to the metal work-function Φ_m) at the electron- (hole-) injecting electrode. This is not as easy as it might seem, as upon contact of the semiconductor and metal band bending of the former

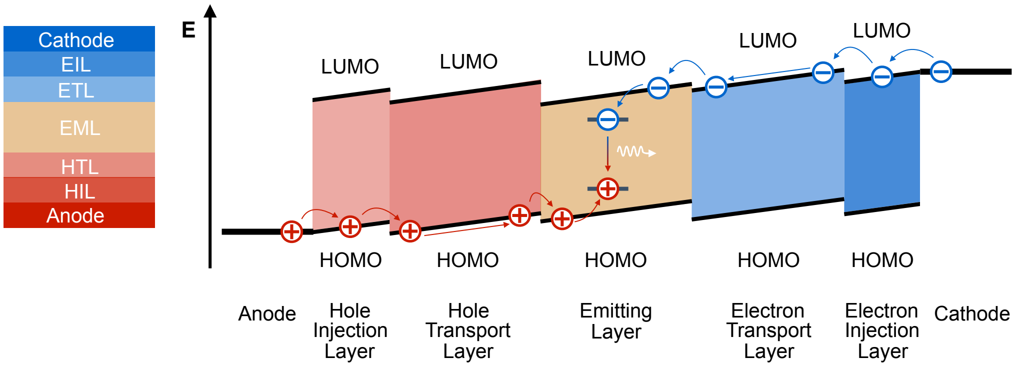

Figure 2.16: Structure of a multilayer OLED. Adapted from [30].

occurs as its E_F aligns with Φ_m. This bending results in a small space charge region also called *diffusion layer* forming a *Schottky*-contact which creates a significant injection barrier. To mitigate this, a thin layer of doped organic semiconductor material is deposited which can decrease the width of the diffusion layer and the energy barrier from LUMO (HOMO) to the aligned E_F which leads to formation of a *quasi-Ohmic* contact by tunneling through the potential barrier (see fig. 2.17 for the case of a hole injection layer).

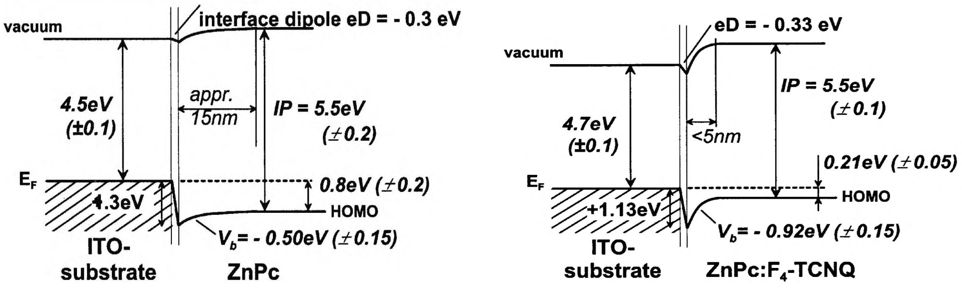

(a) Blocking Schottky contact for undoped organic material.

(b) Quasi-ohmic contact with p-doped organic material.

Figure 2.17: Hole injection for an OLED contact. Adapted from [39]

Transport layers

The following layers after injection are the transport layers. Their main purpose is not simply to transport the carriers as quickly as possible, but instead they try to equilibrate the mobilities. This has the benefit that the zone of recombination is reliably held in the emission layer and is blocked from moving too close to the contacts. Sometimes they also directly take over the role of the blocking layer.

If recombination happens too close to the contacts, strong quenching of the excited states (electron-hole pairs) occurs and starts to compete with the radiative recombination. The efficiency of the OLED is therefore reduced.

Blocking layer

The blocking layers simply assure that the carriers are confined in the emission layer by having a LUMO (HOMO) level which is aligned with the LUMO (HOMO) of the electron (hole) transport layer and the emission layer, while at the same time providing a high energetic barrier for the opposite charge carrier. Additionally, exciton energies are fairly high such that exciton diffusion is also impaired and decay in the emission layer is ensured (see fig. 2.18).

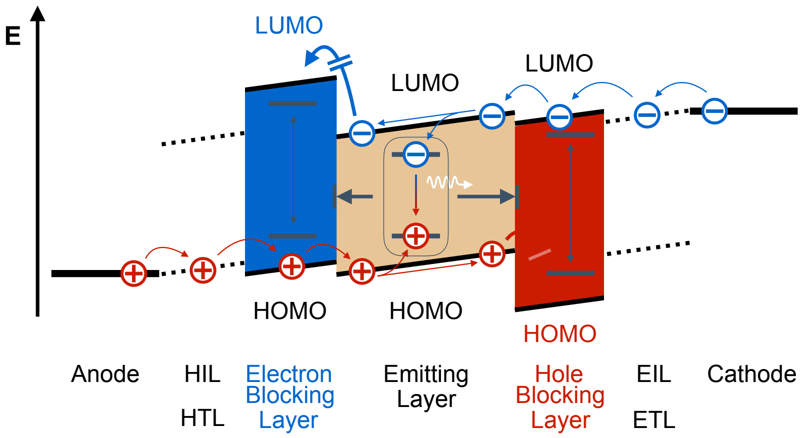

Figure 2.18: Functionality of the blocking layers. Adapted from [30].

Emitter layer

The emitter layer is the final and core layer of the OLED. Here the injected and transported charge carriers recombine and form electron-hole pairs (or excited states, excitons) which should decay radiatively by emission of a photon and thus light. To increase the fraction of radiative decay events, i.e.

$$\eta_{\text{rad}} = \frac{k_{\text{rad}}}{k_{\text{rad}} + k_{\text{nonrad}}}$$

special types of molecules are used. These can be categorized into *phosphorescent emitters* and *thermally activated delayed fluorescence (TADF) emitters*. These two techniques will be explained in more detail in section 3.3.

Chapter 3

Exciton Physics

The name *exciton* has been used already in the context of the optoelectronic applications of organic semiconductors like OPV and OLEDs, however, they have not yet been introduced properly. This chapter will discuss these quasi-particles in more detail, as they are the main focus of the underlying project of this thesis.

The first section 3.1 will introduce the concept of an exciton, what it actually represents physically, which different types of excitons exist and how they are generated in an actual application. The following section 3.2 will start from the point described by section 3.1 and describe the subsequent transport through the material matrix by different physical processes of energy transfer from molecule to molecule. Section 3.3 will then dive deeper into the mechanisms of how such an excited state can change and finally decay over its lifetime in the material. Finally, again some experimental techniques will be described allowing for the measurement of the relative strengths and time constants of these different processes.

3.1 The exciton quasi-particle

The concept of the exciton was first introduced by Frenkel in 1931 when discussing the movement of “excitation packets” upon absorption of a photon by a crystal [40]. To begin the discussion about excitons, the term needs to be properly defined. This starts at the different means of exciton generation and characterization of the different types of excitons as they have quite unique properties. For simplification the abbreviation e^-- h^+pair will be used.

3.1.1 Exciton categorization

An exciton in the general case can be described as an e^-- h^+pair which is coulombically bound. It is therefore from the view of a quasi-particle a *neutral* particle with *integer spin* of either 0 or 1 (i.e. it’s described by Bose-Einstein statistics). For simplicity, from now on the “quasi” will be dropped and the exciton will be described as just a “particle”. The different kinds of excitons can be categorized by different characteristics of the particle from which we will look at two of interest in the definition of the model later, namely *spin-multiplicity* and *magnitude of attraction.*

Let’s start with the ground state of an organic molecule, commonly denoted as $\boldsymbol{S_0}$. This ground state consists in the vast majority of molecules of filled molecular orbitals (states) up to the HOMO with electrons of opposite spin[1]. The excited state of the molecule results if an electron is promoted into states of higher energy, for example the transition of an electron from HOMO to LUMO. As there is no addition or loss of any charge, the molecule is still electrically neutral but bears *potential energy* due to the electron residing in a state with increased energy. Because of the Coulomb attraction between the electron and the hole, they have less energy than free carriers quantified by the *exciton binding energy* E_b. As there are now partially filled orbitals, spins of the electrons do not have to be anti-parallel anymore and two possible configurations arise. If the spins are anti-parallel (net spin 0), the exciton is called a *singlet*, otherwise (net spin 1) it is called a *triplet*. Because there is not only one state per spin-multiplicity, we denote the n$^{\text{th}}$ singlet state by S_n and the n$^{\text{th}}$ triplet state by T_n as shown in fig. 3.1.

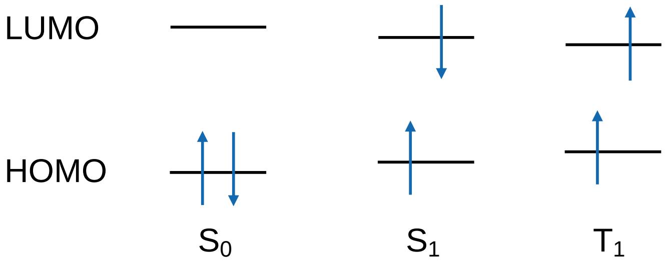

Figure 3.1: Ground, first singlet and first triplet states. Arrows represent electrons with the direction according to the spin. Note the different energies upon excitation.

The second characteristic of an exciton is the strength of the Coulomb attraction between the electron and hole. This mostly depends on the material under consideration, namely its dielectric constant $\varepsilon = \varepsilon_0 \varepsilon_r$ as this reflects the screening of electrostatic interactions due to charges present in the crystal. For large dielectric constants such as in inorganic semiconductors (e.g. $\varepsilon_r = 11.7$ for Si and $\varepsilon_r = 12.9$ for GaAs [41]) the Coulomb interaction between the e^-- h^+pair is strongly screened leading to a largely delocalized exciton with very low E_b. In such a case, where the exciton radius spans multiple unit cells of the crystal, one uses the name *Wannier-Mott* exciton which can be approximately described as a hydrogen-like system where the hole is considered stationary with [42, 43]

$$E_b(n) = \frac{\mu R_H}{m_0 \varepsilon_r^2} \frac{1}{n^2}, \qquad \text{with } \frac{1}{\mu} = \frac{1}{m_e^*} + \frac{1}{m_h^*} \tag{3.1}$$

Equation (3.1) gives the binding energy as a function of the quantum number n (with $n = 1$ the ground state) using the reduced masses m_e^* and m_h^* of the electron and hole, respectively. R_H is the *Rydberg energy* of the hydrogen atom $R_H = 13.6\,\text{eV}$. Due to the high ε_r and small μ compared to the actual hydrogen atom, these energies are much smaller and the exciton radii are much larger than a single unit cell, see table 3.1.

For materials with low ε_r, such as most organic semiconductors (e.g. $\varepsilon_r = 2.4$ - 4 for anthracene [44]), the Coulomb attraction of the e^-- h^+pair is much stronger resulting in strongly localized excitons, often even confined to the same molecule (molecular excitons)

---

[1] A prominent exception of this is molecular oxygen, where the HOMO consists of two degenerate π^*-states with one electron each and both having parallel spins, i.e. the ground state is a triplet state [15].

Table 3.1: Some binding energies and radii for Wannier-Mott excitons in inorganic semiconductors. The gap energies are also given for comparison. Taken from [43].

Semiconductor	E_g [eV]	$E_b(1)$ [meV]	$r_b(1)$ [nm]
GaN	3.5	23	3.1
CdS	2.6	28	2.7
CdSe	1.8	15	5.4
GaAs	1.5	4.2	13
InP	1.4	4.8	12

[45]. Due to the spatial localization, the energy of such an exciton is not accurately described by simply considering the electrostatic interaction of an electron in a Coulomb potential, instead, the overlap of the electron and hole needs to be taken into account as well. Therefore, the energy of such an exciton can be approximated by [46]

$$E_b = \frac{q^2}{4\pi\varepsilon} \iint \frac{\left|\psi_h(\boldsymbol{r}_h)\right|^2 \left|\psi_e(\boldsymbol{r}_e)\right|^2}{\left|\boldsymbol{r}_h - \boldsymbol{r}_e\right|} \mathrm{d}\boldsymbol{r}_h \mathrm{d}\boldsymbol{r}_e \tag{3.2}$$

Note that in (3.2) the actual wavefunctions $\psi_{e,h}$ are present to compute the spatial overlap, which is not the case in (3.1). In this case, the resulting E_b are much larger than for Wannier-Mott excitons (see tab. 3.1), like $\approx 0.4\,\mathrm{eV}$ for PPV [47, 48].

There is also a third case in between the two extremes of Wannier-Mott and Frenkel excitons, the so called *charge-transfer* (CT) excitons, which extend approximately to nearest neighbor molecules. This kind of exciton is of interest in the case of exciton interface dissociation before splitting completely into free carriers, however, these will not be discussed further. A schematic comparison of these three types of excitons is shown in fig. 3.2.

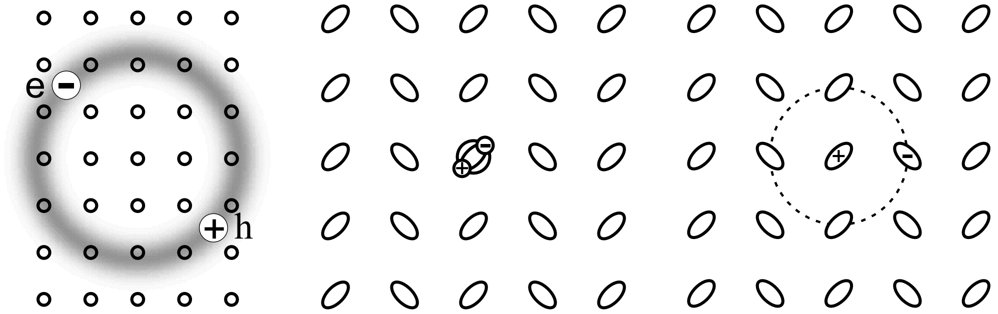

(a) Wannier-Mott exciton.
(b) Frenkel exciton.
(c) CT exciton.

Figure 3.2: Comparison of different exciton types according to their spatial extent. Adapted from [49].

3.1.2 Electrical and optical exciton generation

As the title hints, there are two mechanisms by which an exciton can be generated, *electrically* by recombining electrons and holes and *optically* by interaction of a photon with the electrons in an organic molecule (i.e. its absorption).

The first mechanism occurs due to the electrostatic attraction between a free electron and a free hole moving into each other's vicinity. It can be assumed that one of the carriers resides at a molecule, e.g. at a dopant molecule in the doped emitter layer of an OLED. This molecule will undergo oxidation or reduction when it's charged by a mobile hole or electron, respectively. An approaching electron (or hole) will feel the attraction and approach the charged molecule, up to this moment both carriers are mostly independent from each other, see left side of fig. 3.3. Actual binding will not occur until the charges enter each other's *Coulomb capture radius* which is defined as the distance where the energy of coulombic attraction is equal to the mean thermal energy $k_B T$, this is also approximately true for disordered inorganic materials [50]. The carrier will from then on approach the charged site further followed by formation of a charge transfer state which may be of singlet or triplet nature and the electron and hole wavefunctions will start to overlap, leading to a splitting in energy of the respective singlet or triplet states due to the resulting short-range exchange interaction [51] (see right side of fig. 3.3). This charge transfer state will then quickly decay as the mobile carrier jumps onto the charged site creating a localized neutral Frenkel exciton. This process is generally described as a two-species reaction by the *Langevin* recombination [52]

$$k_{\text{Rec}} = -\gamma n p, \qquad \text{with} \quad \left.\begin{array}{l} \gamma = 4\pi R_{\text{ccr}} \left(D_e + D_h\right) \\ qD = \mu k_B T \\ R_{\text{ccr}} = \frac{q^2}{4\pi\varepsilon_0\varepsilon_r k_B T} \end{array}\right\} \Longrightarrow \gamma = \frac{q}{\varepsilon_0\varepsilon_r}\left(\mu_e + \mu_h\right) \tag{3.3}$$

where the middle equation is the *Einstein relation* between mobility and diffusion constant alongside the expression for the Coulomb capture radius below.

There are some rules which determine the probability of creating a singlet or a triplet exciton. As the electron and hole recombine to form an exciton, their spins can be coupled into four combined states:

$$\left.\begin{array}{r} |\uparrow\uparrow\rangle \\ |\downarrow\downarrow\rangle \\ \frac{1}{\sqrt{2}}\,|\uparrow\downarrow + \downarrow\uparrow\rangle \end{array}\right\} \text{Triplet (symmetric)}$$

$$\left.\frac{1}{\sqrt{2}}\,|\uparrow\downarrow - \downarrow\uparrow\rangle \right\} \text{Singlet (anti-symmetric)}$$

As in the statistical limit all of these four states have the same probability of getting formed, 75% of the excitons generated by e^-- h^+recombination will be triplets and only 25% will be singlets [30].

The second way an exciton can be created is optically by absorption of a photon. The electromagnetic wave represented by the photon drives oscillations of the electrons in the molecular orbitals. The strength of these oscillations is related to the polarizability α by defining the induced dipoles

$$\boldsymbol{p} = \alpha \boldsymbol{F} = q\boldsymbol{\delta r} \tag{3.4}$$

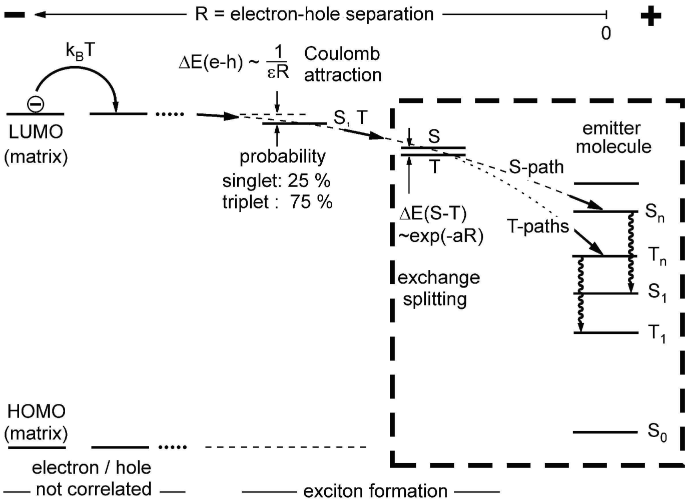

Figure 3.3: Process of recombinative exciton generation. Adapted from [51].

where α is usually high in π-conjugated systems and therefore absorption is strong [30]. The quantum mechanical transition rate is related to the square of the *transition dipole moment* $k = \frac{2\pi}{\hbar} \left|\mu_{fi}\right|^2 \rho$ [28] where this moment for the total two-electron system is given by

$$\mu_{fi} = \langle \psi_f \left| \hat{\mu} \right| \psi_i \rangle = \int \psi_f^* \hat{\mu} \psi_i \mathrm{d}^3\boldsymbol{r} = \int \psi_f^*(\boldsymbol{r}_1, \boldsymbol{r}_2) \left(-q\boldsymbol{r}_1 - q\boldsymbol{r}_2\right) \psi_i(\boldsymbol{r}_1, \boldsymbol{r}_2) \mathrm{d}^3\boldsymbol{r} \tag{3.5}$$

It is evident that the dipole moment operator $\hat{\mu}$ is symmetric under particle exchange whereas the (spatial) wavefunctions for the two-electron system might be symmetric or antisymmetric, i.e.

$$\psi_{\pm} = \frac{1}{\sqrt{2}} \left(\psi_1\psi_2 \pm \psi_2\psi_1\right)$$

and therefore there are only two allowed transitions from (3.5) with $\mu_{fi} \neq 0$, namely when both spatial wavefunctions ψ_i and ψ_f are either symmetric or antisymmetric. Furthermore, the Pauli exclusion principle demands that the *total wavefunction* $\Psi = \psi\sigma_{\text{spin}}$ consisting of the spatial and spin part is antisymmetric under particle exchange and therefore the spin part needs to have opposite parity of the spatial part [43]. The conclusion is that optical transitions need to conserve total spin as the photon carries no angular momentum (as the spatial parts of the total wavefunction have same symmetry, the spin parts also must have the same (reversed) symmetry), therefore optical excitation is only allowed for singlet to singlet or triplet to triplet states (compare to the 25% – 75% for electric excitation)! However, this is not the final truth as will be shown when discussing phosphorescence in section 3.3.1.

A more comprehensive view of the single electron transition is given by including the vibrational energy of the ground and excited states [30]

$$\mu_{fi} = \left\langle \psi_f^e \psi_f^v \Sigma_f \left| \hat{\mu} \right| \psi_i^e \psi_i^v \Sigma_i \right\rangle \underset{\text{BO}}{\simeq} \left\langle \psi_f^e \left| \hat{\mu} \right| \psi_i^e \right\rangle \left\langle \psi_f^v \middle| \psi_i^v \right\rangle \left\langle \Sigma_f \middle| \Sigma_i \right\rangle \tag{3.6}$$

where BO stands for the Born-Oppenheimer approximation that the electron motion can be separated from the nuclear (vibrational) motion. The first term in (3.6) stands for the spatial overlap, the last for the unchanging spin, as already discussed above and the middle term for the vibrational overlap. Note that here $\hat{\mu}(\boldsymbol{r}) = -q\boldsymbol{r}$, which is *spatially* antisymmetric which leads to the condition that *single electron wavefunctions* ψ_f^e and ψ_i^e must have *opposite* parity (dipole-allowed), otherwise this first term becomes 0 (dipole-forbidden) [28].

These terms can be nicely illustrated in a diagram of the vibrational levels in two Morse potentials corresponding to the ground and excited states. The Franck-Condon principle says that the electronic transition is much faster than the adjustment of molecular arrangement, therefore transitions are vertical from the ground state to the vibrational state of the excited molecule which resembles the ground arrangement the most, see fig. 3.4 [53, 54, 55].

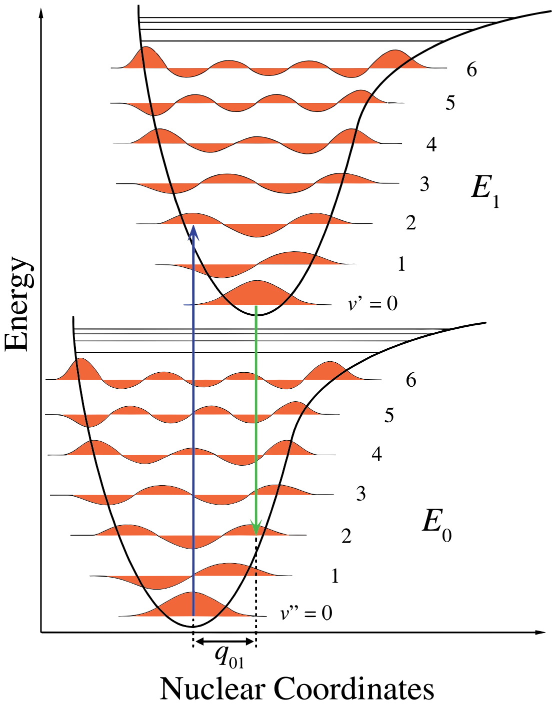

Figure 3.4: Optical transitions according to the Franck-Condon principle (vertical transitions). After excitation, the excited molecule relaxes to the lowest vibrational state. Upon relaxation and photon emission, transition energy is lower leading to a Stokes-shift. Source: [56].

3.2 Exciton transport

Even though excitations in organic materials are commonly strongly localized Frenkel excitons, they are not doomed to stay at their molecule and wait for their inevitable eventual decay. For such strongly localized excitons there are two main mechanisms of transport (apart of course from the possibility to radiatively decay with subsequent absorption again somewhere else), namely *Förster resonance energy transfer* (FRET) or just Förster transport in short and *Dexter electron transfer* or just Dexter transport in short.

In general, to analyze transport one can again use Fermi's golden rule where we need the interaction energy between initial and final states of the complete donor-acceptor system

$$\beta = \left\langle \Psi_f \middle| \hat{H} \middle| \Psi_i \right\rangle \tag{3.7}$$

where (electrons indistinguishable)

$$\begin{aligned}\Psi_i &= \frac{1}{\sqrt{2}}\left(\Psi_D^*(1)\Psi_A(2) + \Psi_D^*(2)\Psi_A(1)\right)\\ \Psi_f &= \frac{1}{\sqrt{2}}\left(\Psi_D(1)\Psi_A^*(2) + \Psi_D(2)\Psi_A^*(1)\right)\end{aligned} \tag{3.8}$$

where the superscript * denotes an excited state, which finally results in two interaction energy terms by using (3.8) in (3.7) and simplifying

$$\beta = \underbrace{\left\langle \Psi_D(1)\Psi_A^*(2) \middle| \hat{H} \middle| \Psi_D^*(1)\Psi_A(2) \right\rangle}_{\beta^C} - \underbrace{\left\langle \Psi_D(1)\Psi_A^*(2) \middle| \hat{H} \middle| \Psi_D^*(2)\Psi_A(1) \right\rangle}_{\beta^E} \tag{3.9}$$

where the first term in (3.9) describes a Coulomb term where the electrons stay at their respective molecules, while the second term describes an exchange term where electrons are actually transferred [28].

3.2.1 Förster resonance energy transfer

The first type of exciton transfer described is the Förster transport mechanism and corresponds to the coulombic term in (3.9). Förster approximated the coulombic interaction energy by a dipole-dipole interaction between the two molecules [57] which is defined by the transition dipole moments proportional to r^{-3}. These interaction dipole moments were expressed by various other physical quantities such that the final rate of Förster energy transfer reads

$$k^F = \frac{9\ln(10)}{N_A}\frac{\Phi_D \kappa^2}{128\pi^5 n^4 \tau_D^0 R^6}\int I_D(\lambda)\varepsilon_A(\lambda)\lambda^4 \mathrm{d}\lambda = \frac{1}{\tau_D^0}\left(\frac{R_0^F}{R}\right)^6 \tag{3.10}$$

with N_A Avogadro's number, Φ_D the donor FL quantum yield far away from the acceptor, κ an orientation factor, n the refractive index, τ_D^0 the decay rate of the donor excitation *in absence of the acceptor* (i.e. no Förster interaction), I_D the normalized donor emission spectrum and ε_A the acceptor absorption coefficient. The simpler expression aggregates many terms into one parameter R_0^F, the *Förster radius.*

Förster transfer is considered long-range with $R_0^F \leq 10\,\mathrm{nm}$ [58] where this corresponds to the distance for which Förster transport is equally likely as relaxation in absence of the acceptor molecule. From (3.10) it is evident that for strong Förster transport the emission spectrum of the donor has to largely overlap with the absorption spectrum of the acceptor. Therefore, in OLED design dopants in the emitter layer are chosen such that their absorption matches the emission of the host.

Note that if one splits the wavefunction in β^C into an electronic and spin part $\Psi = \Psi^e\Psi^\Sigma$ in (3.9) one gets two terms of the spin integral for each electron on its respective molecule in its excited and ground state [28]. Therefore, ground and excited state need to have same spin multiplicity which excludes triplets from Förster transfer (as normally the ground state is a singlet state), except for some organometallic complexes (see section 3.3.3) [59] or of course for already excited triplets to higher triplet states.

3.2.2 Dexter electron transfer

The second type of excitation energy transport is by Dexter electron transfer first introduced by Dexter [60] which is described by the exchange term β^E from (3.9) including the transfer of an actual electron between two molecules. Therefore, if one uses the same approach as above by splitting $\Psi = \Psi^e \Psi^\Sigma$ in β^E the spin integral now does not couple the relaxed and exited states on the same molecule, instead, the coupling is between the molecules for the respective excitation states. Therefore, to have $\left\langle \Psi_D^\Sigma \middle| \Psi_A^\Sigma \right\rangle \neq 0$ (and reversed for the excited states) there needs to exist some spatial overlap of the wavefunctions and this unavoidably restricts Dexter transport to very short ranges [61] (typically $<10\,\text{Å}$ [17]).

As was already used in the Miller-Abrahams electron hopping rates (2.8) in section 2.2.3, an exchange interaction is described by an exponential decay term. Therefore, the rate for Dexter transport is commonly given by [58]

$$k^D = \frac{2\pi}{h} K J' \exp\left(-\frac{2R}{L_D}\right), \quad \text{with } J' = \int I_D(\lambda)\varepsilon_A(\lambda)\mathrm{d}\lambda \tag{3.11}$$

where K is a constant, L_D is the sum of the VdW radii of the donor and the acceptor and both $I_D(\lambda)$ and $\varepsilon_A(\lambda)$ are normalized (i.e. the rate is independent of oscillator strength of both molecules, in contrast to Förster transport [62]). Here K does not correspond to any clear experimentally measurable quantities, therefore k^D is much harder to quantify than k^F.

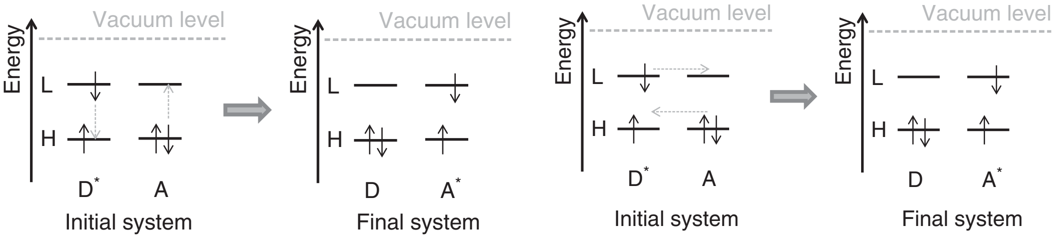

(a) Förster transport mechanism. **(b)** Dexter transport mechanism.

Figure 3.5: Excitation energy transport mechanisms. Source: [28].

3.3 Exciton-altering processes

After creation of an exciton by photon absorption or charge carrier recombination with potential subsequent transport through the material, the excitation will eventually undergo a change of state. This can be either a relaxation back to the ground state radiatively or non-radiatively, dissociation of the e^-- h^+pair into free charge carriers or even change from one type of exciton to another. These processes shall be discussed in this chapter where an overview over some is given in fig. 3.6.

3.3.1 Radiative decay

The first process described in this section is the radiative decay (relaxation) of the excited state back to its ground state, which is the desired process in an OLED device. The result

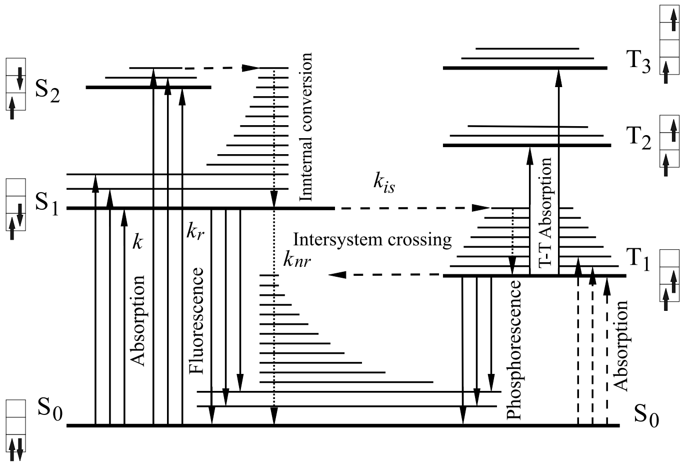

Figure 3.6: Jabłoński diagram for excitonic processes. Energy is plotted on the vertical, spin-multiplicity on the horizontal axis. Horizontal lines represent excitonic states with their respective vibrational energy levels. Source: [49].

is an emission of photons (light) where the phenomenon can be classified according to the origin of the exciton, namely *photoluminescence* (PL) and *electroluminescence* (EL) where in the former case the excitation originates from the absorption of incident photons (e.g. in luminous paint) and from e^-- h^+recombination in the latter (e.g. in an OLED). A second way to classify radiative decay is by its governing time constants, *fluorescence* for very rapid and *phosphorescence* for much slower decay. As already discussed, in most cases the ground state of a molecule is the singlet state S_0 and therefore fluorescence and phosphorescence will correspond to the decay of an excited singlet and triplet state, respectively:

$$\begin{aligned} S^1 &\to S^0 + h\nu \quad \text{Fluorescence} \\ T^1 &\to S^0 + h\nu \quad \text{Phosphorescence} \end{aligned}$$

The observant reader might wonder how this phosphorescent decay is possible as it was shown in section 3.1.2 that optical transitions need to conserve spin which would make phosphorescence a spin-forbidden process! The answer lies in the fact that total angular momentum has to be conserved which can be achieved even under change in spin by *spin-orbit coupling* which introduces a perturbation leading to mixing of triplet and singlet states [28]

$$\begin{aligned} \left|{}^3\Psi_1'\right\rangle &= \left|{}^3\Psi_1^0\right\rangle + \sum_k \frac{\left\langle {}^1\Psi_k^0 \middle| \hat{H}_{SO} \middle| {}^3\Psi_1^0 \right\rangle}{E(T_1) - E(S_k)} \left|{}^1\Psi_k^0\right\rangle \\ \left|{}^1\Psi_0'\right\rangle &= \left|{}^1\Psi_0^0\right\rangle + \sum_k \frac{\left\langle {}^3\Psi_k^0 \middle| \hat{H}_{SO} \middle| {}^1\Psi_0^0 \right\rangle}{E(S_0) - E(T_k)} \left|{}^3\Psi_k^0\right\rangle \end{aligned} \tag{3.12}$$

where the left superscript denotes spin-multiplicity (1 = singlet, 3 = triplet), the right superscript purity (0 = pure state, ' = mixed state) and the subscript the quantum number (0 = ground state etc.). These can then be used in Fermi's golden rule

$$k = \frac{2\pi}{\hbar} \left| \left\langle {}^3\Psi_1' \right| q\boldsymbol{r} \left| {}^1\Psi_0' \right\rangle \right|^2$$

which gives a nonzero probability of radiative triplet decay. This is used in *phosphorescent emitter* materials by using organometallic complexes with a heavy-metal atom leading to strong spin-orbit coupling (see for example fig. 3.7a) in order to circumvent the 25% limit from electrical exciton generation if only singlets would decay radiatively, leading to ≈ 100% internal quantum efficiency (η_{int}) [63].

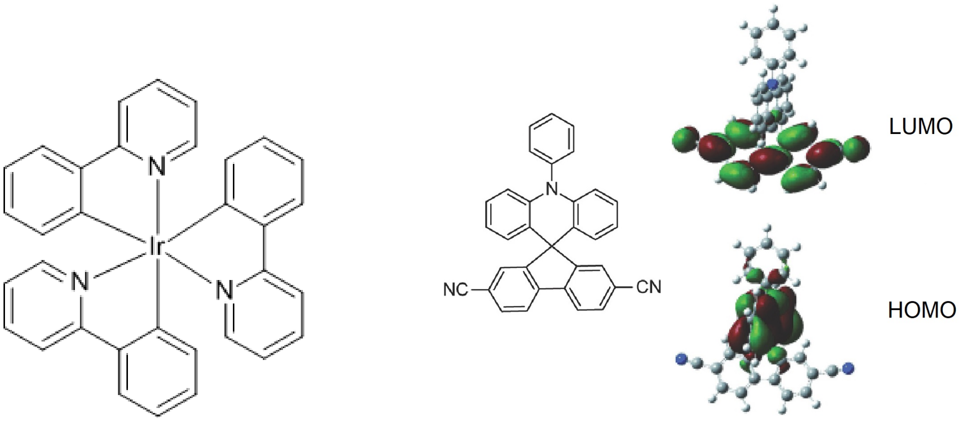

(a) $\mathrm{Ir(ppy)_3}$ used as phosphorescent emitter due to the spin-orbit coupling induced by the heavy Ir atom. Source: TCI Chemicals.

(b) ACRFLCN as TADF material with spatially separated HOMO and LUMO. Source: [64].

Figure 3.7: Example materials used for increased OLED efficiency using phosphorescence and TADF.

3.3.2 Nonradiative decay

Nonradiative decay is often also called *internal conversion* and results in a relaxation of the excited molecule under an emission of phonons. This process basically results from an isoenergetic transition from an excited state (mostly in its lowest vibrational state) to a lower excited state at a higher vibrational energy (see fig. 3.8). This process is very fast for transitions from higher excited states to the first excited state, for a higher singlet state S_n undergoing internal conversion with subsequent vibrational relaxation to the lowest vibrational state of S_1 this happens at timescales of 10^{-13} - 10^{-11} s [58].

This process can also lead to complete deexcitation to the molecular ground state S_0 but is less efficient due to the smaller energetic overlap of the vibrational states of S_0 with higher excited states (the energetic difference between S_0 and S_1 is much larger than between S_1 and higher excited states).

3.3.3 Inter-system crossing

Inter-system crossing (ISC) is a process akin to internal conversion as it consists of an isoenergetic change of state with potential subsequent nonradiative relaxation. However, while during internal conversion there is no change in spin, ISC involves a change in total spin i.e. a change from singlet to triplet state or vice-versa. This “forbidden” change is again enabled by spin-orbit coupling such that total angular momentum is conserved (see

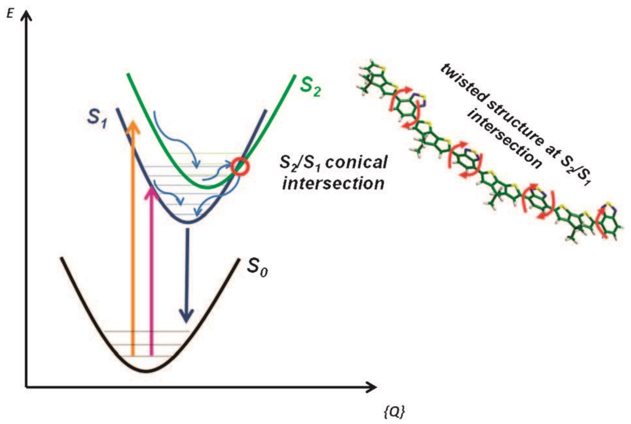

Figure 3.8: Internal conversion of a singlet exciton between absorption and emission of a photon. The isoenergetic transition from S_2 to S_1 is marked with a red circle, vibrational relaxation with light-blue curvy arrows. Source: [65].

discussion about phosphorescence in section 3.3.1), therefore again incorporation of heavy atoms renders this process quite efficient [15].

The transition from S_1 to T_n occurs readily into a vibrational higher triplet state with subsequent internal conversion and relaxation to the vibrational ground state of T_1. The opposite is not true, as T_1 always has lower energy than S_1 (Hund's rule [66]) and therefore there is an energy barrier to cross, i.e. this is a process requiring *thermal activation.* This is exactly where the second (after using phosphorescent materials) strategy to overcome the 25% limit of electroluminescence takes up by decreasing the energy difference between S_1 and T_1 states to promote ISC from triplets to singlets leading to *thermally activated delayed fluorescence* (TADF). This can be achieved by engineering molecules where HOMO and LUMO are spatially separated on the molecule [64], see for an example fig. 3.7b.

3.3.4 Polaron quenching

Exciton-polaron quenching is a process where the excitation energy is quenched (lost) through interaction with a polaron formed by a mobile charge carrier. This is an important *efficiency roll-off* effect in OLEDs at high current densities (increased luminance) [67]. Even though the exact mechanisms are not exactly understood [68] there are mainly two types of exciton-polaron quenching considered, namely Förster- and Dexter-type interactions. In case of the Förster-type polaron quenching, the exciton energy is first transferred to the polaron which creates an excited polaron state followed by fast relaxation and therefore loss of the exciton [67] (as the processes are the same as in section 3.2.1, this could be reduced by minimizing the spectral overlap [17]).

The second mechanism involves an electron transfer through tunneling (Dexter transport) when a free charge carrier charges a molecule in direct vicinity of the exciton and is therefore only of very short range [67]. Again, in a first step an excited charged molecule results followed by relaxation under emission of phonons leaving just a charged molecule behind, see fig. 3.9.

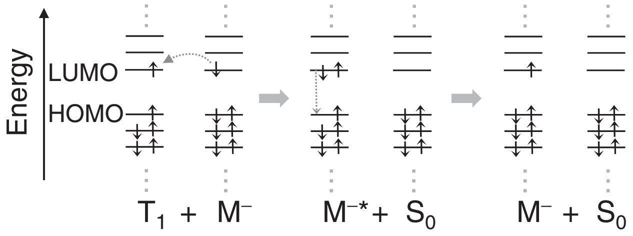

Figure 3.9: Dexter-type triplet-polaron quenching. M^- denotes the negatively charged molecule and M^{-*} the charged molecule in an excited state. Source: [28].

3.3.5 Exciton-exciton annihilation

Excitons can interact with one another upon collision leading to a non-radiative decay of at least one [21]. There are different combinations possible, e.g. singlet-singlet, singlet-triplet and triplet-triplet annihilation (SSA, STA, TTA) [28]. However, due to the longer triplet lifetimes and high triplet concentrations (especially in phosphorescent emitters) TTA constitutes the main factor contributing to efficiency loss [17]. TTA can result in two sets of products depending on their spin [49]:

$$T_1 + T_1 \longrightarrow S_0 + T_n \overset{\text{relax.}}{\longrightarrow} T_1$$
$$T_1 + T_1 \longrightarrow S_0 + S_n \overset{\text{relax.}}{\longrightarrow} S_1$$

The second reaction actually also contributes to TADF (as it's a conversion of triplets to a singlet state), so called *P-type fluorescence* [58].

3.3.6 Dissociation

As already mentioned earlier, in organic semiconductors the exciton binding energy is very high due to the low permittivity of the medium. This is a challenge in OPV where the final goal is to have free charge carriers contributing to the cell current, in contrast to the inorganic PV materials where this step can be omitted as absorption basically creates directly free carriers in the conduction and valence band [28]. In order to split the exciton an interface between the host and a donor-/acceptor-material is needed (see fig. 2.13a), as in such a transition the energy needed to overcome the Coulomb attraction of the e^-- h^+pair is compensated by placing the electron or hole in an energetically more favorable LUMO or HOMO level (see fig. 3.10).

As this separation involves a transition of an electron or hole to a neighboring molecule it can be modeled using again the Miller-Abrahams hopping approach (2.8) from section 2.2.3 considering the difference in energy of exciton binding energy and final LUMO/HOMO energies of the free carriers (Zhou et al. 2019, unpublished).

3.4 Experimental techniques

Some further experiments related to the investigation of excitonic properties are discussed here. Of course, this is by far not a complete list as there are a large number of experimental

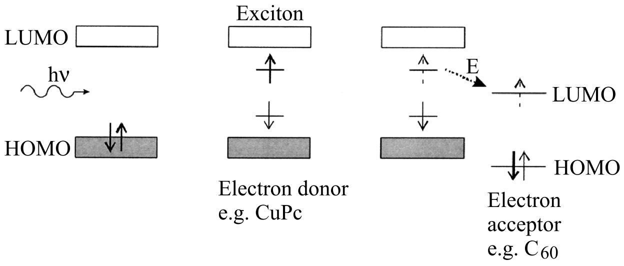

Figure 3.10: Exciton dissociation in a donor-acceptor system using an electron acceptor material providing a beneficial energy transition for the electron but not for the hole. Adapted from [49].

techniques available for investigating these properties and only a few popular examples are shown.

3.4.1 Ultraviolet photoelectric spectroscopy and cyclic voltammetry

Measurement of the emission and absorption spectrum of a material is a simple way to get an idea of the optical gap (i.e. exciton energies), however, if one seeks the energy levels of LUMO and HOMO levels relative to the vacuum level, different techniques are needed. Two such techniques are UV photoelectric spectroscopy (UPS) and cyclic voltammetry (CV).

In UPS, the electrons in the HOMO are ejected into the vacuum upon collision with the high energy photons. Their resulting kinetic energy is the photon energy minus the ionization energy

$$E = h\nu - I$$

Therefore, by measuring the spectrum of the electrons' kinetic energy, one can deduce the different ionization potentials for the different states in the material and therefore their energy levels relative to the vacuum level. It should be noted that these energies are the real energies taking electron-electron interactions into account in contrast to the often theoretically considered single-electron orbitals and energies [28].

CV works electrically instead of optically, by applying a linearly increasing voltage to the material in question in a solvent. At first, there is no current flow as the Fermi-level of the electrode lies in between the HOMO-LUMO gap, however, as soon as a certain potential is reached (Fermi-level and LUMO line up) a current starts to flow. This reduces the species close to the electrode and the current keeps flowing as long as there are reducible species in the electrode's vicinity. Therefore, with time the current decreases again as all molecules in the vicinity are reduced, and the potential is swept in the other direction, i.e. decreased, which leads to oxidation of the previously reduced species and therefore a negative current flow (see fig. 3.11a). The shifts in potential and current are caused by diffusion properties of the solvent, and by taking the average potential of the two current peaks, one can derive the LUMO (or HOMO if potential is reversed) energies relative to the electrode's Fermi-level [69].

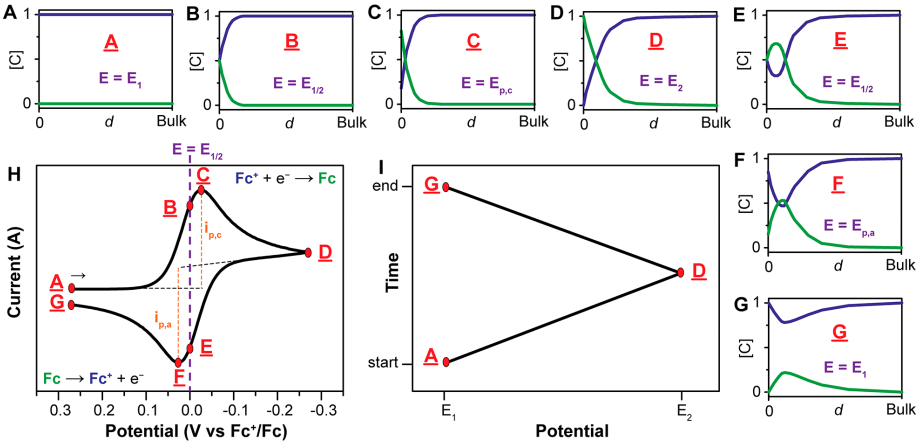

(a) A CV measurement showing the reaction $Fc^+ + e^- \leftrightarrow Fc$. Panels A-G show the concentrations (Fc^+ blue, Fc green) close to the electrode over time, panel H the current response and panel I the applied potential. Source: [69].

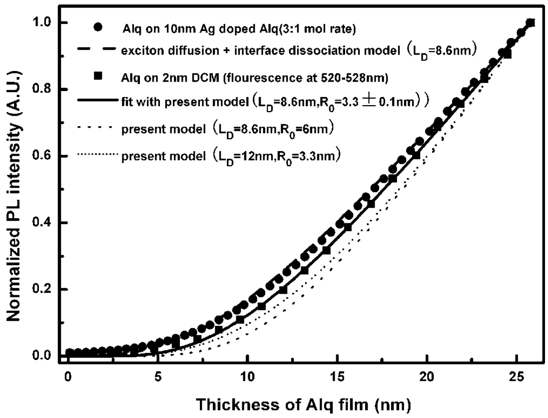

(b) Film-thickness dependent luminescence. Source: [70].

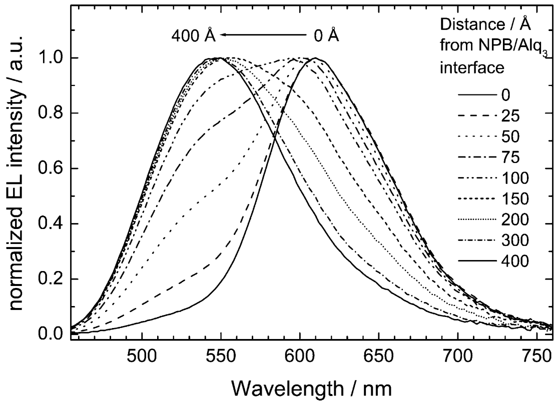

(c) Emission spectrum for different positions of the sensing layer. The left peak corresponds to the host, the right peak to the dopant spectrum. Source: [71].

Figure 3.11: Experiments investigating excitonic parameters such as energy levels, Förster radii and generation zones.

3.4.2 Förster radius probing

The strength of exciton transport is an important parameter for OPV and OLED devices. One way to investigate this parameter is by examining quenching by using *in-situ* PL measurements [70]. A film of the material under investigation is deposited onto a strongly quenching material (i.e. excitation energy is lost to the quenching material) while measuring the PL response of the deposited material. This results in a luminescence intensity measurement for varying film thickness as depicted in fig. 3.11b.

As excitons are generated optically in the film, these may be transported into the quenching material where they are lost if they get too close to the interface before radiatively decaying. By increasing the film thickness, a larger and larger share of the generated excitons will be too far away from the interface leading to increased luminescence emitted by the film. Below a certain thickness, luminescence of the film is almost zero as all the excitons are quenched from which a Förster radius may be derived.

3.4.3 Recombination zones

The recombination zones in an OLED are of interest to optimize performance by avoiding exciton quenching close to interfaces. To investigate the spatial distribution of electric exciton generation in an OLED emitter layer one can introduce thin *sensing layers* [71]. These layers are doped with a material having a very distinct emission spectrum such that by measuring the emission spectrum of the whole OLED as a function of sensing layer position the exciton generation at these positions can be deduced. At positions with high exciton generation (recombination), the excitons will be transferred onto the dopant resulting in a emission spectrum close to the one characteristic for the dopant, otherwise close to the one characteristic for the host material, see fig. 3.11c.

Chapter 4

Mathematical Model

After understanding the basic physical processes occurring in organic semiconductors regarding charge carriers and excitons, the next step is to form a mathematical model. This will be the main purpose of this chapter. First, a short description of the general concept of a "Master equation" is given in section 4.2. This will then be used in section 4.2 to form the mathematical model which governs the exciton dynamics and whose solution is the main result of the computations. Some more detail will be given in this section about the various aspects of the model as it comprises the core centerpiece of the later analysis. Finally, a short introduction into the model used for the charge carrier dynamics will be given.

4.1 The Master equation concept

A Master equation can be commonly defined in the following way [72]:

> "They [Master equations] are differential equations that describe the evolution of the probabilities for Markov processes for systems that jump from one to another state in continuous time."

A Markov process can be described as a stochastic process where the probabilities for the entire future of the system depend only on the last (current) state, i.e. [73]

$$p(\boldsymbol{x}_1, t_1; \boldsymbol{x}_2, t_2; \dots | \boldsymbol{y}_1, \tau_1; \boldsymbol{y}_2, \tau_2; \dots) = p(\boldsymbol{x}_1, t_1; \boldsymbol{x}_2, t_2; \dots | \boldsymbol{y}_1, \tau_1) \tag{4.1}$$

where $(\boldsymbol{x}_i, t_i)$ are the future states of the system and $(\boldsymbol{y}_i, \tau_i)$ the past states. From (4.1) by using some basic rules of probability theory one arrives at the *Chapman-Kolmogorov equation*

$$p(\boldsymbol{x}_1, t_1 | \boldsymbol{x}_3, t_3) = \int p(\boldsymbol{x}_1, t_1 | \boldsymbol{x}_2, t_2) p(\boldsymbol{x}_2, t_2 | \boldsymbol{x}_3, t_3) \mathrm{d}\boldsymbol{x}_2 \tag{4.2}$$

i.e. "the probability for the system to be in state $\boldsymbol{x}_1$ at time t_1 – given it was in state $\boldsymbol{x}_3$ at time t_3 – is equal to the probability of it being in state $\boldsymbol{x}_1$ at time t_1 – given it was in (some intermediate) state $\boldsymbol{x}_2$ at (some intermediate) time t_2 – times the probability it was in state $\boldsymbol{x}_2$ at time t_2 – given it was in state $\boldsymbol{x}_3$ at time t_3 – *integrated over all possible intermediate states* $\boldsymbol{x}_2$".

This can also be written in discrete state space (as will be necessary in the present case)

$$P(\boldsymbol{n}_1, t_1|\boldsymbol{n}_3, t_3) = \sum_{\boldsymbol{n}_2} P(\boldsymbol{n}_1, t_1|\boldsymbol{n}_2, t_2)P(\boldsymbol{n}_2, t_2|\boldsymbol{n}_3, t_3) \tag{4.3}$$

These conditional probabilities are not known in general and are in most cases difficult to derive from the rules of the process [72]. However, as mentioned above, even though the sample paths are discontinuous (jumps), time is treated continuously in the Master equation approach. Because of this, instead of using a time increment $t_3 \to t_1$ we can consider a small increment in the limit $t_1 - t_3 = \mathrm{d}t$ which allows for using rates, i.e.

$$P(\boldsymbol{n}_i, t + \mathrm{d}t|\boldsymbol{n}_j, t) = \omega(\boldsymbol{n}_j \to \boldsymbol{n}_i)\mathrm{d}t + \mathcal{O}\left(\mathrm{d}t^2\right) \tag{4.4}$$

By using (4.4) we can write (4.3) in the form

$$\begin{aligned} P(\boldsymbol{n}_i, t + \mathrm{d}t) = {} & P(\boldsymbol{n}_i, t)\left(1 - \sum_{\boldsymbol{n}_j \neq \boldsymbol{n}_i} \omega(\boldsymbol{n}_i \to \boldsymbol{n}_j)\mathrm{d}t\right) \\ & + \sum_{\boldsymbol{n}_j \neq \boldsymbol{n}_i} P(\boldsymbol{n}_j, t)\omega(\boldsymbol{n}_j \to \boldsymbol{n}_i)\mathrm{d}t + \mathcal{O}\left(\mathrm{d}t^2\right) \end{aligned} \tag{4.5}$$

which yields after rearranging [72]

$$\frac{\mathrm{d}P(\boldsymbol{n}_i, t)}{\mathrm{d}t} = \sum_{\boldsymbol{n}_j \neq \boldsymbol{n}_i} \left(P(\boldsymbol{n}_j, t)\omega(\boldsymbol{n}_j \to \boldsymbol{n}_i) - P(\boldsymbol{n}_i, t)\omega(\boldsymbol{n}_i \to \boldsymbol{n}_j)\right) \tag{4.6}$$

which is the general form of the *Master equation.* It is therefore a *differential Chapman-Kolmogorov equation.* In the way it is described here probability is conserved in the whole system as probability is only *exchanged* between states, however, it is also possible to include so-called *birth* and *death* which results in injected or removed probability. Furthermore, in this form the Master equation exhibits *detailed balance* (time reversibility in physical interpretation), i.e. at equilibrium

$$P_{\mathrm{eq}}(\boldsymbol{n}_j, t)\omega(\boldsymbol{n}_j \to \boldsymbol{n}_i) = P_{\mathrm{eq}}(\boldsymbol{n}_i, t)\omega(\boldsymbol{n}_i \to \boldsymbol{n}_j)$$

4.2 Master equation model for excitons

Now that additionally to the physical basis also the mathematical framework of the Master equation has been introduced, these concepts can be combined and the Master equation model for exciton dynamics can be set up. The different aspects of this will be the main focus of this section where first the model with its underlying assumptions is introduced in section 4.2.1. In the following, the modeling of the transport terms (section 4.2.2) and auxiliary models and boundary conditions (section 4.2.3) are discussed and finally a short introduction and comparison of the model used for the charge carrier dynamics is given.

4.2.1 Governing equations for excitons

Before introducing the equations, a small disclaimer is needed. Even though a Master equation model is used which is a probabilistic model acting on *probabilities*, the quantities used in this work do not fulfill the mathematical definition of a probability, most notably it is possible to get $p > 1$. Instead, it can be thought of as a probability density per elementary volume a_0^3. Therefore, the term *occupation number* or *exciton density* (dropping the *probability*) will be used throughout this work and it can be interpreted as the expectation value of number of excitons present on a specific molecule (compare e.g. Bose-Einstein statistics).

Much of the basic model was adapted from [74]. As we're dealing with organic semiconductors it is assumed that strongly localized Frenkel excitons (see section 3.1.1) need to be considered only, such that for each molecule one can define the occupation numbers p^{s} and p^{t} denoting singlets and triplets, respectively. Furthermore, due to the comparatively fast relaxation from higher to the lowest excited states S_1 and T_1, only these states are considered. The dependency on time will not be shown generally but it should be kept in mind that the exciton densities are certainly a function of time. Additionally, the carrier densities p^{e} and p^{h} vary with time as well. From this one can write down the rate equation in ME form as

$$\begin{aligned}\frac{\mathrm{d}p_i^{\mathrm{s}}}{\mathrm{d}t} =&\sum_{f\neq i}\left[p_f^{\mathrm{s}}\omega_{fi}^{\mathrm{F,s}} - p_i^{\mathrm{s}}\omega_{if}^{\mathrm{F,s}}\right] + \sum_{d\neq i}\left[p_d^{\mathrm{s}}\omega_{di}^{\mathrm{D,s}} - p_i^{\mathrm{s}}\omega_{id}^{\mathrm{D,s}}\right]\\ &+\left(\frac{1}{\tau_{\mathrm{r},i}^{\mathrm{s}}} + \frac{1}{\tau_{\mathrm{nr},i}^{\mathrm{s}}}\right)\left(\exp\left(\frac{E_{\mathrm{b},i}^{\mathrm{s}} - E_{\mathrm{g},i}}{k_BT}\right) - p_i^{\mathrm{s}}\right)\\ &+\frac{p_i^{\mathrm{t}}}{\tau_{\mathrm{ISC},i}}\cdot\exp\left(\frac{E_{\mathrm{b},i}^{\mathrm{s}} - E_{\mathrm{b},i}^{\mathrm{t}}}{k_BT}\right) - \frac{p_i^{\mathrm{s}}}{\tau_{\mathrm{ISC},i}}\\ &-\frac{p_i^{\mathrm{s}}\left(p_i^{\mathrm{e}} + p_i^{\mathrm{h}}\right)}{\tau_{\mathrm{SPQ},i}} + \frac{\left(p_i^{\mathrm{t}}\right)^2}{2\tau_{\mathrm{TTA},i}}\\ &+g_{\mathrm{Rec},i}\left(\frac{p_i^{\mathrm{e}}p_i^{\mathrm{h}}}{\tau_i} - \frac{p_i^{\mathrm{s}}}{\tau_i}\exp\left(-\frac{E_{\mathrm{b},i}^{\mathrm{s}}}{k_BT}\right)\right) + g_{\mathrm{Opt},i}G_i\end{aligned} \tag{4.7}$$

$$\begin{aligned}\frac{\mathrm{d}p_i^{\mathrm{t}}}{\mathrm{d}t} =&\sum_{f\neq i}\left[p_f^{\mathrm{t}}\omega_{fi}^{\mathrm{F,t}} - p_i^{\mathrm{t}}\omega_{if}^{\mathrm{F,t}}\right] + \sum_{d\neq i}\left[p_d^{\mathrm{t}}\omega_{di}^{\mathrm{D,t}} - p_i^{\mathrm{t}}\omega_{id}^{\mathrm{D,t}}\right]\\ &+\left(\frac{1}{\tau_{\mathrm{r},i}^{\mathrm{t}}} + \frac{1}{\tau_{\mathrm{nr},i}^{\mathrm{t}}}\right)\left(\exp\left(\frac{E_{\mathrm{b},i}^{\mathrm{t}} - E_{\mathrm{g},i}}{k_BT}\right) - p_i^{\mathrm{t}}\right)\\ &+\frac{p_i^{\mathrm{s}}}{\tau_{\mathrm{ISC},i}} - \frac{p_i^{\mathrm{t}}}{\tau_{\mathrm{ISC},i}}\cdot\exp\left(\frac{E_{\mathrm{b},i}^{\mathrm{s}} - E_{\mathrm{b},i}^{\mathrm{t}}}{k_BT}\right)\\ &-\frac{p_i^{\mathrm{t}}\left(p_i^{\mathrm{e}} + p_i^{\mathrm{h}}\right)}{\tau_{\mathrm{TPQ},i}} - \frac{\left(p_i^{\mathrm{t}}\right)^2}{\tau_{\mathrm{TTA},i}}\\ &+(1-g_{\mathrm{Rec},i})\left(\frac{p_i^{\mathrm{e}}p_i^{\mathrm{h}}}{\tau_i} - \frac{p_i^{\mathrm{t}}}{\tau_i}\exp\left(-\frac{E_{\mathrm{b},i}^{\mathrm{t}}}{k_BT}\right)\right) + (1-g_{\mathrm{Opt},i})G_i\end{aligned} \tag{4.8}$$

where (4.7) is the rate equation for the singlets and (4.8) the one for the triplets. The first row represents exciton transport with ω_{ij}^{F} the Förster rate $i \to j$ and ω_{ij}^{D} the corresponding Dexter rate, the second row represents radiative τ_{r} and nonradiative τ_{nr} decay (with the exponential for detailed balance), in the third row are the inter-system crossing terms in both directions, in the fourth row we have polaron quenching and triplet-triplet annihilation and finally in the last row the main source terms, namely charge carrier recombination (with detailed balance) and optical generation.

The coefficients $g_{\mathrm{Rec},i}$ and $g_{\mathrm{Opt},i}$ represent the relative share of generation which results in singlets. From section 3.1.2 these are mostly equal to 0.25 and 1, respectively. Even though in section 3.2.1 it was shown that Förster transport conserves spin and as only the lowest excited states S_1 and T_1 are considered in the model, Förster transport is still included in (4.8). This is due to the fact that in phosphorescent materials this spin selection rule is weakened and Förster transport is possible to some degree. Another assumption is that quenching rates are much larger than hopping, such that polaron quenching and triplet-triplet annihilation occur locally instead of Förster-/Dexter-mediated [68]. Furthermore, it is assumed that triplet-triplet annihilation is much stronger than other exciton-exciton annihilation paths and therefore only TTA is taken into account with the result of losing two triplets and gaining one singlet in return. All τ's are material parameters and E_{b}, E_{g} are exciton binding and HOMO-LUMO gap energies, respectively. The coupling to the charge carrier simulation comes from the recombination and polaron quenching terms by including p^e and p^h, the electron and hole densities, respectively.

Some further aspects should be noted. First, due to the fact that the Master equation was formulated for molecular occupation numbers, the final grid used for solving the equations is not a discretization of some underlying physical continuum equation, instead, it is given directly by the distribution of single molecules in the material matrix itself, which may be described as *molecular discretization*. Let's also analyze these equations a bit further. They represent a large system of coupled *nonlinear and inhomogeneous ordinary differential equations of first order with non-constant coefficients*. The nonlinearity is introduced by the triplet-triplet annihilation terms and the coefficients are non-constant due to the time-dependency of the charge carrier densities and energy levels. Furthermore, as exciton transport is governed by diffusion, these equations are most probably *stiff* which makes them difficult to integrate over time.

4.2.2 Exciton transport models

As mentioned above, exciton diffusion is modeled as hopping transport by Förster and Dexter transport mechanisms which describe the hopping rates ω_{ij}. For Förster transport equation (3.10) can be used giving

$$\omega_{ij}^{\mathrm{F}} = \left(\frac{1}{\tau_{\mathrm{r},i}} + \frac{1}{\tau_{\mathrm{nr},i}}\right) \left(\frac{R_0^{\mathrm{F}}}{R_{ij}}\right)^6 \exp\left(-\frac{|\Delta E_{ij}^{\mathrm{et}}| + \Delta E_{ij}^{\mathrm{et}}}{2k_B T}\right) \tag{4.9}$$

where $R_{ij} = ||\boldsymbol{r}_j - \boldsymbol{r}_i||_2$ and $\Delta E_{ij}^{\mathrm{et}} = E_j^{\mathrm{et}} - E_i^{\mathrm{et}} = (E_{\mathrm{g},j} - E_{\mathrm{b},j}) - (E_{\mathrm{g},i} - E_{\mathrm{b},i})$ the difference in exciton energy at site j and i. If this energy difference is positive the Boltzmann factor induces an energy penalty for such a jump. As this rate is dependent on material parameters the question arises which parameter set to choose in case different materials are involved. In this case the geometric mean

$$\sqrt{\omega^{\mathrm{F}}_{A}\omega^{\mathrm{F}}_{B}}$$

is taken where the subscript denotes the material parameter set used to calculate the rate.

Similarly, we can use equation (3.11) to model the Dexter transport rates

$$\omega^{\mathrm{D}}_{ij} = k^{\mathrm{D}}_{0} \exp\left(-\frac{2R_{ij}}{L^{\mathrm{D}}}\right) \exp\left(-\frac{|\Delta E^{\mathrm{et,e}}_{ij}| + \Delta E^{\mathrm{et,e}}_{ij}}{2k_B T}\right) \exp\left(-\frac{|\Delta E^{\mathrm{et,h}}_{ij}| + \Delta E^{\mathrm{et,h}}_{ij}}{2k_B T}\right) \tag{4.10}$$

where $E^{\mathrm{et,e}}_{i}$ and $E^{\mathrm{et,h}}_{i}$ are the bound electron and bound hole energies with

$$E^{\mathrm{et,e}}_{i} = E_{\mathrm{LUMO},i} - \frac{E_{\mathrm{b},i}}{2}$$
$$E^{\mathrm{et,h}}_{i} = E_{\mathrm{HOMO},i} + \frac{E_{\mathrm{b},i}}{2}$$

Note that in the current form these Dexter rates would depend on the absolute energy levels of the donor and acceptor sites and therefore would depend on time. However, in the current work this time-dependency was neglected as this would lead to a difficult situation in transient simulations, as basically the complete Jacobian would then need to be updated at every timestep. The formulation is kept in this way though, as for steady-state simulations it is preferred. Here some further simplifications were made in the model. Even though the physical variables R^{F}_{0} and L^{D} are in reality quantities depending on many factors such as spectral overlap, orientation and quantum-physical properties of the molecules, they are assumed constants in the present model simply representing the different strengths of the mechanisms. This is especially for Förster transport quite a strong simplification as this neglects the superiority of host-to-guest transport over the other transport paths (e.g. host-to-host or guest-to-host) and should be changed in a future work.

The summation terms in (4.7) and (4.8) are over *all sites* (molecules) in the material except the local one. Therefore, theoretically, every site is coupled to all other sites leading to full submatrices which would make the solution of a bigger system unfeasible. From the physical model we see however that the strength of these interactions decays quickly, see fig. 4.1, and a *cutoff distance* R_c can be introduced from where on the couplings are neglected, i.e. $\omega^{\mathrm{F}}(R > R_c) = \omega^{\mathrm{D}}(R > R_c) = 0$ which results in a very sparse banded matrix structure. Note however that in 3D this number scales as $\mathcal{O}\left(R_c^3\right)$ so even for (relatively) small R_c the number of coupled equations (sites) is still large. Often a cutoff distance of $R_c \approx 4a_0$ is chosen [74] where a_0 is the intermolecular or grid spacing.

The equations considered up to now will work fine if one is interested in simulating exciton dynamics in OLED devices where there are no dissociation interfaces present in the stack and dissociation can be neglected. However, in the case of e.g. OPV applications where the splitting of excitons into free e^-- h^+pairs is desired and such interfaces are used, one needs to take this process into account. As mentioned in section 3.3.6 this transfer can be modeled

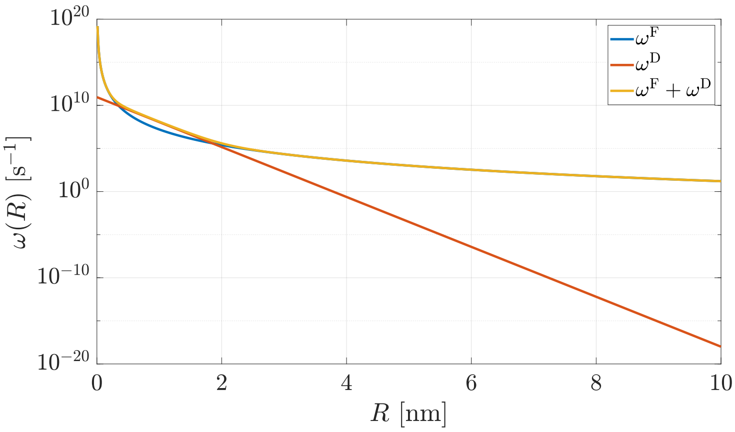

Figure 4.1: Decay of the singlet hopping rates over R for ω^{F}, ω^{D} and $\omega^{\mathrm{F}}+\omega^{\mathrm{D}}$ in Ir(ppy)$_3$ (see [74]).

as an exchange mechanism mediated with an Abrahams-Miller hopping rate (Zhou et al. 2019, unpublished)

$$\omega_{DA}^{\mathrm{et,e}} = \nu_0^{\mathrm{e}} \exp\left(-2\alpha R_{DA} - \frac{\left|E_D^{\mathrm{e}} - E_A^{\mathrm{e}} - E_{\mathrm{b},D}^{\mathrm{et}}\right| - \left(E_D^{\mathrm{e}} - E_A^{\mathrm{e}} - E_{\mathrm{b},D}^{\mathrm{et}}\right)}{2k_BT}\right) \tag{4.11}$$

for electrons and similarly for holes, where E_D^{e}, E_A^{e} are the LUMO energies at the donor and acceptor, respectively (see fig. 4.2). The second term in the exponential introduces an energy barrier if the difference of LUMO at the donor to the acceptor is smaller than the binding energy of the exciton at the donor.

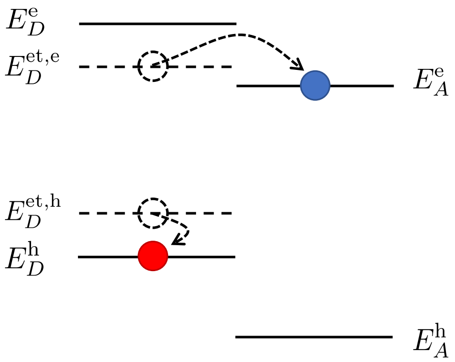

Figure 4.2: Interface dissociation of an exciton by Abrahams-Miller hopping where the electron (blue) hops to a neighboring site with lower LUMO, splitting the exciton. After (Zhou et al. 2019, unpublished).

4.2.3 Auxiliary modeling

Disorder models

Now that the equations are set-up, the transport rates are modeled and most of the parameters are defined by the material there is still one part which needs additional modeling, the different energy levels. For solving the Master equations we need the singlet and triplet binding energies $E^{\mathrm{s}}_{\mathrm{b},i}$ and $E^{\mathrm{t}}_{\mathrm{b},i}$, respectively, as well as the LUMO and HOMO levels E^e_i and E^h_i from which we can calculate the gap energy $E_{\mathrm{g},i}$. These energies for the different sites are defined by the DOS of the material and as discussed in section 2.1.4 we can use a Gaussian distribution. In total E^e_i and E^h_i consist of four, the exciton binding energies of two contributions, i.e.

$$E^{\mathrm{e,h}}_i = E^{\mathrm{e,h}}_{\mathrm{mean}} + q\Phi_i + q\Phi_{\mathrm{im},i} + \xi^{\mathrm{e,h}}_i \tag{4.12}$$

$$E^{\mathrm{s,t}}_{\mathrm{b},i} = E^{\mathrm{s,t}}_{\mathrm{b,mean}} + \xi^{\mathrm{et}}_i \tag{4.13}$$

where in equation (4.12) $E^{\mathrm{e,h}}_{\mathrm{mean}}$ is a mean LUMO/HOMO energy specific for the material, Φ_i is the potential obtained from a 1D Poisson-equation (see section 4.3), $\Phi_{\mathrm{im},i}$ is the contribution from the image potential near the electrodes [7]

$$q\Phi_{\mathrm{im},i} = -\frac{q^2}{16\pi\varepsilon_0\varepsilon_r a_0}\left(\frac{1}{m_x - i_x} + \frac{1}{i_x + 1}\right) \tag{4.14}$$

(m_x is the number of sites in x-direction along the stack) and finally the random contribution taken from the Gaussian DOS $\xi^{e,h}_i \sim \mathcal{N}(0, \sigma^2)$ with σ being a material parameter defining the magnitude of disorder. The Gaussian DOS can be uncorrelated (GDM), then equation (2.4) with $E_{\mathrm{mean}} = 0$ applies, but depending on the material also correlated disorder can be appropriate, e.g. due to stronger intermolecular dipole interactions, then one uses [23]

$$\xi^{\mathrm{e,h}}_i = \sum_{j\neq i} \frac{q\boldsymbol{d}_j \cdot (\boldsymbol{r}_j - \boldsymbol{r}_i)}{\varepsilon_0\varepsilon_r \left|\left|\boldsymbol{r}_j - \boldsymbol{r}_i\right|\right|_2^3} \tag{4.15}$$

which gives for random directions of $\boldsymbol{d}$ and $d = ||\boldsymbol{d}||_2$ a distribution approximately Gaussian with width $\sigma = 2.35\frac{qd}{\varepsilon_0\varepsilon_r a_0^2}$ yielding the *correlated disorder model* (CDM).

In equation (4.13) the exciton binding energy as well incorporates a mean singlet and triplet binding energy specific to the material, however, the random contribution ξ^{et}_i is the same for singlets as for triplets (in order to avoid the unphysical situation that $E^{\mathrm{s}}_{\mathrm{b}} > E^{\mathrm{t}}_{\mathrm{b}}$) and is always uncorrelated.

The disorder considered up to now is diagonal disorder, i.e. the disorder of the local state energies for each molecule. The second type, off-diagonal disorder, could also be considered by using a grid with random grid point positions and/or by letting R^{F}_0 vary randomly (due to the dependency on relative orientation) [75]. This type of disorder is not considered for the present work though.

Boundary conditions

As the Master equation approach models all layers in one grid, we always have six boundaries, namely at the x, y and z faces of the rectangular cuboid formed by the grid, where x is the direction along the stack, i.e. from one electrode to the other. As such devices are usually much wider than thick (i.e. $d_z, d_y \gg d_x$) the lateral dimensions cannot be modeled entirely, instead, only a certain lateral width is considered (e.g. $\Delta y = \Delta z = 30a_0$) and *periodic boundary conditions* are applied. For the Master equation approach this means that transport terms belonging to sites close to these y and z faces which would extend to the exterior of the grid are wrapped around and couple sites on opposite sides.

At the x faces it is assumed that either an electrode or a completely insulating medium exist such that no excitation energy transfer is possible, i.e. on these boundaries *no-flow* boundary conditions are applied.

4.2.4 Species decoupling

Instead of using the scalar representation of the exciton Master equation (4.7) and (4.8) one can also write two vector-valued equations representing the occupation numbers of all sites for singlets and triplets. See A.1 for the definition of the matrices and vectors used in expressions (4.16) and (4.17).

$$\begin{aligned}\frac{\mathrm{d}\boldsymbol{p}^{\mathrm{s}}}{\mathrm{d}t} =& \left(\boldsymbol{W}_{\mathrm{F}}^{\mathrm{s}} + \boldsymbol{W}_{\mathrm{D}}^{\mathrm{s}} - \boldsymbol{D}_{\mathrm{Dec}}^{\mathrm{s}} - \boldsymbol{D}_{\mathrm{ISC}}^{\mathrm{s}} - \boldsymbol{D}_{\mathrm{SPQ}} - \boldsymbol{D}_{\mathrm{RecB}}^{\mathrm{s}}\right) \boldsymbol{p}^{\mathrm{s}} \\ &+ \boldsymbol{D}_{\mathrm{ISC}}^{\mathrm{t}} \boldsymbol{p}^{\mathrm{t}} + \boldsymbol{D}_{\mathrm{Dec}}^{\mathrm{s}} \boldsymbol{b}^{\mathrm{s}} + \frac{1}{2} \boldsymbol{D}_{\mathrm{TTA}} \boldsymbol{d}^{2}(\boldsymbol{p}^{\mathrm{t}}) + \boldsymbol{b}_{\mathrm{Rec}}^{\mathrm{s}} + \boldsymbol{b}_{\mathrm{Opt}}^{\mathrm{s}}\end{aligned} \tag{4.16}$$

$$\begin{aligned}\frac{\mathrm{d}\boldsymbol{p}^{\mathrm{t}}}{\mathrm{d}t} =& \left(\boldsymbol{W}_{\mathrm{F}}^{\mathrm{t}} + \boldsymbol{W}_{\mathrm{D}}^{\mathrm{t}} - \boldsymbol{D}_{\mathrm{Dec}}^{\mathrm{t}} - \boldsymbol{D}_{\mathrm{ISC}}^{\mathrm{t}} - \boldsymbol{D}_{\mathrm{TPQ}} - \boldsymbol{D}_{\mathrm{RecB}}^{\mathrm{t}}\right) \boldsymbol{p}^{\mathrm{t}} \\ &+ \boldsymbol{D}_{\mathrm{ISC}}^{\mathrm{s}} \boldsymbol{p}^{\mathrm{s}} + \boldsymbol{D}_{\mathrm{Dec}}^{\mathrm{t}} \boldsymbol{b}^{\mathrm{t}} - \boldsymbol{D}_{\mathrm{TTA}} \boldsymbol{d}^{2}(\boldsymbol{p}^{\mathrm{t}}) + \boldsymbol{b}_{\mathrm{Rec}}^{\mathrm{t}} + \boldsymbol{b}_{\mathrm{Opt}}^{\mathrm{t}}\end{aligned} \tag{4.17}$$

From this representation it is clearly visible that the two species are only coupled by a diagonal matrix $\boldsymbol{D}_{\mathrm{ISC}}$ (as ISC only occurs locally on a site) which is easily invertible. In steady-state ($\frac{\mathrm{d}\boldsymbol{p}^{\mathrm{s}}}{\mathrm{d}t} = \frac{\mathrm{d}\boldsymbol{p}^{\mathrm{t}}}{\mathrm{d}t} = 0$) we can therefore solve (4.17) for $\boldsymbol{p}^{\mathrm{s}}$

$$\boldsymbol{p}^{\mathrm{s}} = \left(\boldsymbol{D}_{\mathrm{ISC}}^{\mathrm{s}}\right)^{-1} \left(\boldsymbol{D}_{\mathrm{TTA}} \boldsymbol{d}^{2}(\boldsymbol{p}^{\mathrm{t}}) - \boldsymbol{b}_{\mathrm{Rec}}^{\mathrm{t}} - \boldsymbol{b}_{\mathrm{Opt}}^{\mathrm{t}} - \boldsymbol{D}_{\mathrm{Dec}}^{\mathrm{t}} \boldsymbol{b}^{\mathrm{t}} - \boldsymbol{M}^{\mathrm{t}} \boldsymbol{p}^{\mathrm{t}}\right) \tag{4.18}$$

and insert the resulting expression into (4.16) yielding

$$\begin{aligned}0 =& \boldsymbol{M}^{\mathrm{s}} \left(\boldsymbol{D}_{\mathrm{ISC}}^{\mathrm{s}}\right)^{-1} \left(\boldsymbol{D}_{\mathrm{TTA}} \boldsymbol{d}^{2}(\boldsymbol{p}^{\mathrm{t}}) - \boldsymbol{b}_{\mathrm{Rec}}^{\mathrm{t}} - \boldsymbol{b}_{\mathrm{Opt}}^{\mathrm{t}} - \boldsymbol{D}_{\mathrm{Dec}}^{\mathrm{t}} \boldsymbol{b}^{\mathrm{t}} - \boldsymbol{M}^{\mathrm{t}} \boldsymbol{p}^{\mathrm{t}}\right) \\ &+ \boldsymbol{D}_{\mathrm{ISC}}^{\mathrm{t}} \boldsymbol{p}^{\mathrm{t}} + \boldsymbol{D}_{\mathrm{Dec}}^{\mathrm{s}} \boldsymbol{b}^{\mathrm{s}} + \frac{1}{2} \boldsymbol{D}_{\mathrm{TTA}} \boldsymbol{d}^{2}(\boldsymbol{p}^{\mathrm{t}}) + \boldsymbol{b}_{\mathrm{Rec}}^{\mathrm{s}} + \boldsymbol{b}_{\mathrm{Opt}}^{\mathrm{s}}\end{aligned} \tag{4.19}$$

which is only a function of $\boldsymbol{p}^{\mathrm{t}}$. To solve this nonlinear equation, we need the Jacobian ${}^{\mathrm{d}\boldsymbol{f}(\boldsymbol{p}^{\mathrm{t}})}/_{\mathrm{d}\boldsymbol{p}^{\mathrm{t}}}$ which is given by

$$\boldsymbol{J}_{\mathrm{decoup}}^{\mathrm{t}} = \boldsymbol{D}_{\mathrm{ISC}}^{\mathrm{t}} - \underbrace{\boldsymbol{M}^{\mathrm{s}} \left(\boldsymbol{D}_{\mathrm{ISC}}^{\mathrm{s}}\right)^{-1} \boldsymbol{M}^{\mathrm{t}}}_{1} + \underbrace{2 \left(\frac{1}{2} \boldsymbol{I} + \boldsymbol{M}^{\mathrm{s}} \left(\boldsymbol{D}_{\mathrm{ISC}}^{\mathrm{s}}\right)^{-1}\right) \boldsymbol{D}_{\mathrm{TTA}} \boldsymbol{D}_{\mathrm{p}}^{\mathrm{t}}}_{2} \tag{4.20}$$

where $\boldsymbol{I}$ is the unitary matrix. The benefit of this approach is the fact that the number of DOF is halved and two smaller systems can be solved sequentially instead of solving one big system once. However, this also introduces some heavy drawbacks which manifest in the terms 1 and 2 in (4.20). Let's have a look at term 1 first, the two matrices $\boldsymbol{M}^{\mathrm{s}}$ and $\boldsymbol{M}^{\mathrm{t}}$ are $(n \times n)$ matrices with n the number of sites, consisting of the sum of some diagonal matrices *and the banded transport matrices* $\boldsymbol{W}_{\mathrm{F}}$ and $\boldsymbol{W}_{\mathrm{D}}$ resulting in the same structure as the transport matrices. In term 1 a sparse matrix multiplication is needed, resulting in a banded matrix where the bandwidth is still bound to $\mathrm{bandw}(\boldsymbol{M}^{\mathrm{s}}\boldsymbol{M}^{\mathrm{t}}) = \mathrm{bandw}(\boldsymbol{M}^{\mathrm{s}}) + \mathrm{bandw}(\boldsymbol{M}^{\mathrm{t}})$ but with many more nonzero entries making the evaluation of it very expensive.

The second drawback in term 2 comes from the fact that the matrix $\boldsymbol{D}_{\mathrm{p}}^{\mathrm{t}}$ containing the unknowns is multiplied with the band matrix $\boldsymbol{M}^{\mathrm{s}}$. This results in a widely spread dependency of the Jacobian $\boldsymbol{J}_{\mathrm{decoup}}^{\mathrm{t}}$ on the unknowns which makes the update difficult. Note that techniques such as quasi-Newton algorithms will also not mitigate this issue as this multiplication also appears in (4.19), therefore the evaluation of $\boldsymbol{f}(\boldsymbol{p}^{\mathrm{t}})$ is as difficult as updating the Jacobian.

A similar derivation can be done if the transient case is considered which results in the equations (neglecting time dependency of Dexter rates)

$$\frac{\mathrm{d}\boldsymbol{p}^{\mathrm{t}}}{\mathrm{d}t} = \dot{\boldsymbol{p}}^{\mathrm{t}} \tag{4.21}$$

$$\begin{aligned}
\frac{\mathrm{d}\dot{\boldsymbol{p}}^{\mathrm{t}}}{\mathrm{d}t} =\ & \left[\boldsymbol{D}_{\mathrm{ISC}}^{\mathrm{s}}\boldsymbol{M}^{\mathrm{s}}(\boldsymbol{D}_{\mathrm{ISC}}^{\mathrm{s}})^{-1} + \boldsymbol{M}^{\mathrm{t}} - 2\boldsymbol{D}_{\mathrm{TTA}}\boldsymbol{D}_{\mathrm{p}}^{\mathrm{t}}\right]\dot{\boldsymbol{p}}^{\mathrm{t}} \\
& + \left[\boldsymbol{D}_{\mathrm{ISC}}^{\mathrm{s}}\left(\boldsymbol{M}^{\mathrm{s}}(\boldsymbol{D}_{\mathrm{ISC}}^{\mathrm{s}})^{-1}\left(\boldsymbol{D}_{\mathrm{TTA}}\boldsymbol{D}_{\mathrm{p}}^{\mathrm{t}} - \boldsymbol{M}^{\mathrm{t}}\right) + \boldsymbol{D}_{\mathrm{ISC}}^{\mathrm{t}} + \frac{1}{2}\boldsymbol{D}_{\mathrm{TTA}}\boldsymbol{D}_{\mathrm{p}}^{\mathrm{t}}\right) - \frac{\mathrm{d}}{\mathrm{d}t}\left(\boldsymbol{D}_{\mathrm{TPQ}}\right)\right]\boldsymbol{p}^{\mathrm{t}} \\
& + \boldsymbol{D}_{\mathrm{ISC}}^{\mathrm{s}}\left(\boldsymbol{D}_{\mathrm{Dec}}^{\mathrm{s}}\boldsymbol{b}^{\mathrm{s}} + \boldsymbol{b}_{\mathrm{Rec}}^{\mathrm{s}} + \boldsymbol{b}_{\mathrm{Opt}}^{\mathrm{s}} - \boldsymbol{M}^{\mathrm{s}}(\boldsymbol{D}_{\mathrm{ISC}}^{\mathrm{s}})^{-1}\left(\boldsymbol{D}_{\mathrm{Dec}}^{\mathrm{t}}\boldsymbol{b}^{\mathrm{t}} + \boldsymbol{b}_{\mathrm{Rec}}^{\mathrm{t}} + \boldsymbol{b}_{\mathrm{Opt}}^{\mathrm{t}}\right)\right) + \frac{\mathrm{d}}{\mathrm{d}t}\left(\boldsymbol{b}_{\mathrm{Rec}}^{\mathrm{t}} + \boldsymbol{b}_{\mathrm{Opt}}^{\mathrm{t}}\right)
\end{aligned} \tag{4.22}$$

Apart from introducing a very complicated expression including time-derivatives of input parameters (carrier densities) in (4.22) this approach leads to differential equations of second order and therefore no reduction in DOF is achieved. For these reasons, this approach will not be further considered.

4.2.5 Comparison to the continuum model

In the commercial simulation software *setfos*, excitons can also be simulated using a 1D continuum model approach. The equation which is solved for each species is given as

$$\begin{aligned}
\frac{\mathrm{d}S_i(x)}{\mathrm{d}t} =\ & g_i R(x) + \nabla(D_s \nabla S_i) - (k_{\mathrm{rad},i}(z) + k_{\mathrm{nonrad},i})S_i(z) - k_{\mathrm{annihilation},i}S_i(z)^2 \\
& + \sum_{j=1}^{n_{\mathrm{exc}}}\left(k_{ji}\left(1 - \frac{S_i}{S_{\mathrm{max},i}}\right)S_j(z) - k_{ij}\left(1 - \frac{S_j}{S_{\mathrm{max},j}}\right)S_i(z)\right) \\
& + \sum_{j=1}^{n_{\mathrm{exc}}}\left(k_{ij}\exp\left(\frac{-\Delta E_{ji}}{k_B T}\right)S_j(z) - k_{ji}\exp\left(\frac{-\Delta E_{ji}}{k_B T}\right)S_i(z)\right) \\
& + \sum_{j=1}^{n_{\mathrm{exc}}}\left(tts_{ji} \cdot k_{\mathrm{annihilation},j}S_j(z)^2\right) \\
& - k_{\mathrm{tp},i}S_i(z)p(z) - k_{\mathrm{tn},i}S_i(z)n(z) - k_{\mathrm{tn},ti}S_i(z)n_t(z) - k_{\mathrm{tp},ti}S_i(z)p_t(z) \\
& + g_{\mathrm{opt}_{\mathrm{exc}},i}G(z) - k_{\mathrm{d},i}S_i(z)
\end{aligned} \tag{4.23}$$

where the first line describes generation by recombination, exciton diffusion, (non-)radiative decay and exciton-exciton annihilation. The second and third line describe inter-system crossing either thermally activated or not, the fourth represents the gain through exciton-

exciton annihilation of other species, the fifth stands for polaron quenching and the final line for optical generation and exciton dissociation.

The most important difference is the term describing exciton transport. In the continuum model transport is simply governed by the diffusion term $\nabla(D_s \nabla S_i)$ where only nearest neighbor interactions are considered and the spatial variation of material type cannot be resolved (e.g. quenching at a specific location of a dopant molecule). Furthermore, in the current state of the model, any material interface results in a no-flow boundary condition, therefore excitons cannot be exchanged through the layer interfaces. Due to the low dimensionality of the model also no material variation per layer can be well resolved. On the other hand, of course, the solution of such a model is much less expensive than a full 3D model.

A connection between the two models can be established by applying the *Kramers-Moyal* expansion to the probabilistic Master equations (4.7) and (4.8) (after [76]). To show this the expansion is applied to the triplet equations but the procedure is valid for both species and the identifier will be dropped later. The given equation can be reformulated to describe a continuous state space instead of a discrete one such that the state transition rates need to be redefined as

$$\omega_{ij} \longrightarrow \tilde{\omega}(r' \to r)\mathrm{d}r = \tilde{\omega}(r', \delta r)\mathrm{d}r, \quad \delta r = r - r' \tag{4.24}$$

with r', r and δr the initial and final state and the “distance” in state space between the two states. The quantity $\tilde{\omega}$ is now in the continuous space a *state transition density* such that $\tilde{\omega}(r' \to r)\mathrm{d}r$ is the transition probability from state r' to the interval $(r, r + \mathrm{d}r)$ per unit time. Therefore, the triplet Master equation from (4.8) becomes

$$\begin{aligned}
\frac{\partial p^{\mathrm{t}}(r)}{\partial t} &= \int \left[\tilde{\omega}^{\mathrm{F}}(r - \delta r, \delta r) p^{\mathrm{t}}(r - \delta r) - \tilde{\omega}^{\mathrm{F}}(r, -\delta r) p^{\mathrm{t}}(r)\right] \mathrm{d}(\delta r) \\
&+ \int \left[\tilde{\omega}^{\mathrm{D}}(r - \delta r, \delta r) p^{\mathrm{t}}(r - \delta r) - \tilde{\omega}^{\mathrm{D}}(r, -\delta r) p^{\mathrm{t}}(r)\right] \mathrm{d}(\delta r) \\
&+ \left(\frac{1}{\tau_{\mathrm{r}}^{\mathrm{t}}(r)} + \frac{1}{\tau_{\mathrm{nr}}^{\mathrm{t}}(r)}\right)\left(\exp\left(\frac{E_{\mathrm{b}}(r)^{\mathrm{t}} - E_{\mathrm{g}}(r)}{k_B T}\right) - p^{\mathrm{t}}(r)\right) \\
&+ \frac{p^{\mathrm{s}}(r)}{\tau_{\mathrm{ISC}}(r)} - \frac{p^{\mathrm{t}}(r)}{\tau_{\mathrm{ISC}}(r)} \cdot \exp\left(\frac{E_{\mathrm{b}}^{\mathrm{s}}(r) - E_{\mathrm{b}}^{\mathrm{t}}(r)}{k_B T}\right) \\
&- \frac{p^{\mathrm{t}}(r)\left(p^{\mathrm{e}}(r) + p^{\mathrm{h}}(r)\right)}{\tau_{\mathrm{TPQ}}(r)} - \frac{\left(p^{\mathrm{t}}(r)\right)^2}{\tau_{\mathrm{TTA}}(r)} \\
&+ (1 - g_{\mathrm{Rec}}(r))\left(\frac{p^{\mathrm{e}}(r) p^{\mathrm{h}}(r)}{\tau(r)} - \frac{p^{\mathrm{t}}(r)}{\tau(r)} \exp\left(-\frac{E_{\mathrm{b}}(r)^{\mathrm{t}}}{k_B T}\right)\right) + (1 - g_{\mathrm{Opt}}(r)) G(r)
\end{aligned} \tag{4.25}$$

where most parameters are now continuous functions in state space. Note the use of $-\delta r$ as the second argument in the terms describing transport away from r which denotes reverse direction of δr. The special way to write the initial state in the first transport terms as $r - \delta r$ will be clarified soon. While the first two lines of (4.25) describe interactions over distances δr, all the other terms are completely local in nature and are not affected by the following treatment. The assumption is made that there exists a $\epsilon > 0$ such that

$$\tilde{\omega}(r', \delta r) \approx 0 \qquad \text{for } |\delta r| > \epsilon \tag{4.26}$$

$$\tilde{\omega}(r' + \Delta r, \delta r) \approx \tilde{\omega}(r', \delta r) \quad \text{for } |\Delta r| < \epsilon \tag{4.27}$$

where (4.26) means that only short jumps are possible and transfer rates decay quickly, whereas (4.27) stands for the assumption that rates do not vary strongly from state to state in their vicinity. These ultimately result in the fact that the final solution $p^{\mathrm{t}}(r)$ should also vary slowly over r. Note that while δr denotes a distance between two states over which transport occurs, $r + \Delta r$ denotes simply a state in the vicinity of r.

If these assumptions are met, the first transport terms in (4.25) can be approximated by a Taylor-series in δr for small δr around r

$$\begin{aligned} \int \tilde{\omega}(r - \delta r, \delta r) p^{\mathrm{t}}(r - \delta r) \mathrm{d}(\delta r) \approx & \int \tilde{\omega}(r, \delta r) p^{\mathrm{t}}(r) \mathrm{d}(\delta r) \\ & - \int \frac{\partial}{\partial r} \left[\tilde{\omega}(r, \delta r) p^{\mathrm{t}}(r)\right] \cdot \delta r \cdot \mathrm{d}(\delta r) \\ & + \frac{1}{2} \int \frac{\partial^2}{\partial r^2} \left[\tilde{\omega}(r, \delta r) p^{\mathrm{t}}(r)\right] \cdot \delta r^2 \cdot \mathrm{d}(\delta r) + \mathcal{O}\left(\delta r^3\right) \end{aligned} \tag{4.28}$$

which is truncated after the first two terms. This expression inserted back into the Master equation yields (only showing one transport integral)

$$\begin{aligned} & \int \left[\tilde{\omega}(r - \delta r, \delta r) p^{\mathrm{t}}(r - \delta r) - \tilde{\omega}(r, -\delta r) p^{\mathrm{t}}(r)\right] \mathrm{d}(\delta r) \\ = & \int \tilde{\omega}(r, \delta r) p^{\mathrm{t}}(r) \mathrm{d}(\delta r) \\ - & \int \frac{\partial}{\partial r} \left[\tilde{\omega}(r, \delta r) p^{\mathrm{t}}(r)\right] \cdot \delta r \cdot \mathrm{d}(\delta r) \\ + & \frac{1}{2} \int \frac{\partial^2}{\partial r^2} \left[\tilde{\omega}(r, \delta r) p^{\mathrm{t}}(r)\right] \cdot \delta r^2 \cdot \mathrm{d}(\delta r) \\ - & \int \tilde{\omega}(r, -\delta r) p^{\mathrm{t}}(r) \mathrm{d}(\delta r) \end{aligned} \tag{4.29}$$

If it is assumed that transport is symmetric then $\tilde{\omega}(r, -\delta r) = \tilde{\omega}(r, \delta r)$ and the first and last integral on the right hand side of (4.29) cancel each other. The physical interpretation of the assumptions made up to now basically say that transport happens in a single homogeneous material as interfaces would violate (4.27) and disorder would introduce strong asymmetries in transfer rates.

The two transport terms remaining if all these assumptions are fulfilled form on their own a *Fokker-Planck* equation commonly denoted as (not including local terms)

$$\frac{\partial p(r)}{\partial t} = -\frac{\partial}{\partial r} \left[D^{(1)}(r) p(r)\right] + \frac{\partial^2}{\partial r^2} \left[D^{(2)}(r) p(r)\right] \qquad \text{(1D)} \tag{4.30}$$

$$\frac{\partial p(\boldsymbol{r})}{\partial t} = -\sum_i \frac{\partial}{\partial r_i} \left[D_i^{(1)}(\boldsymbol{r}) p(\boldsymbol{r})\right] + \sum_{ij} \frac{\partial^2}{\partial r_i \partial r_j} \left[D_{ij}^{(2)}(\boldsymbol{r}) p(\boldsymbol{r})\right] \qquad \text{(3D)} \tag{4.31}$$

where $D^{(1)}$ is the drift-coefficient (-vector) and $D^{(2)}$ the diffusion-coefficient (-matrix) given by

$$D^{(n)}(r) = \frac{1}{n!} \int \tilde{\omega}(r, \delta r) \cdot \delta r^n \cdot \mathrm{d}(\delta r) \tag{4.32}$$

The first term in the 3D Fokker-Planck equation result from the gradient $\nabla(F(\boldsymbol{r}))$ and the second from the *Hessian*

$$H = \begin{bmatrix} \frac{\partial F(\boldsymbol{r})}{\partial r_1^2} & \cdots & \frac{\partial F(\boldsymbol{r})}{\partial r_1 r_n} \\ \vdots & \ddots & \vdots \\ \frac{\partial F(\boldsymbol{r})}{\partial r_n r_1} & \cdots & \frac{\partial F(\boldsymbol{r})}{\partial r_n^2} \end{bmatrix}$$

with $F(\boldsymbol{r}) = \tilde{\omega}(\boldsymbol{r}, \boldsymbol{\delta r})p(\boldsymbol{r})$ followed by integration.

If the above assumptions hold and transport is symmetric then $\tilde{\omega}$ are symmetric functions in δr. By taking the convolution of the symmetric transfer rates and the antisymmetric function δr the result is zero and the drift term vanishes. Due to the symmetry of δr^2 the diffusion term remains and governs exciton transport in homogeneous materials. From (4.32) it can be seen that the diffusion constant is directly related to the hopping rates defined by $\tilde{\omega}$. By only considering nearest neighbor hopping the integration can be taken yielding the common expression connecting hopping and diffusion [28]

$$D = \frac{1}{2n} a_0^2 \omega(a_0) \tag{4.33}$$

with n the dimensionality as the total rate is divided by the different directions and $\omega(a_0)$ is the total hopping frequency per unit time to the nearest neighbor molecule. This shows the advantage of the Master equation approach as also highly inhomogeneous materials can be modeled accurately and the assumptions needed to define a scalar constant diffusion coefficient do not need to be made.

4.3 Drift-diffusion charge carrier model

As already mentioned in the introduction, the Master equation approach is only applied to the exciton dynamics and relies on the charge carrier densities as external input. This input is itself simulated using the 1D drift-diffusion approach as included in setfos. The basic (scaled) equations to be solved are given as (taken from and using notation of [77])

$$\lambda^2 \nabla \psi = n - p + n_t - p_t \tag{4.34}$$

$$\nabla \cdot J_p = -R(n,p) - \frac{\partial p}{\partial t} \tag{4.35}$$

$$\nabla \cdot J_e = R(n,p) + \frac{\partial n}{\partial t} \tag{4.36}$$

$$J_p = -\mu_p(T, p, \nabla\psi)\left(\nabla p + g_3(p) p \nabla\psi\right) \tag{4.37}$$

$$J_n = -\mu_n(T, n, \nabla\psi)\left(\nabla n + g_3(n) n \nabla\psi\right) \tag{4.38}$$

with

$$\lambda^2 = \frac{U_t \varepsilon}{L^2 q N_0}$$

In order of appearance these are the Poisson, hole continuity, electron continuity, hole current and electron current equations. These can be calculated for single energy levels or using disorder models as well (for single energy levels the g_3 factor in (4.37) and (4.38) would disappear). In this notation n, p, n_t, and p_t are the electron, hole, trap electron and trap hole densities, respectively, ψ is the potential, J is the current and R is the recombination rate.

In addition to these equations models are needed which define recombination rates and mobilities. The standard approach for modeling recombination is through Langevin recombination as given in (3.3) and described in section 3.1.2. Mobilities can be modeled with different levels of detail, such as simple constant mobility or also more elaborate models as described in section 2.2.3 in the beginning of this thesis.

Again, certain difficulties arise due to the different approaches of the microscopic 3D ME and this macroscopic 1D continuum model. The disorder in the DD model only enters through the mathematical definition of the DOS and some adjustments of the resulting mobility, injection etc. (macroscopic parameters) while in the ME case an independent realization of the random variables is drawn giving an *actual spatial variation* of energy levels leading to variations in the microscopic parameters such as hopping rates, and it is not guaranteed that both approaches are actually consistent. This could be alleviated by calculating the ME model multiple times with different realizations thus approaching a certain "mean" solution. Another point is the treatment of guest-host systems where dopants (guests) are randomly distributed inside the host-matrix. Something similar can be achieved in the DD model by modeling the guest material as trap states in the host layer, however, due to the 1D approach these will be continuously spread throughout the layer which introduces some ambiguity in the way e.g. how carrier densities are translated into the 3D ME grid. Furthermore, the treatment of the coupling between excitons and charge carriers, recombination, is of utmost importance as otherwise the two solutions are not consistent. As in the ME approach no formal distinction between materials is made and recombination is simply calculated as $\frac{p^e p^h}{\tau}$ no special treatment of e.g. dopant recombination is necessary. However, if the same dopants are defined as traps in the DD approach special models apply which govern the recombination in these trap states, therefore special attention is necessary to avoid inconsistencies.

Chapter 5

Implementation

In this chapter the actual implementation of the solver as `C++` code will be described. First an overview over the main workflow is given, followed by a more detailed description for each of the main classes determining the simulation process.

An overview of the complete program is given in fig. 5.1 where the main flow follows four main steps

1. Parse the input data from setfos (`setfosInputParser`)
2. Generate the grid with the respective materials (`Grid`)
3. Prepare the model related matrices and vectors (`Model`)
4. Solve the system either in steady-state or transient (`Solvers`)

where the namespace `CONSTANTS::` is used to identify some physical constants which are globally available for all classes, such as π, the Boltzmann constant k_B, the vacuum permittivity ε_0 and others. Currently, also some numerical constants are stored there such as grid spacing a_0 and Förster radius R_0^{F} as these are constants throughout the whole simulation, however, this should be changed in the future and these values should be defined in the respective classes as parameters.

In the current state of the code the model using the decoupled equations from section 4.2.4 is implemented in an independent instance of the code to avoid conflicts between it and the main model using the coupled equations, however, most of the code works exactly the same and there won't be much effort necessary to unify them in the future. An additional independent instance with its own code is the small program `TestAdaptiveRK` which is a small test-suite to test the implementations of the various numerical methods used for transient simulations, i.e.

- Explicit Runge-Kutta
- SDIRK
- ESDIRK
- ROW

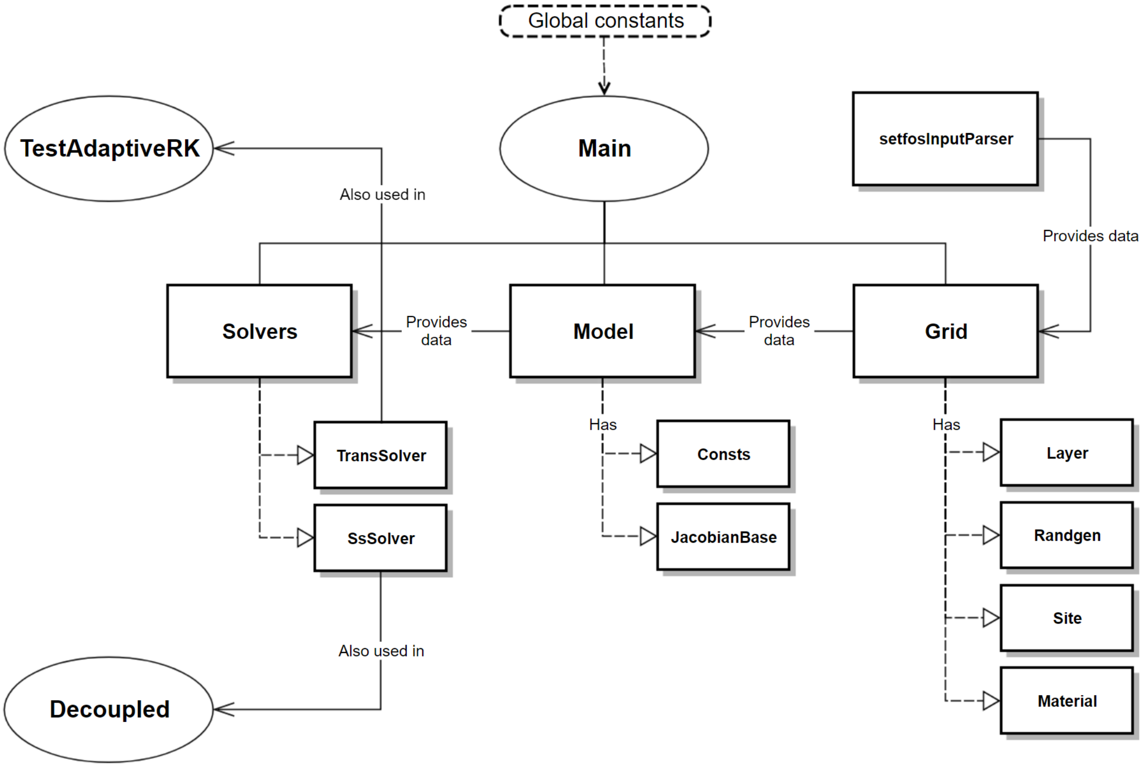

Figure 5.1: Implementation overview with the most important classes defining the simulation process.

with a more detailed description of the mathematical characteristics of each given in section 6.3.2.

This code heavily uses features provided by the `C++` library *Eigen* which is a template header library for linear algebra algorithms such as matrix-/vector-operations, numerical linear solvers, matrix decompositions etc. The library code is licensed under MPL2 and is therefore freely available even for commercial applications. Specifically, the classes `VectorXd` and `SparseMatrix` representing dynamically-sized vectors of type `double` and large sparse matrices, respectively, are used for the vectors and matrices in the code. In general, all floating-point numbers used are double-precision floats (`doubles`) occupying 8 B of memory each. In addition to the matrix-classes also the linear solvers used to solve e.g. the linearized Newton-equations are provided by *Eigen*. Additionally, many parts of the program are parallelized using *OpenMP* to make use of multiple cores on the CPU.

5.1 setfosInputParser

The first step before starting a simulation is to import the input data generated by setfos, i.e. profiles of the electron and hole densities and potential in the device which can be either static or transient. To achieve this, the class `setfosInputParser` can be used which provides the method `import_parameter()` taking the filename of the .txt-file from setfos as parameter. The files should be formatted in the way shown in the example files in tab. 5.1.

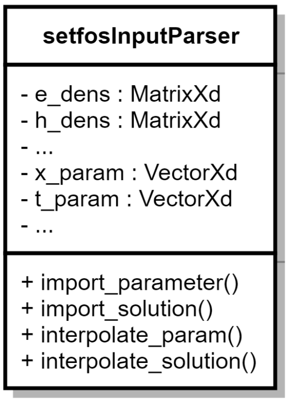

Figure 5.2: setfosInputParser overview.

(a) Example for the “transient” input format.

# …							
#							
# t(us)	x(nm)	n(cm^-3)	p(cm^-3)	Potential(V)	nt(cm^-3)	pt(cm^-3)	G(cm^-3s^-1)
0.00E+00	5.00E-01	7.03E-37	1.16E+19	-2.39E+00	0.00E+00	0.00E+00	0.00E+00
0.00E+00	1.50E+00	3.63E-36	2.26E+18	-2.35E+00	0.00E+00	0.00E+00	0.00E+00
0.00E+00	2.50E+00	1.09E-35	7.54E+17	-2.32E+00	0.00E+00	0.00E+00	0.00E+00
0.00E+00	3.50E+00	2.71E-35	3.02E+17	-2.30E+00	0.00E+00	0.00E+00	0.00E+00
⋮	⋮	⋮	⋮	⋮	⋮	⋮	⋮

(b) Example for the “steady-state” input format.

# Carrier … [cm^-3]						# Potential
# Column …:						# Column format:
# x [nm]	n	p	nt	pt	G	Potential [V]
5.00E-01	5.13E-18	1.16E+19	0.00E+00	0.00E+00	0.00E+00	-2.39E+00
1.50E+00	6.73E-17	2.26E+18	0.00E+00	0.00E+00	0.00E+00	-2.35E+00
2.50E+00	3.04E-16	7.54E+17	0.00E+00	0.00E+00	0.00E+00	-2.32E+00
3.50E+00	9.51E-16	3.02E+17	0.00E+00	0.00E+00	0.00E+00	-2.30E+00
⋮	⋮	⋮	⋮	⋮	⋮	

Table 5.1: Examples for parameter import files.

The imported parameters are then stored in the member variables, allowing for dynamically sized input data. The imported data is then directly spatially interpolated using the (private) member function `interp_param()` such that for each x-layer in the grid a well-defined value can be assigned. In between the input data points values are interpolated linearly, while for points outside the available data range constant extrapolation is used, i.e. for input data $\boldsymbol{d}_{\mathbf{in}}$ in the range $[n_{\text{in}}, m_{\text{in}}]$

$$\begin{aligned} \boldsymbol{d}(n) &= \boldsymbol{d}_{\mathbf{in}}(n_{\text{in}}) \quad \text{for}\, n < n_{\text{in}} \\ \boldsymbol{d}(m) &= \boldsymbol{d}_{\mathbf{in}}(m_{\text{in}}) \quad \text{for}\, m > m_{\text{in}} \end{aligned}$$

Not only parameters from setfos can be imported, but also exciton distributions (“solution”) using `import_solution()` where the import works very similarly to the parameter case, however, there are two different formats of how the imported values will be interpreted. Either the data is given similarly to the examples in tab. 5.1, one for each x-coordinate, or it can also be given as a simple (long) list of numbers (see tab. 5.2b). In the latter case the imported data will be interpreted as a "node-wise" solution where each imported value is directly assigned to the respective entry in the solution vector. This may be useful to import an older solution, e.g. as an initial value for a transient simulation, note however that if random variables such as E_b but also positions of guest sites is not taken into account this imported solution might be inconsistent with the new grid. The "layer-wise" interpolation works equally to the parameter interpolation.

(a) Example for the "layer-wise" input format.

Exciton density [cm^-3]
Column format:

# x [nm]	ps	pt	t_ps	t_pt
5.00E-01	5.13E-18	1.16E+19	0.00E+00	0.00E+00
1.50E+00	6.73E-17	2.26E+18	0.00E+00	0.00E+00
2.50E+00	3.04E-16	7.54E+17	0.00E+00	0.00E+00
3.50E+00	9.51E-16	3.02E+17	0.00E+00	0.00E+00
⋮	⋮	⋮	⋮	⋮

(b) Example for the "node-wise" input format.

ps(cm^-3)	pt(cm^-3)
5.13E-18	1.16E+19
6.73E-17	2.26E+18
3.04E-16	7.54E+17
9.51E-16	3.02E+17
⋮	⋮

Table 5.2: Examples for solution import files

5.2 Grid

The next basic step is to generate the grid on which the simulation will be carried out later. The interface to define it is provided by the class `Grid` which manages various other classes for different parts of the grid, namely `Material`, `Layer` and `Site` as shown in fig. 5.3. The first step is to add the materials used in the domain through the interface of the `Grid` class generating `Material` objects where each stores the relevant excitonic parameters of the material such as lifetimes and energy levels. Furthermore, it defines a set of `bool`s which are used to determine if certain mechanisms are active inside this material and if the disorder in the material is spatially correlated or not.

After all materials are defined, layers can be added one by one along the x-axis where for each a `Layer` object is generated storing information about the layer such as thickness and material types but also providing an interface to quickly act on all the sites inside that specific layer. The most important method is `update_profiles()` which can update the carrier density and potential profiles inside the layer for a given time t by using the data stored in the `setfosInputParser` object. In addition to the `Layer` object the respective number of `Site` objects are created and stored in the `Grid` object (note that they are not stored in the `Layer`). These represent the most fundamental part of the grid, i.e. single grid points representing a single molecule, and store the relevant data such as local energy levels,

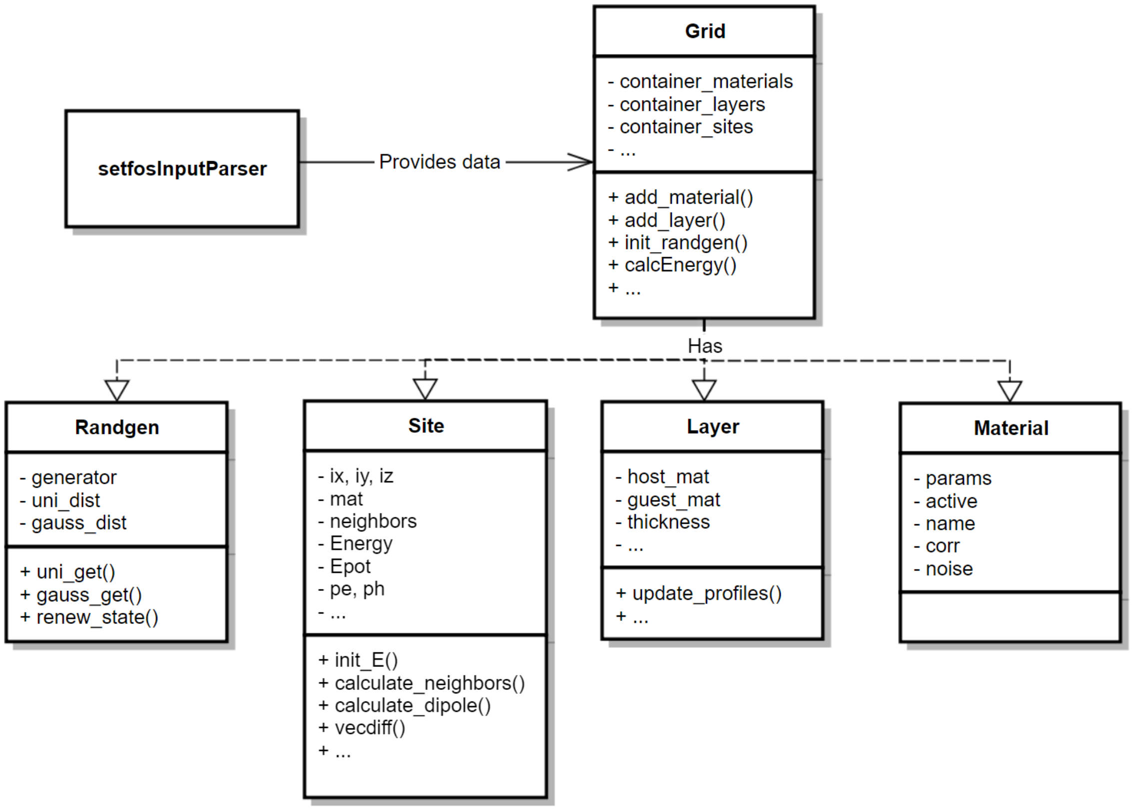

Figure 5.3: Grid overview.

local carrier density, indices, material type etc. (not exciton densities). The global index of a site is determined using the following scheme

$$i = (i_x m_y + i_y)\, m_z + i_z \tag{5.1}$$

with m_y, m_z the grid size in the lateral dimensions. Each object also stores a list of indices corresponding to its "neighbors", i.e. all sites within the coupling distance defined by R_c. In order to determine all these values, the class provides necessary methods

- `calculate_dipole()`: If the local material features uncorrelated disorder, this is a no-op. Otherwise it calculates a vector with length defined by the material and random orientation in space by sampling a Gaussian PDF for each component [78].
- `calculate_neighbors()`: Determines which other sites are in coupling range defined by R_c taking into account periodic boundary-conditions at y- and z-faces creating a neighbor-list.
- `vecdiff()`: Determines the distance between `*this` and a given different site, taking into account periodic boundary conditions.
- `init_E()`: Calculates the local energy levels according to (4.12) and (4.13) where depending on the material type the random component for the carriers is given by (2.4) or (4.15), where in the latter the case the previously calculated dipole-vectors are used.

The layers can be either generated with a single material or a combination of two materials (guest-host system) where the density of the guest material can be specified. The guest molecules will then be randomly distributed in the grid either with a constant density or a linear gradient as shown in fig. 5.4.

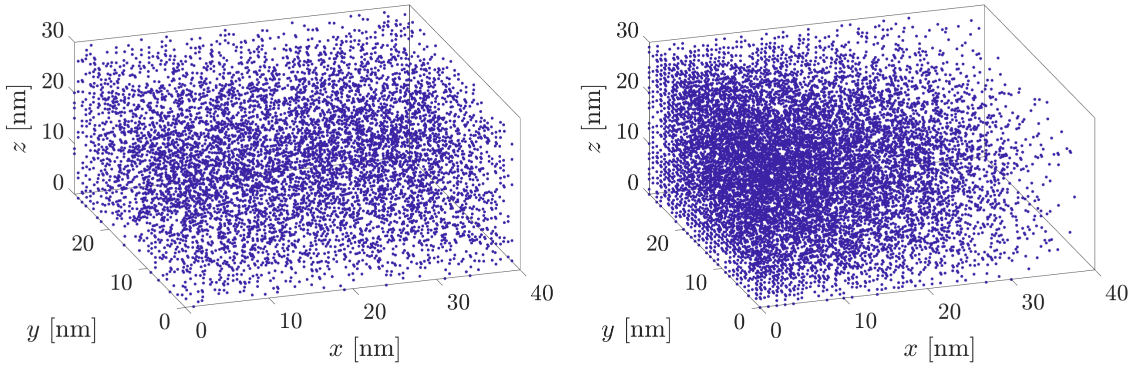

(a) Constant $\rho = 0.2$. **(b)** Linear distribution with $\rho_l = 0.6$ and $\rho_r = 0$.

Figure 5.4: Random distribution of guests in a guest-host system. The guest distribution can have either constant density or a linear density gradient.

The `Grid` object also stores a number of `Randgen` objects in order to ensure thread-safety in multithreaded environments where random numbers are used, generated during `init_randgen()`. Each contains a `default_random_engine` object (normally `mt19937`) seeded either by a user specified seed or a generated one from a `random_device`, which feeds a `uniform_real_distribution` and `normal_distribution` from which random numbers $\xi \sim \mathcal{U}(0, 1)$ and $\xi \sim \mathcal{N}(0, 1)$, respectively, can be obtained.

5.3 Model

The `Model` class manages all the aspects which are connected to the mathematical model from (4.7) and (4.8) such as storing the vector of unknown exciton densities $\boldsymbol{p}$ (denoted by `x` in the code), the system's Jacobian in the `Eigen::SparseMatrix J` and also the constant terms (independent of $\boldsymbol{p}$) consisting of recombination and optical generation in the vector `consts` as these are not yet stored in `J`. The class itself provides interfaces to initialize and update the matrices and vectors as well as to evaluate $\boldsymbol{f}(t, \boldsymbol{p})$ and its partial derivative with respect to time ${}^{\partial \boldsymbol{f}}/_{\partial t}$. One point worth mentioning is the way the functions are evaluated. Due to the polynomial form of the Master equations the functions can be directly evaluated using the stored matrices and vectors if a small correction is added as given in (6.8).

The class `Consts` is a very simple class storing two `Eigen::VectorXd` containing only the parts which are independent of time (detailed balance terms) as well as the final vector. The `init()` function simply calls `constrb_const()` which calculates all the time-independent terms followed by a call to `update()` to also add the time-dependent terms at the current timestep.

The `Jacobian` class represents, as the name says, the Jacobian of the Master equations. Internally, it has a member variable called `mat` which is of type `Eigen::SparseMatrix<double, Eigen::RowMajor>`, where the row-major format is chosen such that matrix-vector multiplications are multithreaded by *Eigen* and with it also

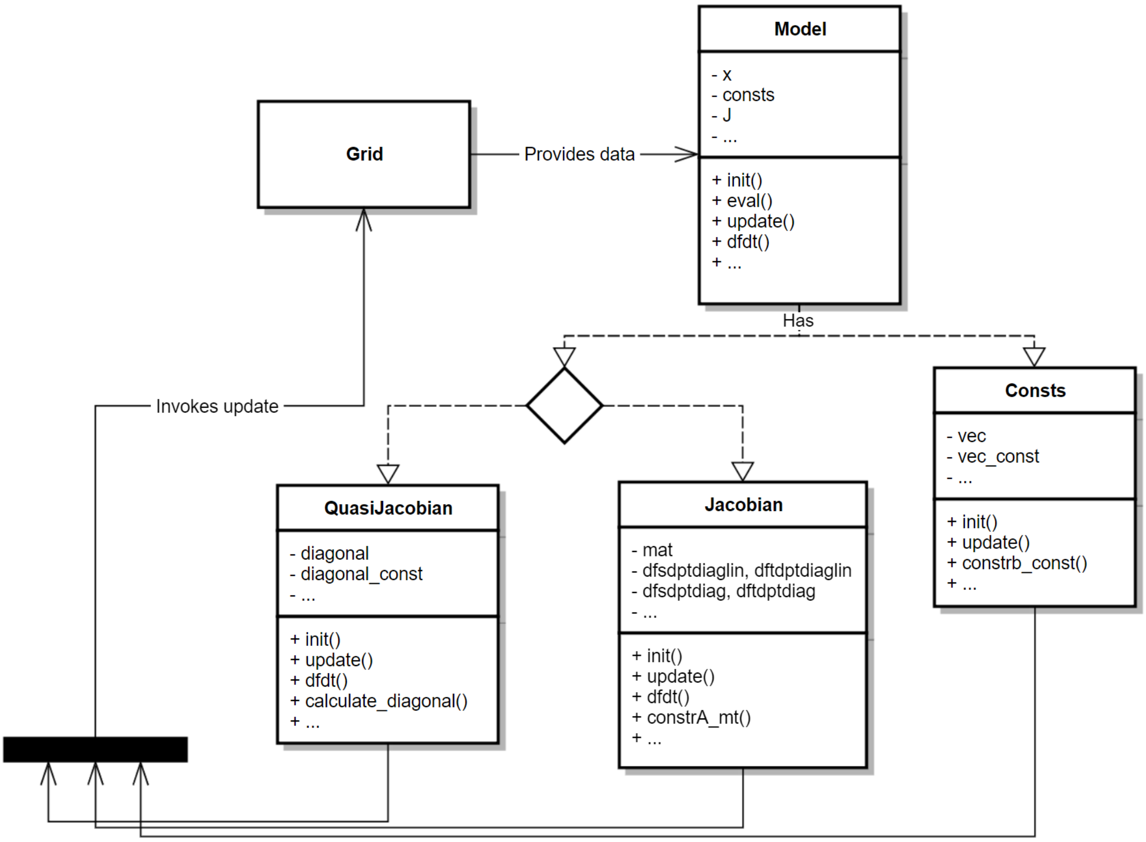

Figure 5.5: Model overview.

the iterative Krylov-subspace solvers. Parts of the matrix which stay constant over the whole simulation are constructed by `constrA_mt()`. The vectors with the cryptic names `dfsdptdiaglin` and `dftdptdiaglin` store the time independent and linear parts of $\mathrm{d}\boldsymbol{f}^{\mathrm{s}}/\mathrm{d}\boldsymbol{p}^{\mathrm{t}}$ and $\mathrm{d}\boldsymbol{f}^{\mathrm{s,t}}/\mathrm{d}\boldsymbol{p}^{\mathrm{s,t}}$ (i.e. the main diagonal) which will undergo updates later, whereas their counterparts without the `-lin` store the pointers to the respective entries. These two together allow for very fast $\mathcal{O}(1)$ access and updates of the Jacobian for changed $(t, \boldsymbol{p})$ where it was utilized that the positions of the entries undergoing changes is well known in advance. This together with the easy way to express $\boldsymbol{f}(t, \boldsymbol{p})$ using the Jacobian leads to the fact that every evaluation of the Master equations in the code is realized by an update of the Jacobian and constant terms followed by (6.8). The final important member function of this class is `dfdt()` which calculates the partial time derivatives as defined in (6.49).

Instead of the normal `Jacobian` where the matrix is stored explicitly in memory one can also use a similar class `QuasiJacobian` where no such matrix exists. Instead, in the case of matrix×vector products as needed in the iterative linear solvers, the entries which are needed in the operation are calculated on-the-fly in order to reduce memory usage (so-called *matrix-free* methods). This is not completely true as the main diagonal is still precomputed by using `calculate_diagonal()` as otherwise all the transport terms corresponding to a certain site would need to be computed every time the diagonal element is called (see the $\sum \omega$ terms in (4.7), (4.8)).

One aspect about the `update()` methods in all of these classes is worth mentioning. These are called with a parameter defining the current timestep. When called, these methods will actually first call `update_profiles()` for each layer stored in the grid. These will then read the data stored in the `setfosInputParser` and again linearly/constantly interpolate/extrapolate the profiles and update the values stored in the `Sites` such as $q\Phi_i$, p^{e} etc. as well as their respective time derivatives.

5.4 Solvers

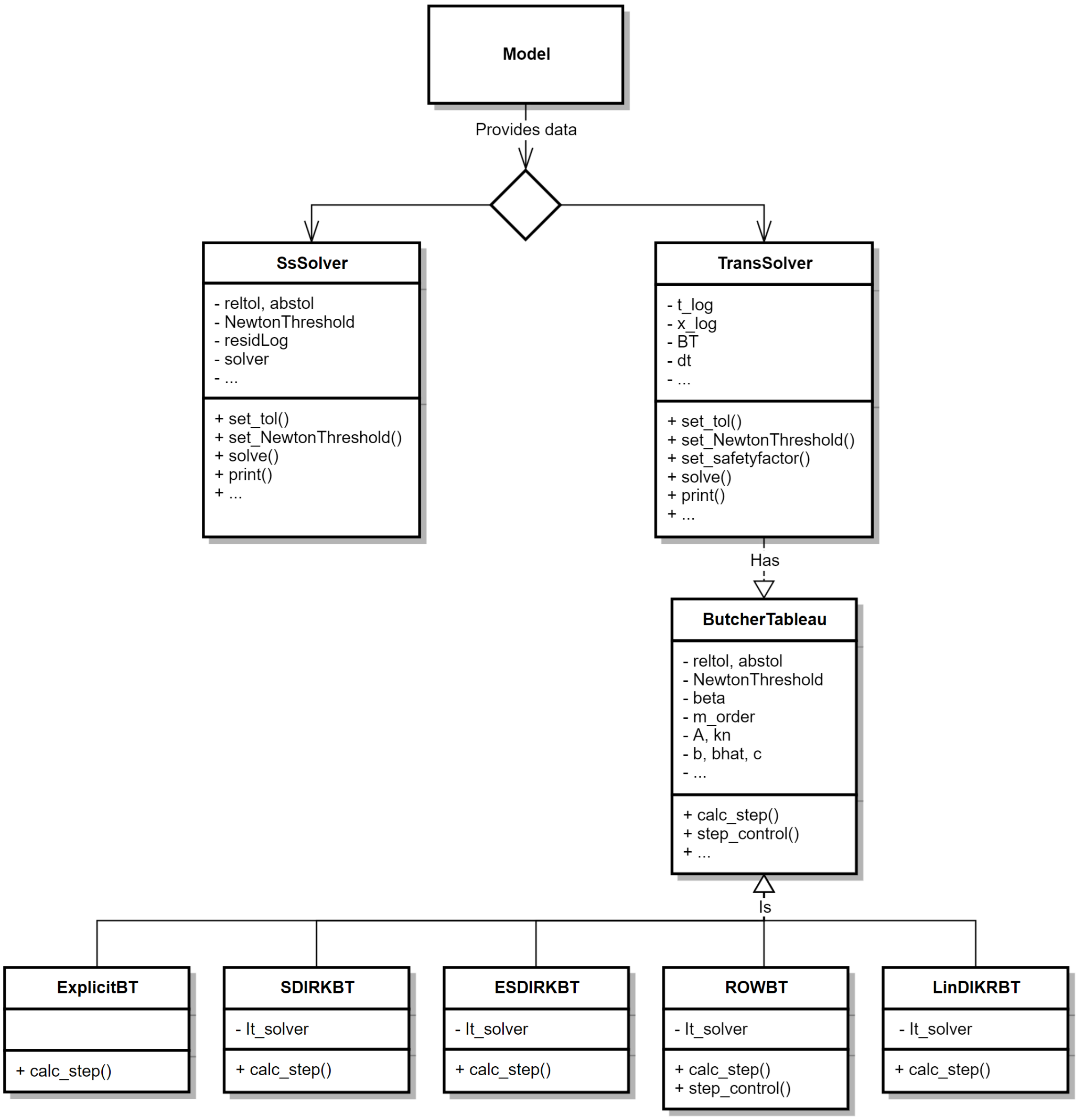

Figure 5.6: Solvers overview.

Depending on the needs, one is only interested in the final equilibrium solution at steady-state, or the actual temporal evolution of the exciton densities are of interest. For these two possibilities the classes `SsSolver` and `TransSolver` provide the necessary interface. The class solving for steady-state is quite simple as it basically only consists of a Newton iteration. By using the member functions `set_tol()` and `set_NewtonThreshold()` the member variables `reltol, abstol` and `NewtonThreshold` can be set in the solver. Those together define the convergence criteria where they correspond to β, α and τ in (6.13). During the iteration the displacement is recorded and stored in the `std::vector<double> residLog`. After the solution is obtained the results are written to a file by calling `print()`. There are three files written:

- <*setname*>_residual.txt: A text file with the contents stored in the `residLog` vector
- <*setname*>_data.bin: A binary file storing all the computed data column-wise in single-precision
- <*setname*>_varunits.txt: A text file where the information about the different columns of *setname*_data.bin is stored with variable names and units

The exported data includes the exciton densities but also some post-processed data (single terms of the Master equations representing different mechanisms) and local parameters (such as random energy contributions and carrier densities).

For transient simulation the second solver class `TransSolver` was implemented which employs a very similar interface additionally giving the option to set a safety factor β_s for stepsize control (see (6.41)). In terms of member variables they differ though as the `TransSolver` class does not yet store many specific control variables except the initial timestep `dt`, instead, it only stores a matrix `x_log` where the computed results for each timestep are stored alongside the vector `t_log` for the used timesteps themselves. The computational details are stored in another class `ButcherTableau` which is referenced in the `TransSolver` object. The `ButcherTableau` class represents as the name says a Butcher tableau which defines the used Runge-Kutta method and stores the specified tolerances as well as the specific coefficients of the method in its variables `A, c, b` and `bhat`. Furthermore, it has a temporary storage for the computed slopes `kn` during the integration steps. It features an internal method `step_control()` which implements the controller from (6.41) with additional safeguards such as $h_{\text{new}} <= 2h$ and $h > 0$ where h is the stepsize. The method `calc_step()` is only a virtual function defined specifically in the inheriting classes `ExplicitBT, SDIRKBT, ESDIRKBT, ROWBT` and `LinDIRKBT`.

All of them implement the basic Runge-Kutta scheme given in (6.35) and (6.36), except the ROW-methods which use a slightly different formulation where the details about all the numerical schemes are described in 6.3.2. As all of them are implicit methods except the ones in the `ExplicitBT` class a linear solver is needed to solve the linear system of equations where in the `SDIRKBT` and `ESDIRKBT` classes even a nonlinear Newton solver is implemented. For the solution of the linear equations an iterative BiCGSTAB algorithm is used. Note that `ROWBT` overrides the inherited `step_control()` method due to the aforementioned slightly different formulation. By calling the `solve()` function of the `TransSolver` these underlying functions defined in the inheriting classes are activated.

5.5 Independent programs

As already mentioned in the beginning, in the current state of the code there are two programs which are independent from the main one. The first is the one implementing the decoupled singlet and triplet equations and the second is a small test-suite for the transient solvers using scalar test ODEs. Whereas the former can and should be easily implemented into the main program, the latter is not meant to become part of the exciton solver.

The decoupled solver shall be described first, however only briefly, as the code is essentially the same except for the implementation of the model, i.e. the construction of the Jacobian and the vector storing the constant terms. As this model is anyway not used for transient simulations the whole time-dependency of the input data and transient solvers are not part of the code. The governing equation is given in (4.19) and the expression for the Jacobian in (4.20). The difficulty is mainly the computation of the Jacobian which needs to be done in some steps. First, all the underlying matrices appearing in (4.20) need to be created which is quite similar to the `constrA_mt()` as the matrices $\boldsymbol{M}^{\mathrm{s}}$ and $\boldsymbol{M}^{\mathrm{t}}$ have the same form as the upper left and lower right block diagonals of the original Jacobian. Computing the final matrix then is done calculating these steps (in code syntax):

$$\begin{aligned}
&\boldsymbol{J} = \boldsymbol{M}^{\mathrm{s}}(\boldsymbol{D}_{\mathrm{ISC}}^{\mathrm{s}})^{-1} \\
&\boldsymbol{J} = \boldsymbol{J} + 0.5\boldsymbol{I} \\
&\boldsymbol{J} = 2\boldsymbol{J}\boldsymbol{D}_{\mathrm{TTA}}\boldsymbol{p}^{\mathrm{t}} \\
&\boldsymbol{J} = \boldsymbol{J} - \left(\boldsymbol{M}^{\mathrm{s}}(\boldsymbol{D}_{\mathrm{ISC}}^{\mathrm{s}})^{-1}\boldsymbol{M}^{\mathrm{t}}\right) \\
&\boldsymbol{J} = \boldsymbol{J} + \boldsymbol{D}_{\mathrm{ISC}}^{\mathrm{s}}
\end{aligned}$$

It is very costly to compute these steps and due to the various temporaries created in the process the memory consumption is very high. Furthermore, this process is executed every time the Jacobian needs to be updated during a Newton iteration as it is not straightforward to distinguish the entries which are functions of p^{t} and which are not. As soon as the Jacobian is constructed, the constant terms are evaluated as

$$\boldsymbol{c} = \boldsymbol{M}^{\mathrm{s}}(\boldsymbol{D}_{\mathrm{ISC}}^{\mathrm{s}})^{-1}\left(\boldsymbol{b}_{\mathrm{Rec}}^{\mathrm{t}} + \boldsymbol{b}_{\mathrm{Opt}}^{\mathrm{t}} + \boldsymbol{D}_{\mathrm{Dec}}^{\mathrm{t}}\boldsymbol{b}^{\mathrm{t}}\right) - \left(\boldsymbol{b}_{\mathrm{Rec}}^{\mathrm{s}} - \boldsymbol{b}_{\mathrm{Opt}}^{\mathrm{s}} - \boldsymbol{D}_{\mathrm{Dec}}^{\mathrm{s}}\boldsymbol{b}^{\mathrm{s}}\right)$$

from where on the steady-state solution is obtained the same ways as in the coupled case.

The second program is a test suite where three scalar ordinary differential equations are solved and compared to the exact solution. The three ODEs with their respective solutions are given in (5.2), (5.3) and (5.4). Apart from solving different equations the implementation is of course designed to be as equal to the original one as possible in order to make sure that the results are comparable and conclusions about the original implementation might be drawn.

$$\frac{\mathrm{d}y}{\mathrm{d}t} = \lambda y \qquad \Longrightarrow y = A\exp(\lambda t) \tag{5.2}$$

$$\frac{\mathrm{d}y}{\mathrm{d}t} = \frac{2}{t}y + t^2 - 1 \quad \Longrightarrow y = t^3 + At^2 + t \tag{5.3}$$

$$\frac{\mathrm{d}y}{\mathrm{d}t} = \frac{4}{t^2} - \frac{6}{t}y + y^2 \Longrightarrow y = \frac{t^{-2} + 4At^{-5}}{t^{-1} + At^{-4}} \tag{5.4}$$

The first equation (5.2) is the famous Dahlquist test equation solved with initial condition $f(t = 0) = 1$ i.e. $A = 1$ and $\lambda = -3$ where λ can be decreased to make integration more difficult for solvers which do not provide A-stability (see section 6.3.1). The second equation is an example in [79] and features non-constant coefficients. This equation is solved with initial condition $f(t = -5) = -5$, i.e. $A = 5$. The final equation is a Riccati equation chosen due to its similarity to the Master equations (nonlinear with non-constant coefficients in the linear terms) with initial condition $f(t = 0.1) = 39.89$, i.e. $A = 0.27989$. Derivations of the ODE solutions can be found in the appendix A.3. Two examples of the results obtained with this code are shown in fig. 5.7. In case of the GRK4A the relative tolerance β was defined as given in the plot and $\alpha = 10^{-2}\beta$ and for the linearized implicit Euler stepsize was constant.

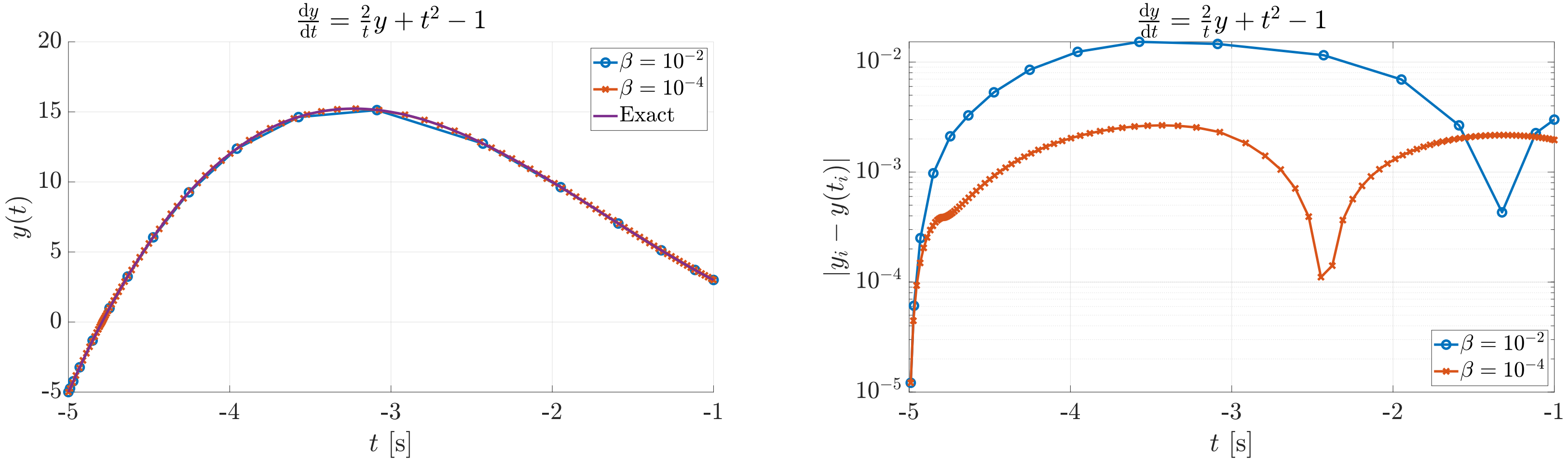

(a) Solution to (5.3) using GRK4A.

(b) Error to the exact solution of (5.3) using GRK4A.

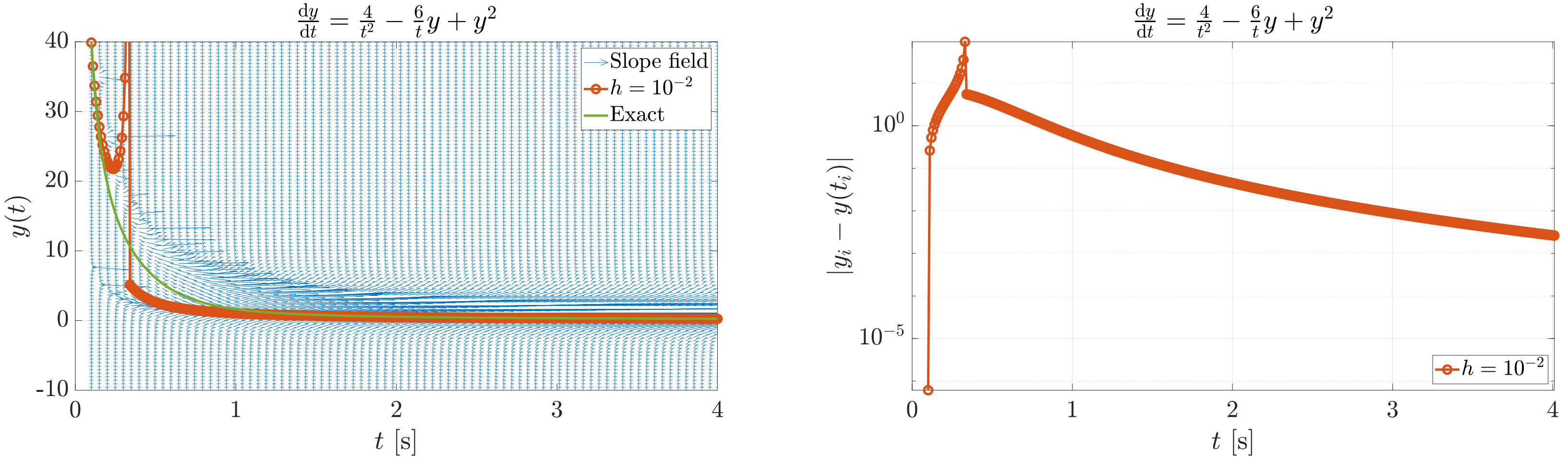

(c) Solution to (5.4) using the linearized implicit Euler.

(d) Error to the exact solution of (5.4) using the linearized implicit Euler.

Figure 5.7: Example solutions of the transient simulation test suite. For the Riccati equation also the slope field is plotted to show the narrow stability region. The method fails due to small integration errors moving it into the unstable region (all other methods succeeded).

Chapter 6

Numerical Methods

After setting up the mathematical model in chapter 4 and explaining the general implementation of the `C++` code, in this chapter a more detailed discussion of the mathematical methods used for solving the equations is given. In the first section the resulting matrices from the model and their properties and uses is explained. In the following the procedures used for solving the steady-state equations is shown along some ideas that were explored during the project. Finally, the approach for solving the equations under transient conditions is discussed alongside some stability considerations.

6.1 Matrix properties

As the coupled equations represent the main system to be solved, these will be discussed first, followed by some remarks about the more exotic approaches.

6.1.1 Coupled equations matrix

In order to solve (and evaluate, see later) the nonlinear equations (4.7) and (4.8) one needs to construct the Jacobian matrix $\boldsymbol{J} = {}^{\mathrm{d}\boldsymbol{f}}/_{\mathrm{d}\boldsymbol{p}}$ of the system where

$$\boldsymbol{p} = \begin{bmatrix} \boldsymbol{p}^{\mathrm{s}} \\ \boldsymbol{p}^{\mathrm{t}} \end{bmatrix}$$

Due to the polynomial structure of equations (4.7), (4.8) the Jacobian will have a very similar form as the equations themselves which makes it as cheap to compute as $\boldsymbol{f}(\boldsymbol{p})$. The Jacobian for the system is given in the following as

$$\boldsymbol{J} = \begin{bmatrix} \boldsymbol{J}^{\mathbf{ss}} & \boldsymbol{J}^{\mathbf{ts}} \\ \boldsymbol{J}^{\mathbf{st}} & \boldsymbol{J}^{\mathbf{tt}} \end{bmatrix} \tag{6.1}$$

with the sub-matrices $\boldsymbol{J}^{\mathbf{ss}}$, $\boldsymbol{J}^{\mathbf{ts}}$, $\boldsymbol{J}^{\mathbf{st}}$, $\boldsymbol{J}^{\mathbf{tt}}$ describing singlet↔singlet, triplet→singlet, singlet→triplet and triplet↔triplet interactions, respectively. These are given in detail by

$$\boldsymbol{J}^{\mathbf{ss}} = \begin{bmatrix} D_1^{\mathrm{s}} & \omega_{21}^{\mathrm{F,s}} + \omega_{21}^{\mathrm{D,s}} & \omega_{31}^{\mathrm{F,s}} + \omega_{31}^{\mathrm{D,s}} & \cdots & \omega_{N1}^{\mathrm{F,s}} + \omega_{N1}^{\mathrm{D,s}} \\ \omega_{12}^{\mathrm{F,s}} + \omega_{12}^{\mathrm{D,s}} & D_2^{\mathrm{s}} & \omega_{32}^{\mathrm{F,s}} + \omega_{32}^{\mathrm{D,s}} & \cdots & \omega_{N2}^{\mathrm{F,s}} + \omega_{N2}^{\mathrm{D,s}} \\ & & \vdots & & \\ & & \vdots & & \\ \cdots & \omega_{ji}^{\mathrm{F,s}} + \omega_{ji}^{\mathrm{D,s}} \cdots & D_i^{\mathrm{s}} & \cdots \omega_{ji}^{\mathrm{F,s}} + \omega_{ji}^{\mathrm{D,s}} & \cdots \\ & & \vdots & & \\ & & \vdots & & \\ \omega_{1N}^{\mathrm{F,s}} + \omega_{1N}^{\mathrm{D,s}} & \omega_{2N}^{\mathrm{F,s}} + \omega_{2N}^{\mathrm{D,s}} & \cdots & \omega_{N-1,N}^{\mathrm{F,s}} + \omega_{N-1,N}^{\mathrm{D,s}} & D_N^{\mathrm{s}} \end{bmatrix} \tag{6.2}$$

$$\boldsymbol{J}^{\mathbf{ts}} = \begin{bmatrix} \frac{\exp\left(\frac{\Delta E_{\mathrm{b},1}}{k_B T}\right)}{\tau_{\mathrm{ISC},1}} + \frac{p_1^{\mathrm{t}}}{\tau_{\mathrm{TTA},1}} & 0 & \cdots & 0 \\ 0 & \frac{\exp\left(\frac{\Delta E_{\mathrm{b},2}}{k_B T}\right)}{\tau_{\mathrm{ISC},2}} + \frac{p_2^{\mathrm{t}}}{\tau_{\mathrm{TTA},2}} & & \vdots \\ \vdots & & \ddots & 0 \\ 0 & \cdots & 0 & \frac{\exp\left(\frac{\Delta E_{\mathrm{b},N}}{k_B T}\right)}{\tau_{\mathrm{ISC},N}} + \frac{p_N^{\mathrm{t}}}{\tau_{\mathrm{TTA},N}} \end{bmatrix} \tag{6.3}$$

$$\boldsymbol{J}^{\mathbf{st}} = \begin{bmatrix} \frac{1}{\tau_{\mathrm{ISC},1}} & 0 & \cdots & 0 \\ 0 & \frac{1}{\tau_{\mathrm{ISC},2}} & & \vdots \\ \vdots & & \ddots & 0 \\ 0 & \cdots & 0 & \frac{1}{\tau_{\mathrm{ISC},N}} \end{bmatrix} \tag{6.4}$$

$$\boldsymbol{J}^{\mathbf{tt}} = \begin{bmatrix} D_1^{\mathrm{t}} & \omega_{21}^{\mathrm{F,t}} + \omega_{21}^{\mathrm{D,t}} & \omega_{31}^{\mathrm{F,t}} + \omega_{31}^{\mathrm{D,t}} & \cdots & \omega_{N1}^{\mathrm{F,t}} + \omega_{N1}^{\mathrm{D,t}} \\ \omega_{12}^{\mathrm{F,t}} + \omega_{12}^{\mathrm{D,t}} & D_2^{\mathrm{t}} & \omega_{32}^{\mathrm{F,t}} + \omega_{32}^{\mathrm{D,t}} & \cdots & \omega_{N2}^{\mathrm{F,t}} + \omega_{N2}^{\mathrm{D,t}} \\ & & \vdots & & \\ & & \vdots & & \\ \cdots & \omega_{ji}^{\mathrm{F,t}} + \omega_{ji}^{\mathrm{D,t}} \cdots & D_i^{\mathrm{t}} & \cdots \omega_{ji}^{\mathrm{F,t}} + \omega_{ji}^{\mathrm{D,t}} & \cdots \\ & & \vdots & & \\ & & \vdots & & \\ \omega_{1N}^{\mathrm{F,t}} + \omega_{1N}^{\mathrm{D,t}} & \omega_{2N}^{\mathrm{F,t}} + \omega_{2N}^{\mathrm{D,t}} & \cdots & \omega_{N-1,N}^{\mathrm{F,t}} + \omega_{N-1,N}^{\mathrm{D,t}} & D_N^{\mathrm{t}} \end{bmatrix} \tag{6.5}$$

with the main diagonal entries

$$D_i^{\mathrm{s}} = -\left(\sum_{f \neq i}^{N} \omega_{if}^{\mathrm{F,s}} + \sum_{d \neq i}^{N} \omega_{id}^{\mathrm{D,s}} + \frac{1}{\tau_{\mathrm{r},i}^{\mathrm{s}}} + \frac{1}{\tau_{\mathrm{nr},i}^{\mathrm{s}}} + \frac{1}{\tau_{\mathrm{ISC},i}} \right) \tag{6.6}$$

$$D_i^{\mathrm{t}} = -\left(\sum_{f \neq i}^{N} \omega_{if}^{\mathrm{F,t}} + \sum_{d \neq i}^{N} \omega_{id}^{\mathrm{D,t}} + \frac{1}{\tau_{\mathrm{r},i}^{\mathrm{t}}} + \frac{1}{\tau_{\mathrm{nr},i}^{\mathrm{t}}} + \frac{1}{\tau_{\mathrm{ISC},i}} \exp\left(\frac{E_{\mathrm{b},i}^{\mathrm{s}} - E_{\mathrm{b},i}^{\mathrm{t}}}{k_B T} \right) + \frac{2 p_i^{\mathrm{t}}}{\tau_{\mathrm{TTA},i}} \right) \tag{6.7}$$

It is worth to discuss some aspects of this matrix. First of all, it is important to note that $\boldsymbol{J}^{\mathrm{ss}}$ and $\boldsymbol{J}^{\mathrm{tt}}$ are *not* symmetric due to the asymmetric Boltzmann exponentials in (4.9) and

(4.10), therefore any special solving techniques for self-adjoint (Hermitian) matrices are not applicable. Furthermore, it may or may not be diagonally dominant depending on the magnitude of the chosen parameters.

Definition. Let $\boldsymbol{A} \in \mathbb{R}^{n\times n}$. $\boldsymbol{A}$ is called *self-adjoint* or *Hermitian* iff

$$\boldsymbol{A} = \boldsymbol{A}^H, \text{ i.e. } a_{ij} = \overline{a_{ji}} \quad \forall\, i,\, j$$

Definition. Let $\boldsymbol{A} \in \mathbb{R}^{n\times n}$. $\boldsymbol{A}$ is called *(strict) diagonally dominant* iff

$$|a_{ii}| \geq \sum_{j\neq i} |a_{ij}| \quad \forall\, i$$

However, due to the fact that all quantities in (4.7) and (4.8) are (physically) nonnegative the resulting Jacobian is a *Metzler matrix* which is typical for matrices describing continuous-time finite-state Markov processes like the Master equation.

Definition. Let $\boldsymbol{A} \in \mathbb{R}^{n\times n}$. $\boldsymbol{A}$ is called *Metzler matrix* iff

$$a_{ij} \geq 0 \quad \forall\, i \neq j$$

Because of the Metzler-property and because all the constant terms in the Master equations of the model are always nonnegative as well it follows that (in continuous time) the positivity of the exciton occupation numbers p_i^{s} and p_i^{t} is conserved over time, i.e.

$$\begin{matrix} p_i^{\mathrm{s}}(t=0) \geq 0 \\ p_i^{\mathrm{t}}(t=0) \geq 0 \end{matrix} \quad \Longrightarrow \quad \begin{matrix} p_i^{\mathrm{s}}(t) \geq 0 \\ p_i^{\mathrm{t}}(t) \geq 0 \end{matrix} \quad \forall\, t > 0$$

as all sink terms depend on the local exciton occupation number and vanish if $p = 0$.

Note that in (6.2) and (6.5) the matrices are presented in a form which is fully populated, i.e. all transport terms ω_{ij} are included. As mentioned in section 4.2.2, in order to reduce the coupling between sites a cutoff distance R_c is defined and transport terms are set to 0 for $R > R_c$. This makes the matrices $\boldsymbol{J}^{\mathrm{ss}}$ and $\boldsymbol{J}^{\mathrm{tt}}$ very sparse and gives them a banded structure with various sub-bands as shown in fig. 6.1. Note that even for a relatively small $R_c = 4\,\mathrm{nm}$ and grid size of $120 \times 30 \times 30$ the number of nonzeroes in the complete Jacobian is above 55'000'000.

This band structure emerges from the way sites are numbered, see (5.1). It is important that the last dimension over which the global index increases is x as there are no periodic boundary conditions applied at the x-faces, otherwise sites with the highest global index would be coupled with the lowest one and *vice-versa.*

Despite the large number of nonzeroes the Jacobian is easy to update as can be seen from (6.3) and (6.5) where only the two main diagonals of these sub-matrices are functions of $\boldsymbol{p}^{\mathrm{t}}$. By storing the addresses of these entries they can be updated individually in $\mathcal{O}(1)$. For transient simulations where one also needs to take into account temporal dependencies of $\boldsymbol{p}^{\mathrm{e}}(t)$, $\boldsymbol{p}^{\mathrm{h}}(t)$, $\boldsymbol{\Phi}(t)$ and $\boldsymbol{G}_{\mathrm{opt}}(t)$ this is not so easy anymore. The time dependencies on the charge carriers and optical generation are also easily taken into account as they are only present on the main diagonal of the full Jacobian and in the “constant” terms, however,

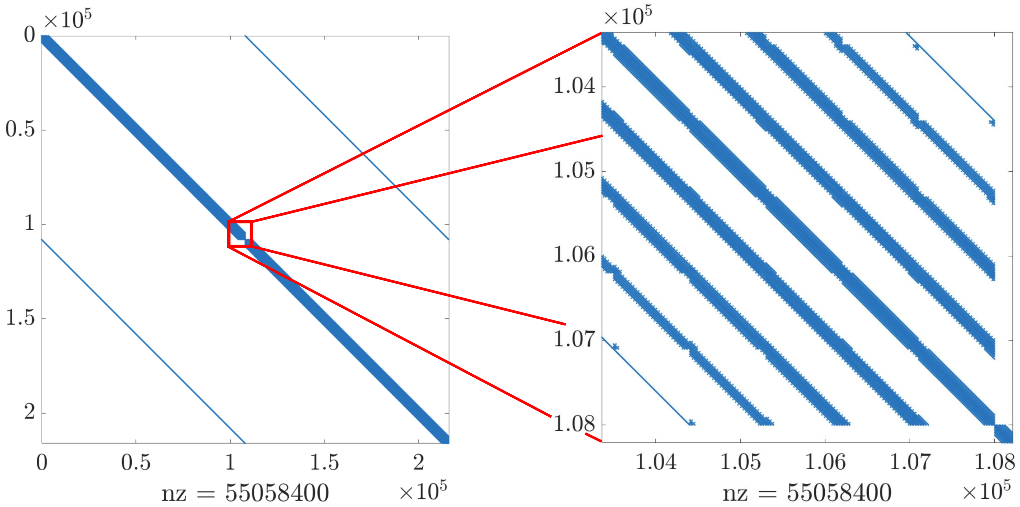

Figure 6.1: Pattern of the coupled Jacobian for a $120 \times 30 \times 30$ grid and $R_c = 4\,\mathrm{nm}$.

if one chooses to implement Dexter transport (and dissociation) as presented in 4.2.2 the energies would introduce a field-dependency and therefore a time-dependency of the transport terms. For an exact simulation one would then need to recalculate all transport terms in the Jacobian for each timestep which would increase the computational cost drastically.

Because of the polynomial structure of the Master equations the evaluation of the right-hand sides of (4.7), (4.8) can be done directly using the Jacobian in order to not recompute any of the transport terms if they are already stored in the matrix by calculating

$$\boldsymbol{f}(\boldsymbol{p}) = \boldsymbol{J}(\boldsymbol{p})\boldsymbol{p} - \boldsymbol{c} - \boldsymbol{f}_{\mathrm{nlin}}(\boldsymbol{p}), \qquad \text{with } \boldsymbol{f}_{\mathrm{nlin}}(\boldsymbol{p}) = \begin{bmatrix} \frac{(p_1^{\mathrm{t}})^2}{2\tau_{\mathrm{TTA},1}} \\ \vdots \\ \frac{(p_N^{\mathrm{t}})^2}{2\tau_{\mathrm{TTA},N}} \\ -\frac{(p_1^{\mathrm{t}})^2}{\tau_{\mathrm{TTA},1}} \\ \vdots \\ -\frac{(p_N^{\mathrm{t}})^2}{\tau_{\mathrm{TTA},N}} \end{bmatrix} \tag{6.8}$$

where $\boldsymbol{c}$ is the vector storing the (negative) “constant” terms and $\boldsymbol{f}_{\mathrm{nlin}}$ is a correction for the nonlinear terms.

6.1.2 Further matrices

There are also situations where other matrices emerge than the one described in the last section. Those will be shortly discussed here.

Decoupled equations matrix

As described in section 4.2.4 the Master equations for the two exciton species can be decoupled because of the simple diagonal structure of the coupling matrix $\boldsymbol{D}_{\mathrm{ISC}}^{\mathrm{s}} = \boldsymbol{J}^{\mathrm{st}}$ where the expression for the resulting Jacobian in that case is given by (4.20). In this expression the term denoted by 1 includes the sparse matrix multiplication of $\boldsymbol{M}^{\mathrm{s}}$ and $\boldsymbol{M}^{\mathrm{t}}$ where both of these matrices have the same structure as $\boldsymbol{J}^{\mathrm{ss}}$ and $\boldsymbol{J}^{\mathrm{tt}}$ as depicted in fig. 6.1. Because of the multiplication a large fill-in occurs where the bandwidth is broadened and the sub-bands get denser. This is shown in fig. 6.2 where only the upper-left corner of the main diagonal of $\boldsymbol{M}^{\mathrm{s}}$ and $\boldsymbol{J}^{\mathrm{t}}_{\mathrm{decoup}}$ is shown color-coded by the magnitude of the entries.

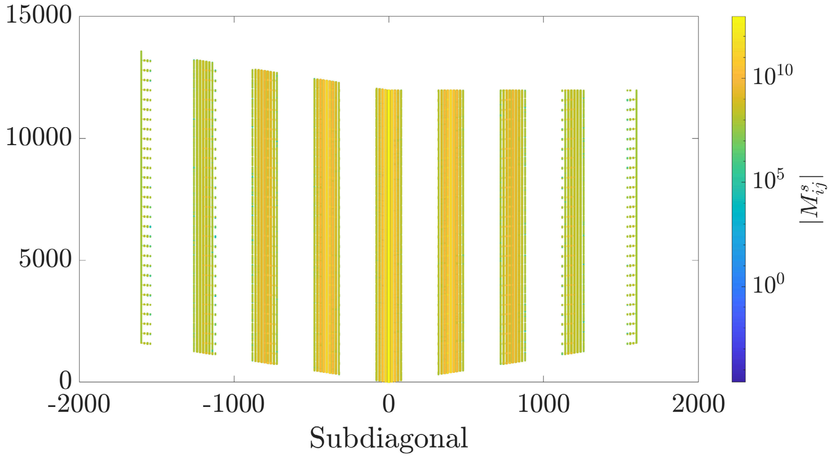

(a) $\boldsymbol{M}^{\mathrm{s}}$ matrix structure and magnitude.

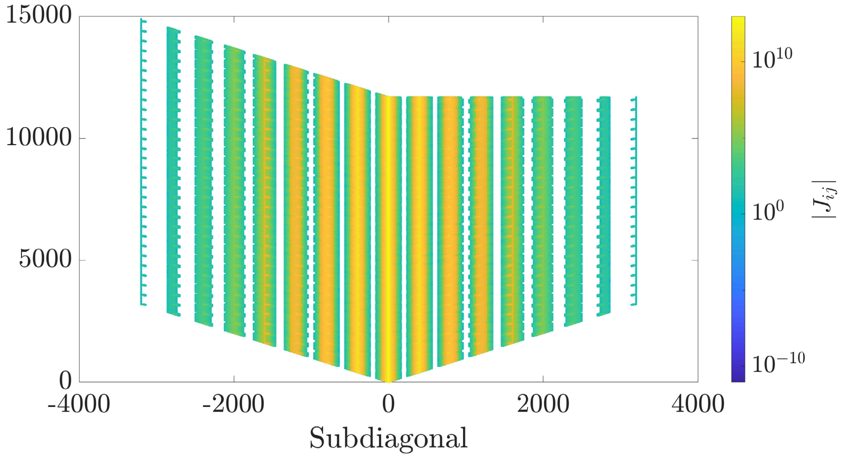

(b) $\boldsymbol{J}^{\mathrm{t}}_{\mathrm{decoup}}$ matrix structure and magnitude.

Figure 6.2: Fill-in of the decoupled Jacobian. Compare the number of filled sub-diagonals as well as the more spread large magnitudes in 6.2b.

For a $120 \times 20 \times 20$ grid the resulting Jacobian $\boldsymbol{J}^{\mathrm{t}}_{\mathrm{decoup}}$ has about 84’000’000 nonzero entries, i.e. much more already than the coupled Jacobian for a larger $120 \times 30 \times 30$ grid. Furthermore, during the construction of the matrix in the code (see section 5.5), various temporaries are created during the (not multithreaded) matrix calculation which lead to large memory consumption ($\sim 8\,\mathrm{GB}$ peak for a $120 \times 30 \times 30$ grid). In addition to the fill-in the dependency on the solution is spread over the whole range of matrix entries given by the structure of $\boldsymbol{M}^{\mathrm{s}}$ and therefore the cheap $\mathcal{O}(1)$ updates by storing the addresses is not straightforward anymore. If one would try to mitigate this problem of updating the Jacobian by employing certain numerical techniques such as Broyden rank(1)-updates [80], the problem emerges that the evaluation of the right-hand side of (4.19) is as expensive as the evaluation of the Jacobian and therefore these methods are of no use (as they are based on the assumption that the evaluation of the Jacobian ${}^{\mathrm{d}\boldsymbol{f}}/_{\mathrm{d}\boldsymbol{x}}$ is much more expensive *relative* to the evaluation of $\boldsymbol{f}(\boldsymbol{x})$ itself, as those evaluations are still needed for every iteration).

Matrix-free methods

As will be discussed later in section 6.2.2, for iterative Krylov-subspace solvers only matrix×vector products are necessary. Therefore, there is the option to use so-called *matrix-free* methods where the matrix is not stored explicitly in memory. Instead, the products of the elements needed are calculated on-the-fly during the matrix×vector operation, saving basically all the memory which would be occupied by the matrix itself. However, this is of course equivalent to a complete construction of the matrix for each operation and is therefore computationally expensive. In fig. 6.3 the solution time per iteration of the iterative linear solver is compared between the "normal" (matrix stored explicitly in memory) and the matrix-free version on a small $120 \times 15 \times 15$ grid. The results show that the computation time per iteration using matrix-free solvers is around 10× the computation time if the matrix is stored explicitly. This is due to the fact that the transport terms have to be calculated every time which include nontrivial operations such as `exp()`, `pow()` and `sqrt()`. Note that the amount of operations for each entry is constant, so the complexity is still $\mathcal{O}(np)$ given by the matrix×vector multiplication (p being the number of sub-diagonals).

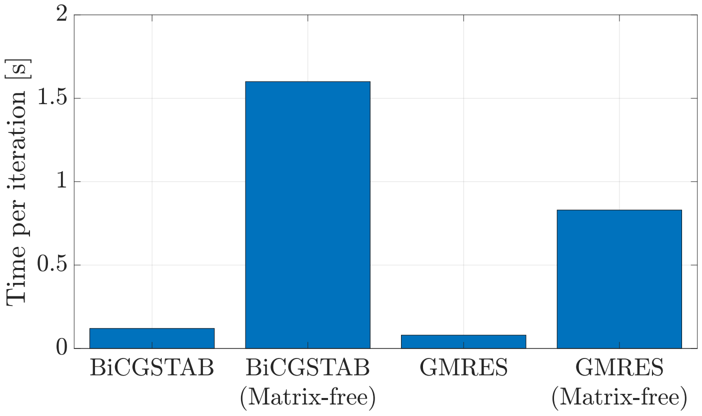

Figure 6.3: Iteration time for matrix free-solvers compared to their explicit counterparts.

Another difficulty is to obtain a preconditioner if the matrix is not available explicitly. One application where such a matrix-free version of the Jacobian could be useful is where a single matrix×vector product is necessary, such as to evaluate (6.8) during transient simulations, especially if one chooses to include the field-dependency of the Dexter hopping terms (or dissociation terms) where the Jacobian would frequently need to be updated almost completely anyways.

6.2 Steady-state solution

If only the equilibrium state of the device is of interest such as evaluation at different voltage points to calculate luminance vs. current curves, then the steady-state assumption can be applied and time derivatives are set to zero

$$\frac{\mathrm{d}\boldsymbol{p}^{\mathrm{s}}}{\mathrm{d}t} = \frac{\mathrm{d}\boldsymbol{p}^{\mathrm{t}}}{\mathrm{d}t} \equiv 0$$

The resulting equations can then be directly solved for the steady-state exciton distribution.

6.2.1 Newton algorithm

If one applies the steady-state condition to the equations (4.7) and (4.8) one needs to solve the nonlinear equations given by

$$\boldsymbol{f}(\boldsymbol{p}) = \boldsymbol{0} \tag{6.9}$$

where $\boldsymbol{f}(\boldsymbol{p})$ denotes the right-hand sides of (4.7) and (4.8). In order to solve this equation numerically one generally applies *Newton's method* where the nonlinear equation is sequentially linearized. The method is popular due to its simplicity and generally quadratic convergence in a neighborhood of the final solution. A short description of the method is given in the following. In order to solve a system of nonlinear equations as given by (6.9) the equations are linearized around a point $\boldsymbol{p}^{(0)}$

$$\boldsymbol{f}(\boldsymbol{p}) \approx \boldsymbol{f}(\boldsymbol{p}^{(0)}) + \left.\frac{\mathrm{d}\boldsymbol{f}}{\mathrm{d}\boldsymbol{p}}\right|_{\boldsymbol{p}^{(0)}} \left(\boldsymbol{p} - \boldsymbol{p}^{(0)}\right) + \mathcal{O}\left(\boldsymbol{p}^2\right) = \boldsymbol{0} \tag{6.10}$$

where the Taylor series of $\boldsymbol{f}(\boldsymbol{p})$ is truncated after the linear terms. (6.10) can be written by using the Jacobian matrix and rearranging

$$\boldsymbol{J}(\boldsymbol{p}^{(0)})\boldsymbol{\Delta p}^{(0)} = -\boldsymbol{f}(\boldsymbol{p}^{(0)}) \tag{6.11}$$

This is a linear equation which can be solved for $\boldsymbol{\Delta p}^{(0)} = \left(\boldsymbol{p} - \boldsymbol{p}^{(0)}\right)$ which leads to the following iterative scheme

$$\boldsymbol{p}^{(k+1)} = \boldsymbol{p}^{(k)} + \boldsymbol{\Delta p}^{(k)} \tag{6.12}$$

Using this scheme the vector $\boldsymbol{p}^{(k)}$ approaches the solution of (6.9) for a good initial guess $\boldsymbol{p}^{(0)}$ in the neighborhood of the solution to the nonlinear problem. There are various ways to determine if the solution has converged, one of the most popular is the *displacement condition* [81]

$$\left|\left|\boldsymbol{\delta}^{(k+1)}\right|\right| \leq \tau, \qquad \text{with } \delta_i^{(k+1)} = \frac{p_i^{(k+1)} - p_i^{(k)}}{\beta\left|p_i^{(k+1)}\right| + \alpha} = \frac{\Delta p_i^{(k)}}{\beta\left|p_i^{(k+1)}\right| + \alpha} \tag{6.13}$$

where $||\cdot||$ in (6.13) denotes a suitable norm such as a L_∞ or L_2 norm

$$||\boldsymbol{\delta}||_\infty = \max_i |\delta_i| \,, \qquad ||\boldsymbol{\delta}||_2 = \sqrt{\frac{1}{N}\sum_i \delta_i^2} \tag{6.14}$$

The scalars α, β and τ are absolute and relative tolerances and a tolerance ratio which is often $\tau = 1$. The absolute tolerance should be chosen small simply as a mean to prevent division by zero. However, the displacement condition simply checks that no change of the solution is occurring anymore, in order to check for the correctness of the obtained (converged) solution $\boldsymbol{p}^*$ it is a good idea to check $||\boldsymbol{f}(\boldsymbol{p}^*)||$ which should be close to zero.

6.2.2 Linear solution method

By linearizing the nonlinear equations in (6.9) we merely replaced one problem with another one, namely how the resulting linearized system should be solved. Due to the large size of the system in general for such a 3D problem with long-range interactions direct solution methods such as LU- or QR-decompositions are unfeasible due to the large fill-in of the decomposition matrices.

To mitigate the problems of the direct solvers one can employ an iterative linear *Krylov-subspace* solver where the linearized equation is itself solved iteratively. Due to the general shape of the Jacobian matrix, solvers able to deal with such matrices have to be chosen where two common possibilities are the *Generalized Minimum Residual* (GMRES) and *Bi-Conjugate Gradient Stabilized* (BiCGSTAB) methods (see [82] for more information). For both methods the convergence rate depends on the condition number κ where for a matrix $\boldsymbol{A} \in \mathbb{R}^{n\times n}$

$$\kappa(\boldsymbol{A}) = \frac{\sigma_{\max}(\boldsymbol{A})}{\sigma_{\min}(\boldsymbol{A})} \tag{6.15}$$

where $\sigma_{\max}(\boldsymbol{A})$ and $\sigma_{\min}(\boldsymbol{A})$ are the maximum and minimum singular values of the matrix $\boldsymbol{A}$. In order to minimize this ratio, one generally preconditions the system of equations by using a suitable *preconditioner*. Assume one wants to solve the system $\boldsymbol{A}\boldsymbol{x} = \boldsymbol{b}$ iteratively, then a good preconditioner $\boldsymbol{K}$ should have the following properties [83]:

- Either $\kappa(\boldsymbol{K}^{-1}\boldsymbol{A}) \approx 1$ (i.e. $\boldsymbol{K}$ ($\boldsymbol{K}^{-1}$) is a good approximation of $\boldsymbol{A}$ ($\boldsymbol{A}^{-1}$))
- Or the spectrum of $\boldsymbol{K}^{-1}\boldsymbol{A}$ consists of few eigenvalues (clusters)
- $\boldsymbol{K}\boldsymbol{z} = \boldsymbol{r}$ can be easily solved
- $\boldsymbol{K}$ can be easily constructed

Then one solves instead of the original system of equations an adjusted one depending on which type of preconditioning is chosen, i.e.

$$\boldsymbol{K}^{-1}\boldsymbol{A}\boldsymbol{x} = \boldsymbol{K}^{-1}\boldsymbol{b} \qquad \text{(Left preconditioning)} \tag{6.16}$$

$$\boldsymbol{A}\boldsymbol{K}^{-1}\boldsymbol{y} = \boldsymbol{b}, \qquad \boldsymbol{x} = \boldsymbol{K}^{-1}\boldsymbol{y} \qquad \text{(Right preconditioning)} \tag{6.17}$$

$$\boldsymbol{L}^{-1}\boldsymbol{A}\boldsymbol{U}^{-1}\boldsymbol{z} = \boldsymbol{L}^{-1}\boldsymbol{b}, \qquad \boldsymbol{x} = \boldsymbol{U}^{-1}\boldsymbol{z} \qquad \text{(Split preconditioning } \boldsymbol{K} = \boldsymbol{L}\boldsymbol{U}\text{)} \tag{6.18}$$

The actual implementation of such preconditioned systems actually adjusts the algorithm of the iterative Krylov-subspace solver and results in the *preconditioned GMRES / BiCGSTAB* algorithms where per iteration the system $\boldsymbol{K}\boldsymbol{z} = \boldsymbol{r}$ needs to be solved.

For the present problem various preconditioners were considered, namely

- ILUT
- (Block) Jacobi
  - Block full
  - Block simplified
- (Block) Gauss-Seidel
  - Block full
  - Block simplified
  - Block diagonal

The first preconditioner is constructed by a *threshold incomplete LU* (ILUT) factorization after [84] which is governed by two parameters p_{ILUT} and τ_{ILUT} controlling the maximum amount of fill-in and dropping of elements whose magnitudes are below the defined threshold, respectively. In this way an approximate LU factorization is carried out which can be used to approximate $\boldsymbol{A}^{-1}$ and to directly solve $\tilde{\boldsymbol{L}}\tilde{\boldsymbol{U}}\boldsymbol{z} = \boldsymbol{r}$ in each iteration. The two other types come from general fixed-point iteration techniques following the scheme

$$\boldsymbol{x}_{k+1} = \boldsymbol{G}\boldsymbol{x}_k + \hat{\boldsymbol{b}} \tag{6.19}$$

where $\boldsymbol{G}$ and $\hat{\boldsymbol{b}}$ are defined from the matrix-splitting $\boldsymbol{A} = \boldsymbol{K} - \boldsymbol{N}$

$$\hat{\boldsymbol{b}} = \boldsymbol{K}^{-1}\boldsymbol{b}, \qquad \boldsymbol{G} = \boldsymbol{K}^{-1}\boldsymbol{N} = \boldsymbol{I} - \boldsymbol{K}^{-1}\boldsymbol{A} \tag{6.20}$$

By inserting (6.20) in (6.19) it follows that the generating system of (6.19) is the left preconditioned system as given in (6.16). Therefore, preconditioning the iterative Krylov-subspace method by $\boldsymbol{K}$ is equivalent to evaluate one step of $\boldsymbol{A}\boldsymbol{z} = \boldsymbol{r}$ using Jacobi or Gauss-Seidel iteration. For the two considered methods, Jacobi and Gauss-Seidel iteration, $\boldsymbol{K}$ is given by

$$\boldsymbol{K}_{\mathrm{J}} = \boldsymbol{D}, \qquad \boldsymbol{K}_{\mathrm{GS}} = \boldsymbol{D} - \boldsymbol{E} \tag{6.21}$$

where $\boldsymbol{D}$ and $-\boldsymbol{E}$ are the main diagonal and the strict lower triangular part of $\boldsymbol{A}$. These can then be used as preconditioners for the iterative Krylov-subspace solver where they are especially strong for diagonally dominant matrices and very easy to construct as well as to invert. The block versions are simply defined by applying the concept to block matrices, e.g. taking the block diagonal of $\boldsymbol{A}$ for $\boldsymbol{D}$. This tries to exploit the block structure of the Jacobian as given in (6.1) where for the "full" block preconditioners the full $\boldsymbol{J}^{\mathrm{ss}}$ and $\boldsymbol{J}^{\mathrm{tt}}$ are taken whereas for the "simplified" ones only the sub-diagonals corresponding to the transport to nearest neighbors are kept additionally to the main diagonal, as these are expected to are large in magnitude. Block diagonal Gauss-Seidel finally is equivalent to the normal Jacobi preconditioner where the diagonal of $\boldsymbol{J}^{st}$ is also taken into account. The structures of the Jacobi- and Gauss-Seidel preconditioners is given in fig. 6.4.

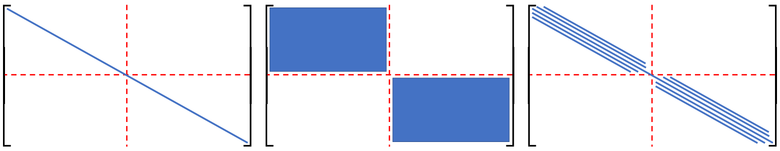

(a) Normal Jacobi. **(b)** Full block Jacobi. **(c)** Simplified block Jacobi.

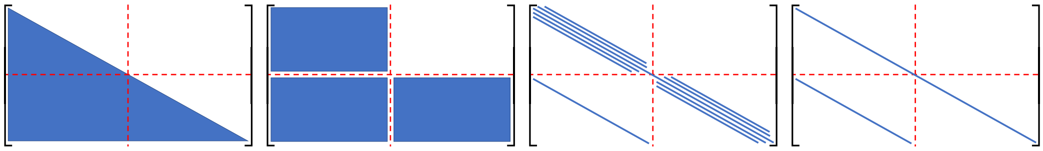

(d) Normal Gauss-Seidel. **(e)** Full block Gauss-Seidel. **(f)** Simplified block Gauss-Seidel. **(g)** Diagonal block Gauss-Seidel.

Figure 6.4: Structures of different preconditioners used for solving the linearized equations iteratively. Matrix entries which are kept are marked in blue.

6.2.3 Method performance

In order to check how these methods perform, an example stack was simulated with different parameters and preconditioners. The details about the physical parameters are given in section 7.2. In fig. 6.5 the convergence of the Newton method is shown graphically by plotting the displacement criteria from (6.13) alongside the evaluation of $\boldsymbol{f}(\boldsymbol{p})$. The first thing to note is the much faster convergence in case of low charge carrier densities compared to the case with high densities. This can be easily explained by looking at the norm of the right-hand side, depicted in orange. Due to the lower recombination in the case of lower carrier densities obviously the final exciton distribution will feature lower occupation numbers, therefore the initial guess $\boldsymbol{p} = \boldsymbol{0}$ is much closer to the final solution (compare $||\boldsymbol{f}(\boldsymbol{p}^{(0)})_{\text{high}}||_2 \approx 10^{19}$ vs. $||\boldsymbol{f}(\boldsymbol{p}^{(0)})_{\text{low}}||_2 \approx 1$). In both cases tolerances were chosen as $\beta = 10^{-11}$, $\alpha = 0$ and $\tau = 1$.

Regarding the solution of the linearized equations the number of iterations as well as the time needed for convergence of the Krylov-subspace solver are depicted in fig. 6.6 for both high and low carrier densities. Only the values for the first iteration of the Newton solver are shown. Note that the necessary residual for convergence is different in both cases as $||\boldsymbol{f}(\boldsymbol{p}^{(0)})||_2$ is different and the implemented convergence criterion in the notation of (6.11) is

$$\frac{||\hat{\boldsymbol{r}}^{(k)}||_2}{||\boldsymbol{f}(\boldsymbol{p}^{(k)})||_2} = \frac{||\boldsymbol{f}(\boldsymbol{p}^{(k)}) + \boldsymbol{J}^{(k)}\boldsymbol{\Delta p}^{(k)}||_2}{||\boldsymbol{f}(\boldsymbol{p}^{(k)})||_2} < \eta \tag{6.22}$$

where η is some user-specified tolerance value (here equal to machine epsilon). It is interesting to note that the relative performance of the ILUT-preconditioner is quite different in both cases. While in the cases of low carrier density it preconditions the iterative solver extremely well (more expensive to solve $\boldsymbol{Kz} = \boldsymbol{r}$ compared to e.g. Jacobi, therefore its temporal advantage is not as pronounced) in the second case this is not as clear anymore, where the simpler Jacobi and diagonal Block Gauss-Seidel achieve even slightly better performance. In both cases it is very clear though that the simplified Block Jacobi and -Gauss-Seidel do not yield any benefits. The full Block preconditioners have not been tested, they could be worth an attempt even though it probably will be very expensive to solve the system involving the preconditioner in the algorithm.

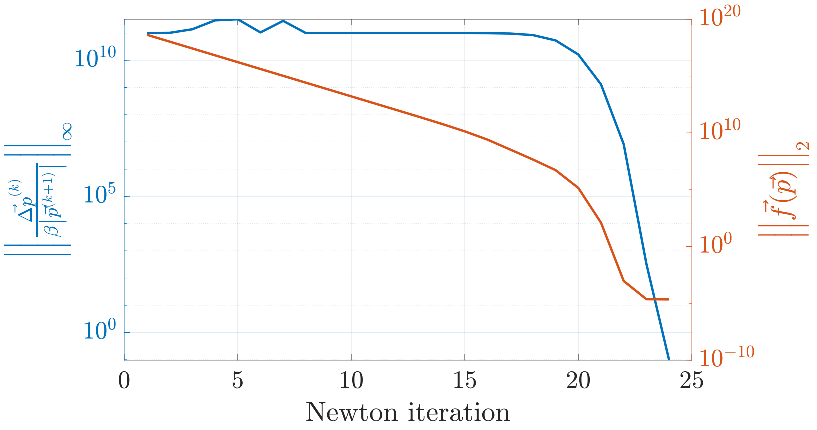

(a) High charge carrier densities.

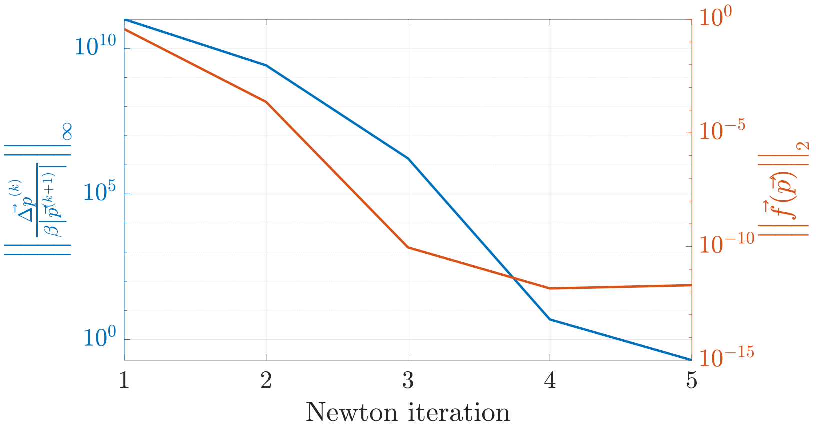

(b) Low charge carrier densities.

Figure 6.5: Convergence of the Newton method for high and for low charge carrier densities.

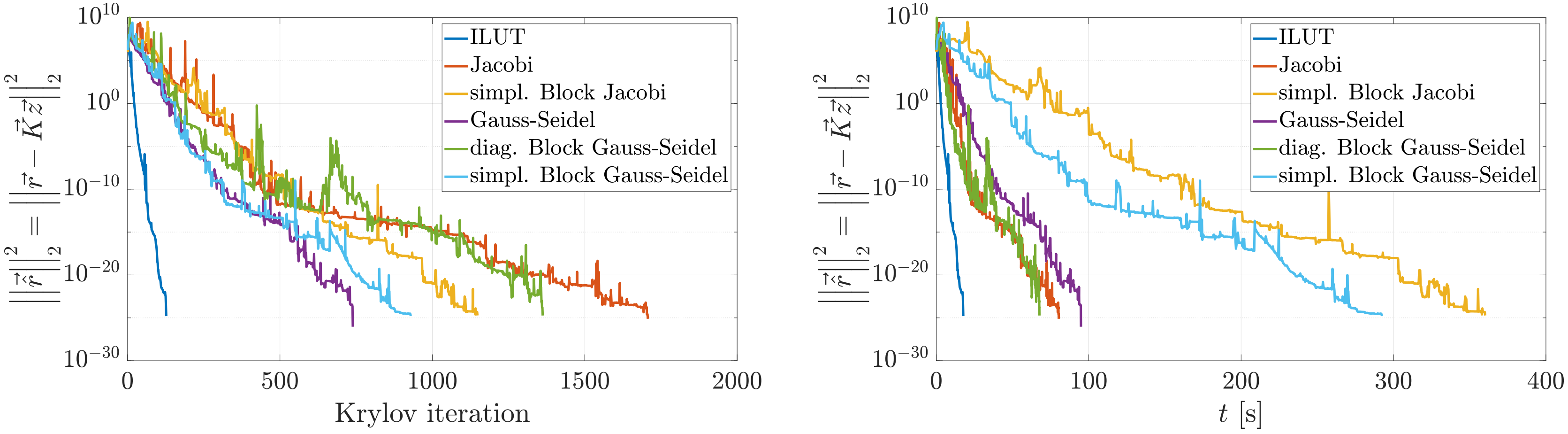

(a) Convergence versus iterations for low carrier density.

(b) Convergence versus time for low carrier density.

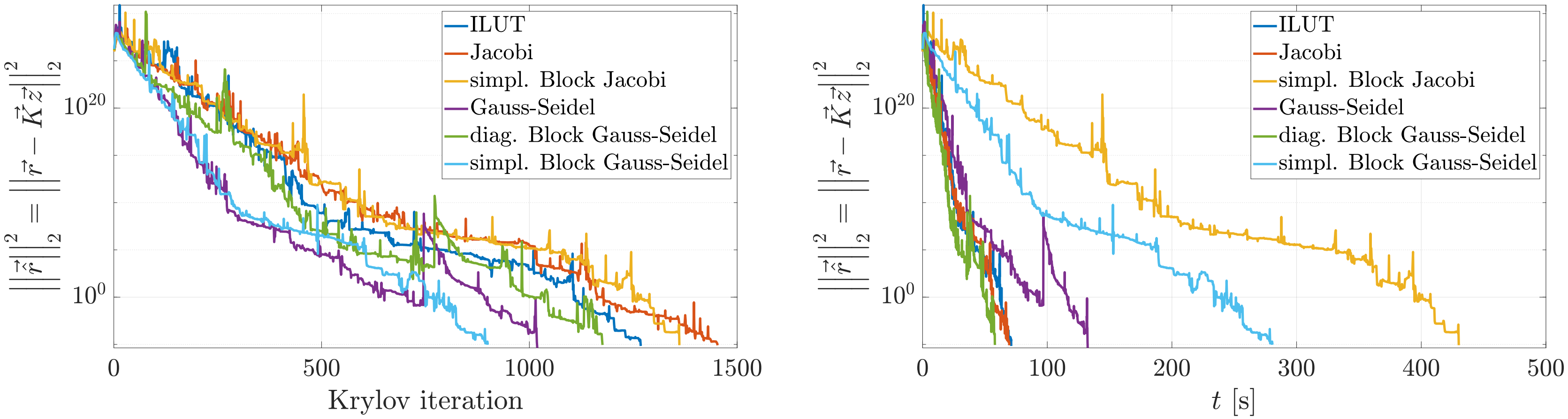

(c) Convergence versus iterations for high carrier density.

(d) Convergence versus time for high carrier density.

Figure 6.6: Convergence behavior of the BiCGSTAB solver with different preconditioners.

6.2.4 Inexact Newton-Raphson

If the linearized Newton-equations (6.11) are solved using iterative Krylov-subspace methods one possibility to speed-up the solution of the nonlinear equations is to use so-called *Inexact Newton* or *Newton-Krylov* methods. The idea is to avoid oversolving the linearized equations, i.e. solve them iteratively to a very high accuracy if the Newton step is still far from the solution of the nonlinear equations. In practice this means that the threshold for the Krylov-subspace method is adapted over the Newton iteration where even though the number of iterations increases the total computation time decreases as for every Newton iteration less Krylov iterations are necessary. One allows for a certain error $\boldsymbol{r}_k$

$$\boldsymbol{J}^{(k)}\boldsymbol{\Delta p}^{(k)} = -\boldsymbol{f}(\boldsymbol{p}^{(k)}) + \boldsymbol{r}^{(k)}, \quad \text{such that } \frac{||\boldsymbol{r}^{(k)}||}{||\boldsymbol{f}(\boldsymbol{p}^{(k)})||} \leq \eta^{(k)} \tag{6.23}$$

One key point to consider with such a method is convergence of the Newton iteration. Mathematically it can be shown that the convergence of the superordinate Newton iteration depends on the evolution of the series $\{\eta^{(k)}\}$ (assuming it converges at all) [85]

1. Linear convergence for $0 < \eta < 1,\ \eta \neq f(k)$
2. Superlinear convergence for $\eta^{(k)} \to 0 \,\text{for}\, k \to \infty$
3. Quadratic convergence for $\eta^{(k)} = c||\boldsymbol{f}(\boldsymbol{p}^{(k)})||,\ 0 < c$

Also, some other conditions apply, the Jacobian needs to be Hölder continuous with the corresponding exponent of convergence at the final solution $\boldsymbol{p}^*$. In order to achieve quadratic convergence with increasing accuracy towards the end, the threshold was set to be

$$\eta_k = \min\{\left|\left|\boldsymbol{f}(\boldsymbol{p}^{(k)})\right|\right|_2, \eta_{\text{ref}}\} \tag{6.24}$$

To check the benefit of this approach different grid sizes were simulated again once with high and once with lower charge carrier densities. The results are very different depending on the carrier densities and the grid sizes, as can be seen in fig. 6.7 and 6.8 (lines with same line style correspond to one initial value of η_{ref} and belong together, the solid line corresponds to the exact case). For low carrier densities where the initial guess $\boldsymbol{p} = \boldsymbol{0}$ was closer to the final solution the inexact method behaved well and converged almost identically to the exact method after four iterations for constant $\eta_{\text{ref}} = 10^{-3}$. However, in these cases the computational benefit of the inexact method in absolute terms was not that large of course as well.

In the case of high carrier densities, the result was quite different. For the smaller grid size at first $\eta_{\text{ref}} = 0.5$ was chosen as suggested in [85], however, no convergence could be achieved and $\left|\left|\boldsymbol{f}(\boldsymbol{p}^{(k)})\right|\right|_2$ started to oscillate around 10^{10}. Convergence was again achieved by lowering the reference threshold to 10^{-2}. For the larger grid this was also not sufficient anymore and the residual started to oscillate again. As an additional measure the reference threshold was reduced dynamically ($\eta_{\text{ref}} \to \eta_{\text{ref}}/10$) as soon as an increase in the residual was detected. In fig. 6.8b it is clearly visible that this dynamic adjustment does not yield any benefit, as soon as the iteration stops converging it seems to be trapped in a region of the solution space from where it cannot escape anymore, even if the linearized equations are solved to high accuracy. As a conclusion, using these inexact Newton methods without any additional precautions can lead to serious convergence problems, especially when the initial guess is far from the solution (as given with high carrier densities). It seems as if the Newton solver navigates itself into a region in solution space from which it cannot escape anymore due to the inexact steps in the beginning. Convergence could be enhanced by *globalizing* these inexact Newton methods, as described e.g. in [86], such as by Backtracking and Dogleg methods. The additional computation cost for such methods seems not really justified though, as the exact methods also provide good results already.

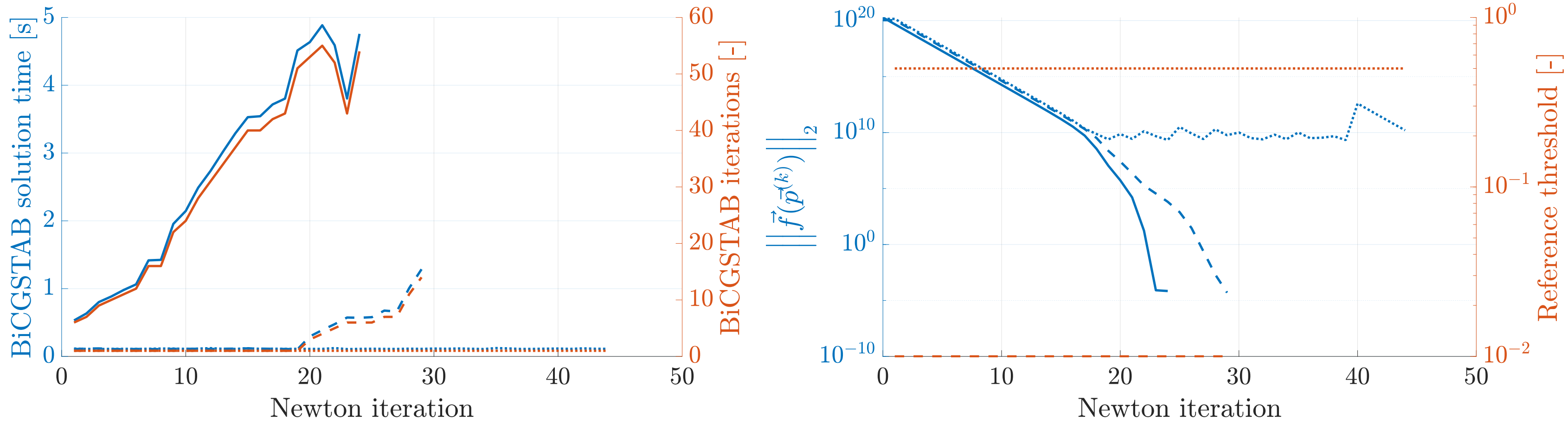

(a) Solution time and iterations for BiCGSTAB.

(b) Relative function norm and η_{ref} set in BiCGSTAB.

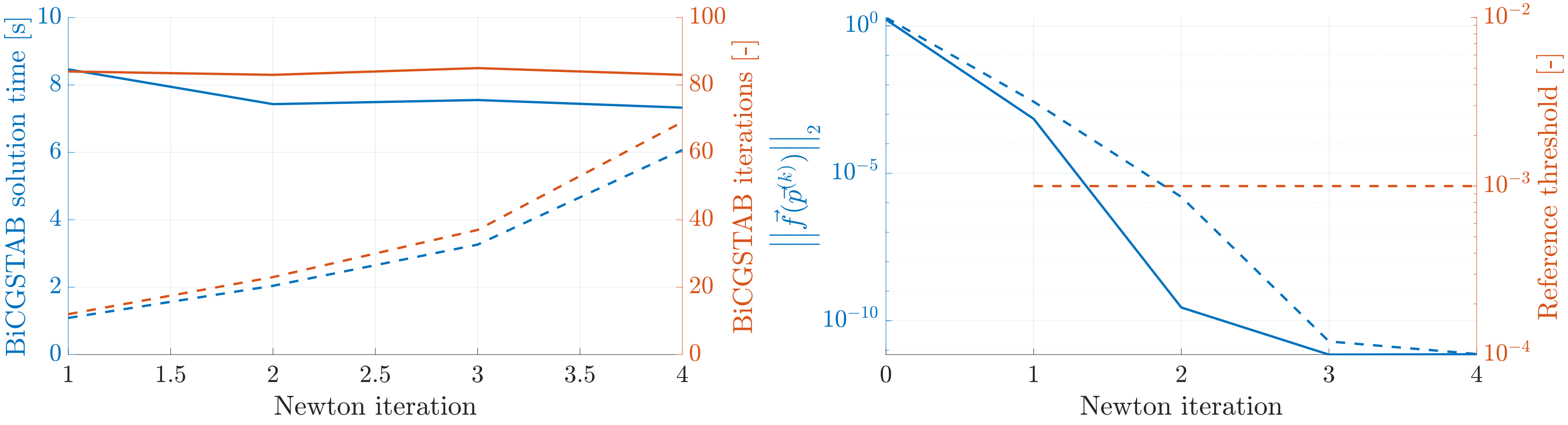

(c) Solution time and iterations for BiCGSTAB.

(d) Relative function norm and η_{ref} set in BiCGSTAB.

Figure 6.7: Inexact Newton convergence using a 120x15x15 grid ((a) and (b) high, (c) and (d) low carrier density).

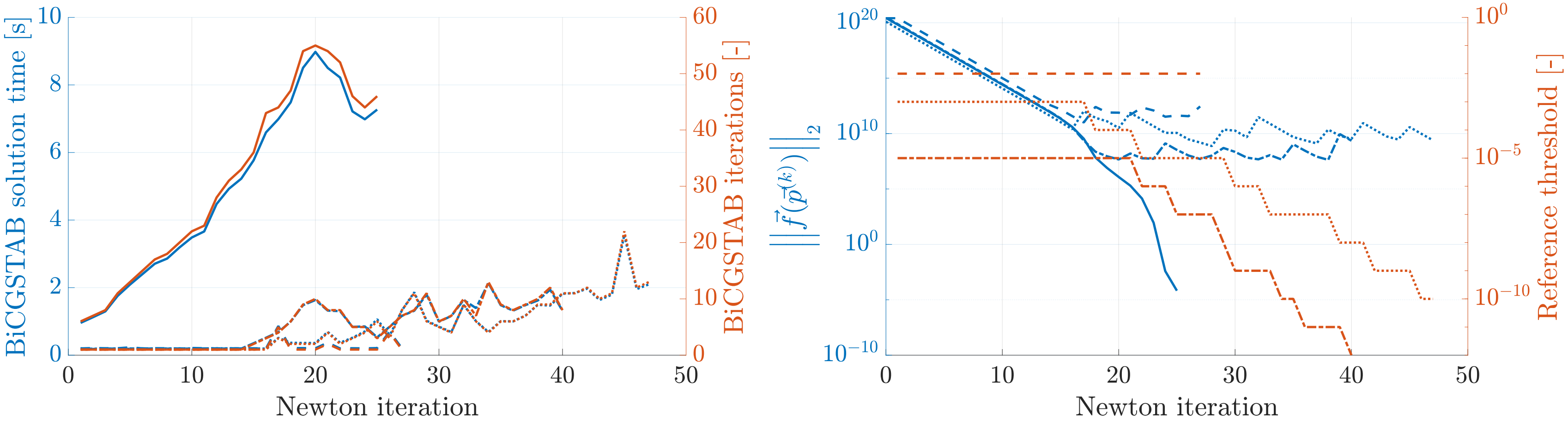

(a) Solution time and iterations for BiCGSTAB.

(b) Relative function norm and η_{ref} set in BiCGSTAB.

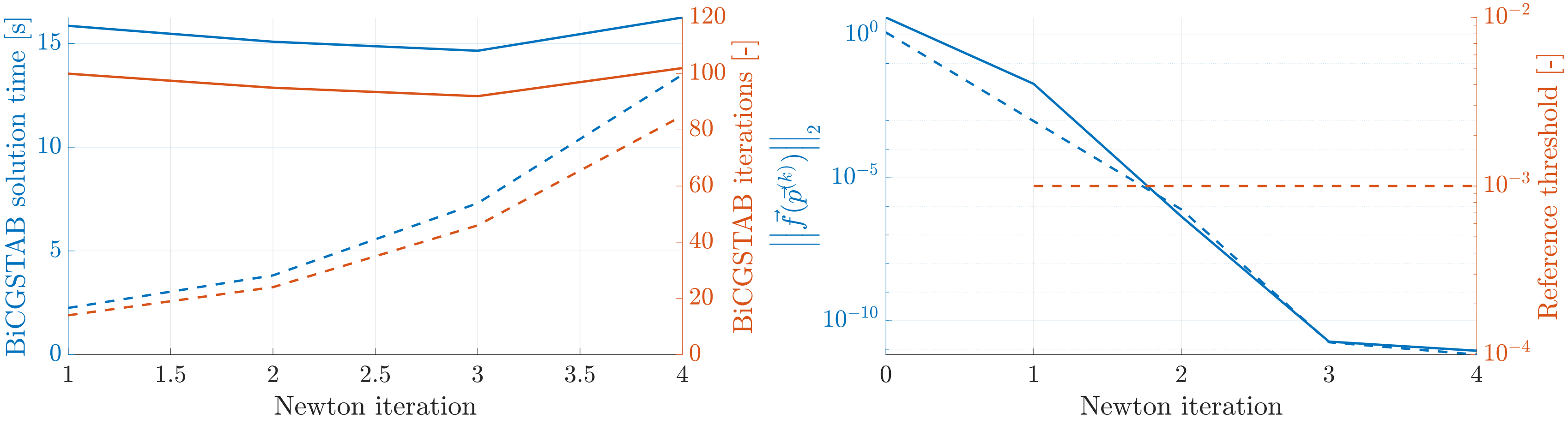

(c) Solution time and iterations for BiCGSTAB.

(d) Relative function norm and η_{ref} set in BiCGSTAB.

Figure 6.8: Inexact Newton convergence using a 120x20x20 grid ((a) and (b) high, (c) and (d) low carrier density).

6.2.5 Balance equations

Under steady-state conditions the total generation of excitons must match the total decay which can be used to check the accuracy of the computed occupation numbers in the whole grid. Mathematically such balance equations can be achieved by summing over all equations in the system. In the general case this yields the following expressions, depending on the exciton type considered (only singlets, triplets or both). For singlets only we have

$$\begin{aligned}
& \sum_i^N \left(\frac{1}{\tau^{\mathrm{s}}_{\mathrm{r},i}} + \frac{1}{\tau^{\mathrm{s}}_{\mathrm{nr},i}}\right) \exp\left(\frac{E^{\mathrm{s}}_{\mathrm{b},i} - E_{\mathrm{g},i}}{k_B T}\right) \\
& + \sum_i^N \frac{p^{\mathrm{t}}_i}{\tau_{\mathrm{ISC},i}} \exp\left(\frac{E^{\mathrm{s}}_{\mathrm{b},i} - E^{\mathrm{t}}_{\mathrm{b},i}}{k_B T}\right) \\
& + \sum_i^N \frac{\left(p^{\mathrm{t}}_i\right)^2}{2\tau_{\mathrm{TTA},i}} + \sum_i^N g_{\mathrm{Rec},i} \frac{p^{\mathrm{e}}_i p^{\mathrm{h}}_i}{\tau_i} + \sum_i^N g_{\mathrm{Opt},i} G_i \\
= & \sum_i^N \left(\frac{1}{\tau^{\mathrm{s}}_{\mathrm{r},i}} + \frac{1}{\tau^{\mathrm{s}}_{\mathrm{nr},i}}\right) p^{\mathrm{s}}_i + \sum_i^N \frac{p^{\mathrm{s}}_i}{\tau_{\mathrm{ISC},i}} \\
& + \sum_i^N g_{\mathrm{Rec},i} \frac{p^{\mathrm{s}}_i}{\tau_i} \exp\left(-\frac{E^{\mathrm{s}}_{\mathrm{b},i}}{k_B T}\right) + \sum_i^N \frac{p^{\mathrm{s}}_i \left(p^{\mathrm{e}}_i + p^{\mathrm{h}}_i\right)}{\tau_{\mathrm{SPQ},i}}
\end{aligned} \tag{6.25}$$

and for triplets only

$$\begin{aligned}
& \sum_i^N \left(\frac{1}{\tau^{\mathrm{t}}_{\mathrm{r},i}} + \frac{1}{\tau^{\mathrm{t}}_{\mathrm{nr},i}}\right) \exp\left(\frac{E^{\mathrm{t}}_{\mathrm{b},i} - E_{\mathrm{g},i}}{k_B T}\right) \\
& + \sum_i^N \frac{p^{\mathrm{s}}_i}{\tau_{\mathrm{ISC},i}} \\
& + \sum_i^N (1 - g_{\mathrm{Rec},i}) \frac{p^{\mathrm{e}}_i p^{\mathrm{h}}_i}{\tau_i} + \sum_i^N (1 - g_{\mathrm{Opt},i}) G_i \\
= & \sum_i^N \left(\frac{1}{\tau^{\mathrm{t}}_{\mathrm{r},i}} + \frac{1}{\tau^{\mathrm{t}}_{\mathrm{nr},i}}\right) p^{\mathrm{t}}_i + \sum_i^N \frac{p^{\mathrm{t}}_i}{\tau_{\mathrm{ISC},i}} \exp\left(\frac{E^{\mathrm{s}}_{\mathrm{b},i} - E^{\mathrm{t}}_{\mathrm{b},i}}{k_B T}\right) \\
& + \sum_i^N \frac{\left(p^{\mathrm{t}}_i\right)^2}{\tau_{\mathrm{TTA},i}} \\
& + \sum_i^N (1 - g_{\mathrm{Rec},i}) \frac{p^{\mathrm{t}}_i}{\tau_i} \exp\left(-\frac{E^{\mathrm{t}}_{\mathrm{b},i}}{k_B T}\right) + \sum_i^N \frac{p^{\mathrm{t}}_i \left(p^{\mathrm{e}}_i + p^{\mathrm{h}}_i\right)}{\tau_{\mathrm{TPQ},i}}
\end{aligned} \tag{6.26}$$

The expression combining both species for the total number of excitons reads

$$
\begin{aligned}
&\sum_i^N \left(\frac{1}{\tau^{\mathrm{s}}_{\mathrm{r},i}} + \frac{1}{\tau^{\mathrm{s}}_{\mathrm{nr},i}}\right) \exp\left(\frac{E^{\mathrm{s}}_{\mathrm{b},i} - E_{\mathrm{g},i}}{k_B T}\right) \\
&+\sum_i^N \left(\frac{1}{\tau^{\mathrm{t}}_{\mathrm{r},i}} + \frac{1}{\tau^{\mathrm{t}}_{\mathrm{nr},i}}\right) \exp\left(\frac{E^{\mathrm{t}}_{\mathrm{b},i} - E_{\mathrm{g},i}}{k_B T}\right) \\
&+\sum_i^N \frac{p^{\mathrm{e}}_i p^{\mathrm{h}}_i}{\tau_i} + \sum_i^N G_i \\
= \quad &\sum_i^N \left(\frac{1}{\tau^{\mathrm{s}}_{\mathrm{r},i}} + \frac{1}{\tau^{\mathrm{s}}_{\mathrm{nr},i}}\right) p^{\mathrm{s}}_i + \sum_i^N \left(\frac{1}{\tau^{\mathrm{t}}_{\mathrm{r},i}} + \frac{1}{\tau^{\mathrm{t}}_{\mathrm{nr},i}}\right) p^{\mathrm{t}}_i \\
&+\sum_i^N g_{\mathrm{Rec},i} \frac{p^{\mathrm{s}}_i}{\tau} \exp\left(-\frac{E^{\mathrm{s}}_{\mathrm{b},i}}{k_B T}\right) + \sum_i^N (1 - g_{\mathrm{Rec},i}) \frac{p^{\mathrm{t}}_i}{\tau} \exp\left(-\frac{E^{\mathrm{t}}_{\mathrm{b},i}}{k_B T}\right) \\
&+\sum_i^N \left[\left(p^{\mathrm{e}}_i + p^{\mathrm{h}}_i\right)\left(\frac{p^{\mathrm{s}}_i}{\tau_{\mathrm{SPQ},i}} + \frac{p^{\mathrm{t}}_i}{\tau_{\mathrm{TPQ},i}}\right)\right] + \sum_i^N \frac{\left(p^{\mathrm{t}}_i\right)^2}{2\tau_{\mathrm{TTA},i}}
\end{aligned} \tag{6.27}
$$

A more detailed derivation can be found in the appendix A.2.

6.3 Transient solution

In many cases not only the final steady-state distribution is of interest, instead, the goal of the simulation is to obtain time dependent evolutions of the occupation numbers, such as for turn-on and turn-off behavior. To achieve this, the differential equations need to be integrated numerically in time which will be the main focus of this section.

6.3.1 Stability

The mathematical problem resulting from the Master equations (4.7) and (4.8) is a *non-autonomous initial-value problem* (IVP) of the form

$$
\begin{aligned}
\frac{\mathrm{d}\boldsymbol{p}}{\mathrm{d}t} &= \boldsymbol{f}(t, \boldsymbol{p}) \\
\boldsymbol{p}(t = 0) &= \boldsymbol{p_0}
\end{aligned} \tag{6.28}
$$

One important factor when numerically solving such IVPs is the behavior of the solution obtained by numerical schemes. One important criterion for the existence of such a solution is given by Picard-Lindelöf (taken from [77])

Theorem. *Let $D \subseteq \mathbb{R} \times \mathbb{R}^n$ be an open set, and let $\boldsymbol{f} : D \to \mathbb{R}^n$ be continuous in the first variable and uniform Lipschitz in its second, i.e. for $(t, \boldsymbol{p}) \in D$, $\boldsymbol{f}(t, \boldsymbol{p})$ is continuous as a function of t, and there exists a constant γ such that for any $(t, \boldsymbol{p_1})$ and $(t, \boldsymbol{p_2})$ in D we have*

$$
|\boldsymbol{f}(t, \boldsymbol{p_1}) - \boldsymbol{f}(t, \boldsymbol{p_2})| \leq \gamma \, |\boldsymbol{p_1} - \boldsymbol{p_2}|
$$

Then, for any $(t_0, \boldsymbol{p_0}) \in D$*, there exists an interval* $I := (t^-, t^+)$ *containing* t_0 *and a unique solution* $\boldsymbol{p} \in C^1(I)$ *of the initial-value problem*

$$\begin{aligned} \frac{\partial \boldsymbol{p}}{\partial t}(t) &= \boldsymbol{f}(t, \boldsymbol{p}) \\ \boldsymbol{p}(t_0) &= \boldsymbol{p_0} \end{aligned}$$

Additionally, even if a solution exists, two crucial properties of the numerical scheme are *stability* and *convergence*. The latter simply states that the numerical solution should approach the exact analytical solution representing the system of ordinary differential equations for stepsizes approaching zero $h \to 0$. The former property (stability) states that the error of the numerical solution relative to the exact one needs to stay bounded, even though time tends towards infinity $t \to \infty$. This property is also closely related to *stiffness* where so-called stiff equations are very difficult to integrate numerically.

This property of stiffness can be shown well on the simple linear ODE given by

$$\frac{\mathrm{d}y(t)}{\mathrm{d}t} = \lambda y, \implies y(t) = y_0 \exp\left(-\lambda t\right), \qquad \lambda \in \mathbb{C} \tag{6.29}$$

which is commonly called the *Dahlquist test equation.* The reason why such a simple linear system is studied is that the system (6.28) can be linearized (therefore this is used to determine *linear stability*) resulting in the form

$$\dot{\boldsymbol{p}} = \boldsymbol{J}\boldsymbol{p} + \boldsymbol{g}(t) \tag{6.30}$$

with the general solution

$$\boldsymbol{p}(t) = \sum_{n=1}^{m} \kappa_n \exp\left(\lambda_n t\right) \boldsymbol{c}_n + \boldsymbol{\psi}(t) \tag{6.31}$$

where λ_n and $\boldsymbol{c}_n$ are the eigenvalues and eigenvectors of $\boldsymbol{J}$. Assuming

$$\Re(\lambda_n) < 0 \quad \forall n$$

therefore the terms in the sum are decaying modes of the solution and $\boldsymbol{p}(t)$ approaches the steady-state solution $\boldsymbol{\psi}(t)$. If it is now desired to numerically solve the ODE all the way to steady-state all the decaying transient modes need to vanish, where the slowest mode with $\Re(\underline{\lambda})$ determines this time interval. On the other hand, if there are much faster modes with $\Re(\overline{\lambda})$ corresponding to the fastest, these will determine the resulting temporal discretization which is needed. Therefore, if the *stiffness ratio* [87]

$$\frac{\Re(\overline{\lambda})}{\Re(\underline{\lambda})} \tag{6.32}$$

is very large in magnitude, then a very small stepsize is needed for a long integration time leading to an excessive number of integration steps. This is the reason why the ability of a numerical scheme to integrate (6.29) is of interest. One example scheme applied to (6.29) for demonstration purposes is the *forward Euler scheme* (see also section 6.3.2) which results in (assuming $\lambda \in \mathbb{R}$ for simplicity)

$$y(t+h) = (1+\lambda h)y(t) \implies y(t+nh) = (1+\lambda h)^n y(t) \tag{6.33}$$

It is clear that for $\lambda < 0$ the exact solution tends to zero for $t \to \infty$. On the other hand, the iterative scheme in (6.33) only tends to zero if

$$|1+\lambda h| < 1 \implies h < \frac{2}{|\lambda|}$$

this motivates the definition of the *stability function* $R(z) = R(h\lambda)$ $(z \in \mathbb{C})$, which for the forward Euler scheme is $R(z) = 1 + z$, and the *stability region* S which defines the region on the complex plane where $|R(z)| < 1$. Using this some important properties for numerical integration schemes can be defined [79]

Definition. A single-step numerical integration scheme with stability function $R(z)$ and stability region S is called *A-stable* if $\{z \in \mathbb{C} | \Re(z) < 0\} \subseteq S$. Furthermore, the scheme is called *L-stable* if it is A-stable and fulfills $\lim\limits_{\Re(z) \to -\infty} |R(z)| = 0$.

Therefore, an A-stable method integrating (6.29) will tend to zero for $t \to \infty$ for any $h > 0$. An L-stable method will furthermore also strongly dampen very rapidly decaying modes where $|\Re(\lambda)|$ is very large. It can be shown that for a general Runge-Kutta method with coefficients $\boldsymbol{A}$ and $\boldsymbol{b}$ as described later the stability function is given by [81]

$$R(z) = \frac{\det(\boldsymbol{I} - z\boldsymbol{A} + z\boldsymbol{e} \otimes \boldsymbol{b}^T)}{\det(\boldsymbol{I} - z\boldsymbol{A}} \tag{6.34}$$

Even though the concepts discussed here only concerned linear stability, a numerical method featuring e.g. L-stability will mostly also perform well applied to nonlinear equations. For details on nonlinear stability considerations see [88, 87, 89] as such a treatment would be out of scope for this work.

6.3.2 Integration methods

In this work only single-step *Runge-Kutta* (RK) methods were considered as there is a wide range of possible schemes readily available. In the following first part a short general introduction in these RK methods is given followed by some specific methods which were implemented in the solver.

This type of methods was first introduced by Kutta [90] where the general approach is given by

$$\boldsymbol{k_s} = \boldsymbol{f}(t_n + c_s h, \boldsymbol{p_n} + h \sum_{j=1}^{m} a_{sj} \boldsymbol{k_j}) \tag{6.35}$$

$$\boldsymbol{p_{n+1}} = \boldsymbol{p_n} + h \sum_{s} b_s \boldsymbol{k_s} \tag{6.36}$$

The coefficients a_{sj}, b_s and c_s are defined by the specific RK method and generally presented as a *Butcher tableau* [89]

$$\begin{array}{c|c} \boldsymbol{c} & \boldsymbol{A} \\ \hline & \boldsymbol{b}^T \\ & \hat{\boldsymbol{b}}^T \end{array} \tag{6.37}$$

The idea of these methods is to calculate a series of slopes $\{\boldsymbol{k_s}\}$ from which then the next function value $\boldsymbol{p_{n+1}}$ is calculated as a weighted linear combination of the slopes where the weights are chosen such that the leading errors cancel out each other. Sometimes also a second set of weights $\hat{\boldsymbol{b}}$ is given with different order than the original weights for stepsize control purposes. The *order* of a method is defined as follows [91]

Definition. Let $\boldsymbol{p_i}$ be the estimated solution at timestep t_i. Then a RK method is said to have *order* p if the difference between estimated and true solution at this timestep satisfies

$$||\boldsymbol{p_i} - \boldsymbol{p}(t_0 + ih)|| = \mathcal{O}\left(h^{p+1}\right)$$

This is referred to as the *local error* if one assumes that the step $\boldsymbol{p_{i-1}}$ was exact, i.e. the error for a single step. On the other hand, the *global error* usually scales as $\mathcal{O}\left(h^p\right)$ as with smaller stepsizes the local error decreases, but at the same time the steps necessary to reach a certain integration time increases as $\mathcal{O}\left(h\right)$. Such methods then of course possess the convergence property, as $||\boldsymbol{p_i} - \boldsymbol{p}(t_0 + ih)|| \to 0$ for $h \to 0$.

If a set $\hat{\boldsymbol{b}}$ is given additionally with different order, then this set can be used to achieve stepsize control cheaply as the same set of slopes can be used for both and virtually no additional work needs to be done. The error of both methods follows from

$$\begin{aligned} \boldsymbol{p_i} &= \boldsymbol{p}(t_{i-1} + h) + \boldsymbol{C}h^{p+1} + \mathcal{O}\left(h^{p+2}\right) \\ \hat{\boldsymbol{p}}_{\boldsymbol{i}} &= \boldsymbol{p}(t_{i-1} + h) + \hat{\boldsymbol{C}}h^{\hat{p}+1} + \mathcal{O}\left(h^{\hat{p}+2}\right) \end{aligned} \tag{6.38}$$

and therefore (assuming $p > \hat{p}$)

$$\boldsymbol{p_i} - \hat{\boldsymbol{p}}_{\boldsymbol{i}} = \hat{\boldsymbol{C}}h^{\hat{p}+1} + \mathcal{O}\left(h^{\hat{p}+2}\right) \tag{6.39}$$

From this we can estimate the error and choose a stepsize h^* which fulfills the specified tolerance tol

$$||\hat{\boldsymbol{p}}_{\boldsymbol{i}} - \boldsymbol{p}(t_{i-1} + h)|| \simeq \left|\left|\hat{\boldsymbol{C}}\right|\right| (h^*)^{\hat{p}+1} \simeq \underbrace{||\boldsymbol{p_i} - \hat{\boldsymbol{p}}_{\boldsymbol{i}}||}_{e} \left(\frac{h^*}{h}\right)^{\hat{p}+1} \implies h^* = h\beta_s \left(\frac{\mathrm{tol}}{e}\right)^{\frac{1}{\hat{p}+1}} \tag{6.40}$$

where $\beta_s \approx 0.9$ is a safety factor. In the code this is implemented slightly different, namely as

$$\boldsymbol{\delta} = \frac{\boldsymbol{p} - \hat{\boldsymbol{p}}}{\beta\,|p| + \alpha} \implies h^* = h\beta_s \left(||\boldsymbol{\delta}||_\infty\right)^{-\frac{1}{\hat{p}+1}} \tag{6.41}$$

where again β and α are relative and absolute tolerances. This is a very basic stepsize controller and much more sophisticated ones can be employed with the general form [81]

$$h^* = \beta_s h \left(||\boldsymbol{\delta}||\right)^{-a} \left(||\delta||^{\dagger}\right)^{b} \left(||\delta||^{\dagger\dagger}\right)^{-c} \left(\frac{h}{h^{\dagger}}\right)^{\mathfrak{a}} \left(\frac{h^{\dagger}}{h^{\dagger\dagger}}\right)^{\mathfrak{b}} \tag{6.42}$$

Such controllers also take errors and timesteps of previous steps (indicated by †) into account. These will not be considered further though. Especially for the (E)SDIRK methods described later some further strategies exist such as iteration control (control of the stepsize also taking into account the convergence of the iterative solution at each step) as well as sophisticated stage-value predictors providing initial guesses for the iteration.

Explicit methods

Explicit RK methods are characterized by having $a_{sj} = 0$ for $j \geq s$. Therefore, in (6.35), the slopes $\{\boldsymbol{k_s}\}$ can be calculated sequentially which is computationally quite cheap. The price to pay for that is the worse stability properties of these methods where an example was illustrated in section 6.3.1, in fact from (6.34) it can even be shown that explicit RK methods can *never be A-stable* [92]. In the code a variety of explicit methods are implemented, listed in tab. 6.1. The stability problems of these methods become evident in the following example.

Table 6.1: Implemented explicit Runge Kutta schemes with the corresponding orders. For the respective tableaus see A.4.1.

	p	$\hat{p}$	Source
Euler	1	–	[91]
Heun (trapezoidal rule)	2	–	[91]
RK32	3	–	[91]
Classic Runge-Kutta	4	–	[91]
Heun-Euler	2	1	[91]
Cash-Karp	5	4	[91]

The same steady-state charge carrier and potential distribution as in section 7.2 was used as a static input for the ODE, with initial condition $\boldsymbol{p}(0) = \boldsymbol{0}$. The exciton occupation numbers should therefore increase and slowly approach the steady-state distribution as given in the example. The triplet occupation numbers averaged over the lateral dimensions are shown in fig. 6.9 where the first eight timesteps are shown with an absolute tolerance $\alpha = 10^{-6}$ and initial timestep $h_0 = 0.1\,\mathrm{ps}$. In fig. 6.10 the resulting stepsizes chosen by the stepsize controller are shown for different tolerances (the two lines corresponding to $\mathrm{tol} = \alpha = 10^{-6}$ differ in initial stepsize h_0). After an initial overshoot all tolerances settle their stepsizes to certain constant value which is independent of the tolerance chosen. This is a typical behavior when the stepsize is not limited by *accuracy*, instead it is limited by *stability* (stiff ODE). This can also be seen when comparing the timesteps with the obtained solution where the onset of instability (negative densities in an oscillatory spatial manner) at step four coincides with the overshoot of h. After leaving the stable region errors increase depending on how far the step into said region was (larger for higher tolerances), therefore the increase

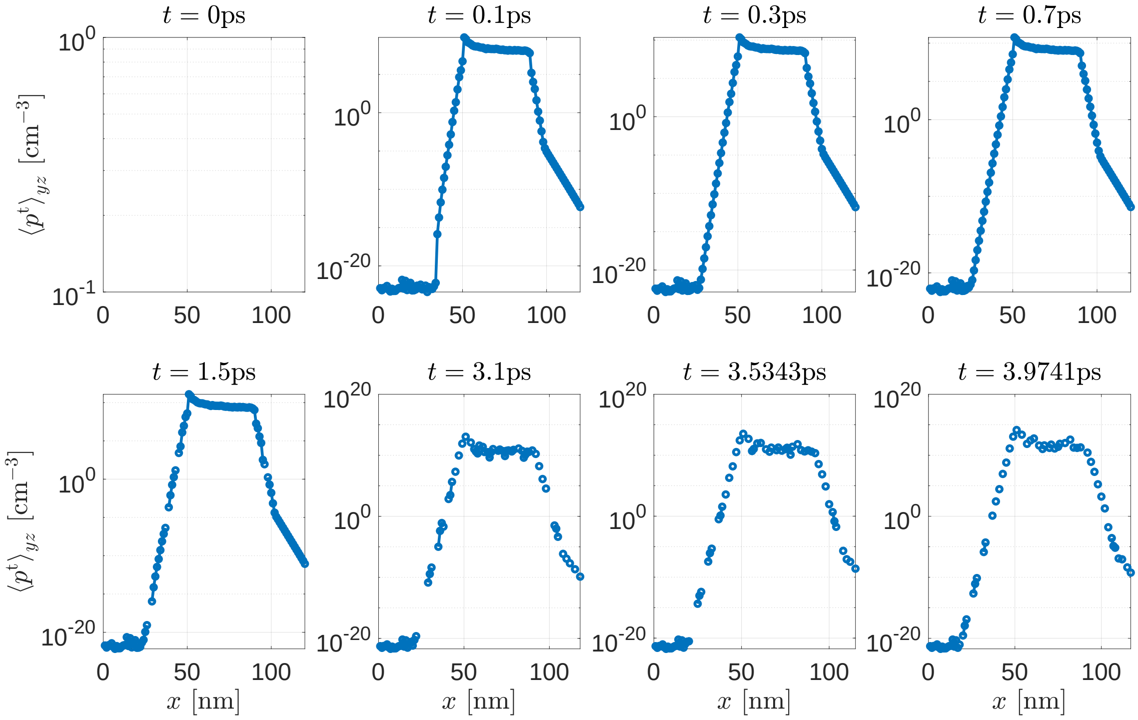

Figure 6.9: Unstable solution with explicit RK solver Cash-Karp.

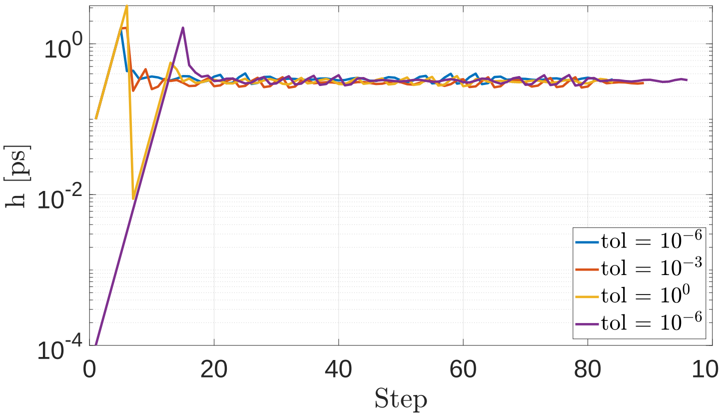

Figure 6.10: Evolution of stepsize for explicit RK solver Cash-Karp.

in error cancels the larger tolerance, leading to a stepsize equal for all tolerances. To avoid instabilities excessively small stepsizes would need to be chosen.

(Explicit) Singly-diagonal implicit Runge-Kutta methods

In order to overcome the stability constraints induced by the explicit methods the *implicit* Runge-Kutta methods can be used. The main difference to the explicit methods is that the constraint $a_{sj} = 0$ for $j \geq s$ is not fulfilled anymore. Therefore (6.35) cannot be computed sequentially, instead, a (generally nonlinear) system of equations needs to be solved at each step, strongly increasing the computational cost. One way to levitate this cost is to use *diagonal implicit RK* (DIRK) methods where $a_{sj} = 0$ for $j > s$, i.e. $\boldsymbol{A}$ is a lower-triangular matrix. The equations (6.35) can then be solved one after the other where instead of solving one big ($(mN) \times (mN)$, where N the DOF of $\boldsymbol{f}$) system for all $\{\boldsymbol{k_s}\}$ at once the task reduces to solve m nonlinear equations of size $N \times N$. If also $a_{ss} = \tilde{a}\,\forall s$ the method is called *singly-diagonal implicit RK* or SDIRK. One additional type of methods are the *explicit singly-diagonal implicit RK* (ESDIRK) methods which are SDIRK methods with the additional property that $a_{11} = 0$, i.e. the first stage is explicit reducing the number of nonlinear systems that need to be solved.

Due to the large number of DOF in the case considered here only (E)SDIRK methods were implemented. A list of methods used here are given in tab. 6.2 and 6.3. For a general DIRK scheme (6.35) becomes

Table 6.2: Implemented SDIRK schemes with the corresponding orders and stability properties. For the respective tableaus see A.4.2.

	p	$\hat{p}$	Stability	Source
SDIRK-2a	2	1	L-stable	[81, 79, 93]
SDIRK4	4	3	L-stable	[88]
Implicit midpoint rule	2	1	A-stable	[81, 79]
Implicit Euler	1	–	L-stable	[81, 79]

Table 6.3: Implemented ESDIRK schemes with the corresponding orders and stability properties. For the respective tableaus see A.4.3.

	p	$\hat{p}$	Stability	Source
Implicit trapezoidal rule	2	1	A-stable	[81]
ESDIRK43	4	2	L-stable	[81]

$$\boldsymbol{k_s} = \boldsymbol{f}(t_n + c_s h, \underbrace{\boldsymbol{p_n} + h\sum_{j}^{s-1} a_{sj}\boldsymbol{k_j}}_{\boldsymbol{x_s}} + h a_{ss}\boldsymbol{k_s}) \tag{6.43}$$

where $\boldsymbol{x_s}$ can be calculated from the previously computed slopes. However, now the point where the slope needs to be computed is not known directly as it itself depends on the slope $\boldsymbol{k_s}$. This leads to the nonlinear system of equations with $\tilde{t} = t_0 + c_s h$

$$\tilde{\boldsymbol{p}}_{\boldsymbol{s}} = \boldsymbol{p_n} + \boldsymbol{x_s} + h a_{ss} \boldsymbol{f}(\tilde{t}, \tilde{\boldsymbol{p}}_{\boldsymbol{s}}) \implies \boldsymbol{p_n} + \boldsymbol{x_s} + h a_{ss} \boldsymbol{f}(\tilde{t}, \tilde{\boldsymbol{p}}_{\boldsymbol{s}}) - \tilde{\boldsymbol{p}}_{\boldsymbol{s}} = 0 \tag{6.44}$$

which needs to be solved by Newton iteration. This results in the following iterative Newton equation

$$\left(\boldsymbol{J}(\tilde{t}, \tilde{\boldsymbol{p}}_{\boldsymbol{s}}^{(k)}) - \frac{1}{h a_{ss}} \boldsymbol{I}\right) \boldsymbol{\Delta} \tilde{\boldsymbol{p}}_{\boldsymbol{s}}^{(k)} = \frac{1}{h a_{ss}} \left(\tilde{\boldsymbol{p}}_{\boldsymbol{s}}^{(k)} - \boldsymbol{p_n} - \boldsymbol{x_s}\right) - \boldsymbol{f}(\tilde{t}, \tilde{\boldsymbol{p}}_{\boldsymbol{s}}^{(k)}) \tag{6.45}$$

where $\boldsymbol{J}$ is again the Jacobian of $\boldsymbol{f}$, ${}^{\mathrm{d}\boldsymbol{f}}/_{\mathrm{d}\boldsymbol{p}}$, and $\boldsymbol{p_n} + \boldsymbol{x_s}$ can be used as initial guess. This iteration needs to be solved at every step multiple times yielding much more stable results in return. It is important to note however that additionally to the possibility of failure of the integration these methods can also fail by non-converging Newton iterations. Therefore, even though from stability considerations large timesteps could be chosen smaller ones may be needed for the Newton iteration to converge.

Rosenbrock-Wanner methods

This last point regarding possible convergence problems of DIRK methods can finally also be overcome by using *Rosenbrock-Wanner* (ROW) methods, sometimes also called semi-implicit RK methods. These methods are found in between explicit and implicit methods featuring cheaper computation times but still high stability. These methods start from SDIRK methods

$$\boldsymbol{k_s} = h \boldsymbol{f}(t_n + c_s h, \boldsymbol{p_n} + \sum_{j}^{s-1} a_{sj} \boldsymbol{k_j} + a_{ss} \boldsymbol{k_s}) \tag{6.46}$$

$$\boldsymbol{p_{n+1}} = \boldsymbol{p_n} + \sum_{s} b_s \boldsymbol{k_s} \tag{6.47}$$

Note the slight change in the equations where the position of h changed, i.e. $\boldsymbol{k_s}$ now represent intermediate solutions directly, following the notation in [88], the method itself is equivalent though. The idea of ROW methods is now to linearize (6.46) to avoid the Newton iteration yielding

$$\boldsymbol{k_s} = h \boldsymbol{f}(t_n + c_s h, \boldsymbol{p_n} + \sum_{j}^{s-1} a_{sj} \boldsymbol{k_j}) + \gamma_s h^2 \frac{\partial \boldsymbol{f}}{\partial t}(t_n, \boldsymbol{p_n}) + h \boldsymbol{J}(t_n, \boldsymbol{p_n}) \sum_{j=1}^{s} \gamma_{sj} \boldsymbol{k_j} \tag{6.48}$$

There are some points worth discussing. First, an additional parameter set $\boldsymbol{\gamma}$ is introduced where $\gamma_s = \sum_j^s \gamma_{sj}$ which are used to introduce additional linear combinations of already computed $\boldsymbol{k}$. Furthermore, note that the partial derivative w.r.t time only includes the time-dependent coefficients given by (assuming no time dependence in the Dexter rates)

$$\frac{\partial \boldsymbol{f}}{\partial t} = \frac{\mathrm{d}}{\mathrm{d}t}(\boldsymbol{b}_{\mathrm{Rec}}) + \frac{\mathrm{d}}{\mathrm{d}t}(\boldsymbol{b}_{\mathrm{Opt}}) - \frac{\mathrm{d}}{\mathrm{d}t}(\boldsymbol{D}_{\mathrm{PQ}}) \boldsymbol{p} \tag{6.49}$$

where

$$\boldsymbol{b}_{\text{Rec}} = \begin{bmatrix} \boldsymbol{b}^{\text{s}}_{\text{Rec}} \\ \boldsymbol{b}^{\text{t}}_{\text{Rec}} \end{bmatrix} \qquad \text{with} \begin{cases} \frac{\mathrm{d}}{\mathrm{d}t}(\boldsymbol{b}^{\text{s}}_{\text{Rec}})_i = \frac{g_{\text{Rec},i}}{\tau_i}\left(p^{\text{e}}_i \frac{\mathrm{d}p^{\text{h}}_i}{\mathrm{d}t} + p^{\text{h}}_i \frac{\mathrm{d}p^{\text{e}}_i}{\mathrm{d}t}\right) \\ \frac{\mathrm{d}}{\mathrm{d}t}(\boldsymbol{b}^{\text{t}}_{\text{Rec}})_i = \frac{1-g_{\text{Rec},i}}{\tau_i}\left(p^{\text{e}}_i \frac{\mathrm{d}p^{\text{h}}_i}{\mathrm{d}t} + p^{\text{h}}_i \frac{\mathrm{d}p^{\text{e}}_i}{\mathrm{d}t}\right) \end{cases}$$

$$\boldsymbol{b}_{\text{Opt}} = \begin{bmatrix} \boldsymbol{b}^{\text{s}}_{\text{Opt}} \\ \boldsymbol{b}^{\text{t}}_{\text{Opt}} \end{bmatrix} \qquad \text{with} \begin{cases} \frac{\mathrm{d}}{\mathrm{d}t}(\boldsymbol{b}^{\text{s}}_{\text{Opt}})_i = g_{\text{Opt},i} \frac{\mathrm{d}G_{\text{Opt},i}}{\mathrm{d}t} \\ \frac{\mathrm{d}}{\mathrm{d}t}(\boldsymbol{b}^{\text{t}}_{\text{Opt}})_i = (1 - g_{\text{Opt},i}) \frac{\mathrm{d}G_{\text{Opt},i}}{\mathrm{d}t} \end{cases}$$

$$\boldsymbol{D}_{\text{PQ}} = \begin{bmatrix} \boldsymbol{D}_{\text{SPQ}} & \boldsymbol{0} \\ \boldsymbol{0} & \boldsymbol{D}_{\text{TPQ}} \end{bmatrix} \qquad \text{with} \begin{cases} \frac{\mathrm{d}}{\mathrm{d}t}(\boldsymbol{D}_{\text{SPQ}})_i = \frac{1}{\tau_{\text{SPQ},i}}\left(\frac{\mathrm{d}p^{\text{e}}_i}{\mathrm{d}t} + \frac{\mathrm{d}p^{\text{h}}_i}{\mathrm{d}t}\right) \\ \frac{\mathrm{d}}{\mathrm{d}t}(\boldsymbol{D}_{\text{TPQ}})_i = \frac{1}{\tau_{\text{TPQ},i}}\left(\frac{\mathrm{d}p^{\text{e}}_i}{\mathrm{d}t} + \frac{\mathrm{d}p^{\text{h}}_i}{\mathrm{d}t}\right) \end{cases}$$

Also note that the Jacobian is evaluated always at the last timestep $(t_n, \boldsymbol{p_n})$ and is not changed over the stages. By using such methods, only a linear system of equations needs to solved, therefore avoiding the possibility of non-converging Newton iterations as well as speeding up the computation compared to DIRK methods. There are two methods currently implemented, see tab. 6.4. Something similar can be done with any DIRK method by simply linearizing in $\boldsymbol{p_n}$ [77] which transforms (6.35) into (now again using the old form where $\{\boldsymbol{k_s}\}$ represent slopes)

Table 6.4: Implemented ROW schemes with the corresponding orders and stability properties. For the respective tableaus see A.4.4.

	p	$\hat{p}$	Stability	Source
GRK4A	4	3	A-stable	[94]
GRK4T	4	3	A(89.3°)-stable	[94]

$$\left(\boldsymbol{J}(t_n + c_s h, \boldsymbol{p_{s-1}}) - \frac{1}{h a_{ss}}\boldsymbol{I}\right)\boldsymbol{k_s} = \frac{1}{h a_{ss}}\boldsymbol{f}(t_n + c_s h, \boldsymbol{p_{s-1}}) \tag{6.50}$$

where

$$\boldsymbol{p_{s-1}} = \boldsymbol{p_n} + h\sum_{j=1}^{s-1} a_{sj}\boldsymbol{k_j}$$

Here the Jacobian is updated for every stage. Note, however, that the coefficients derived for the original nonlinear methods are not guaranteed to yield the same stability and accuracy when using these linearized versions (see e.g. fig. 5.7c and 5.7d)!

Chapter 7

Results and discussion

Finally, after discussing the basics and mathematical model, the implementation in the code and the various numerical methods used to solve the Master equations for the exciton occupation numbers some application examples are presented in this chapter. In the first section a validation of the 1D Master equation model in steady-state is shown where the computed figure of merit, the luminescence, is compared to literature data. Following a simulation result for the 3D steady-state of an OLED device is presented and analyzed. Finally, some application for the transient methods shown previously is also discussed.

7.1 1D steady-state

The first results were created using the 1D version of the code implementation, which works basically the same as the 3D version except that on the lateral dimensions a no-flow BC instead of periodic conditions is applied and setting both $m_y = m_z = 1$, i.e. the grid is simply a 1D chain of molecules. In order to check for the validity of such a model, a similar approach in literature was analyzed and used as reference.

In the paper by Wu et al. [70] the photoluminescence (PL) of the top Alq$_3$ layer in the structure depicted in fig. 7.1 was measured and subsequently modeled. Of interest was especially the influence of long-range Förster coupling of the excited Alq$_3$ molecules to the quenching DCM molecules with the final goal to have an estimate for the Förster radius R_0^{F}. To achieve this, the Alq$_3$ layer was pumped using a laser which led to exciton formation inside undergoing possible energy-quenching by the DCM layer through Förster transfer where they would be lost and not contributing anymore to the PL of Alq$_3$. The idea was that with variable thickness of the Alq$_3$ layer the PL starts very low due to the proximity of the excited molecules to the quenching DCM until a critical distance (thickness) is reached (higher than the Förster radius) from where on the PL of Alq$_3$ would start to become visible. In order to extract the parameters from the experimental data they employed a continuity model for exciton migration as follows:

$$\frac{1}{D}\frac{\partial N}{\partial t} = \frac{\partial^2 N(x)}{\partial x^2} - \left(1 + \frac{R_0^4}{x^4}\right)\frac{N(x)}{L_D^2} + \frac{G_0\tau_0}{L_D^2} = 0 \qquad (7.1)$$

The first term after the first "=" sign in (7.1) describes exciton diffusion, the second term describes the sink of excitons comprised of radiative decay $\frac{N(x)}{L_D^2}$ and Förster transfer to the

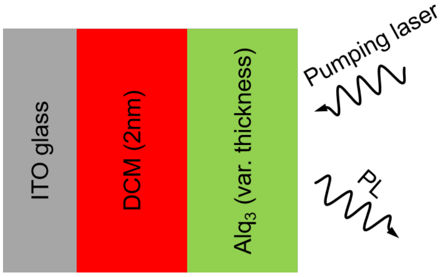

Figure 7.1: Stack used for photoluminescence quenching experiment in [70].

DCM layer $\frac{R_0^4}{x^4}\frac{N(x)}{L_D^2}$ where x denotes the distance to the DCM-Alq3 interface, L_D the exciton diffusion length and D the diffusion coefficient. Note that the Förster rate is proportional to x^{-4} instead of x^{-6} as the rate was integrated over the 2D interface (point-to-plane instead of point-to-point transfer). The last term describes a spatially constant generation term as a result of the pumping laser. Generation in the DCM layer is $G = 0$. Using the resulting exciton distribution, the PL was calculated as

$$\mathrm{PL}(d) \propto \int_0^d N(x) \frac{1}{1 + \frac{R_0^4}{x^4}} \mathrm{d}x \tag{7.2}$$

where the fraction inside the integral is the "light extraction efficiency" (fraction of radiative decay over all decay mechanisms). The resulting PL intensity as a function of the Alq3 layer thickness is shown in fig. 7.2. In order to apply the Master equation model to this problem the material parameters listed in tab. 7.1 taken from literature have been used. As this is a PL experiment, only singlets were considered in the simulation. As a first test the magnitude of disorder was varied to investigate its effects on the resulting exciton distribution. The singlet occupation numbers for varying disorder are depicted in fig. 7.3b where it is evident that for the "standard" σ-value assumed in many organic semiconductors the energetic noise completely screens any other effect. This effect is even stronger when simulated on a large

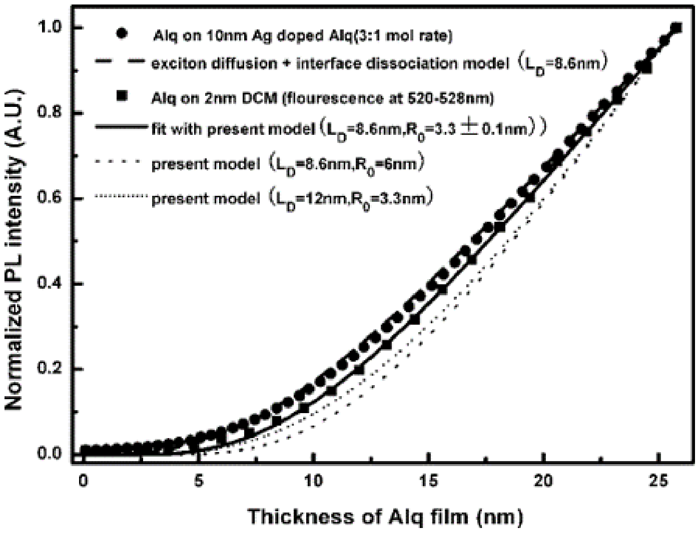

Figure 7.2: Resulting normalized PL in the Alq3 layer due to quenching. It is well visible that for thicknesses < 3.5 nm all excitons are quenched [70].

Table 7.1: Energies and lifetimes for DCM and $\mathrm{Alq_3}$.

Material	E_{LUMO} [eV]	E_{HOMO} [eV]	E^{s} [eV]	$\tau_{\mathrm{r}}^{\mathrm{s}}$ [ns]	τ_{nr} [ns]
DCM	-2.59[95]	-5.61[95]	2.21[96]	3.7[97]	5[97]
$\mathrm{Alq_3}$	-2.4[74]	-5.9[74]	2.7[98]	25[99]	16.7[100]

grid (not related to the stack in fig. 7.1) where an arbitrary linear generation profile was imposed (see fig. 7.3b). This very strong influence of the energetic disorder might emerge due to the confined transport in one dimension only. Due to the fewer possible paths for an exciton in 1D the probability is higher to encounter a highly contrasted energetic surrounding such that locally all excitons will flow to the site with lowest energy from which there's no way to escape. In 3D on the other hand there are many more possible directions to hop to with a higher probability of finding a neighboring site with energy levels close to the current ones, allowing for equilibrating transport.

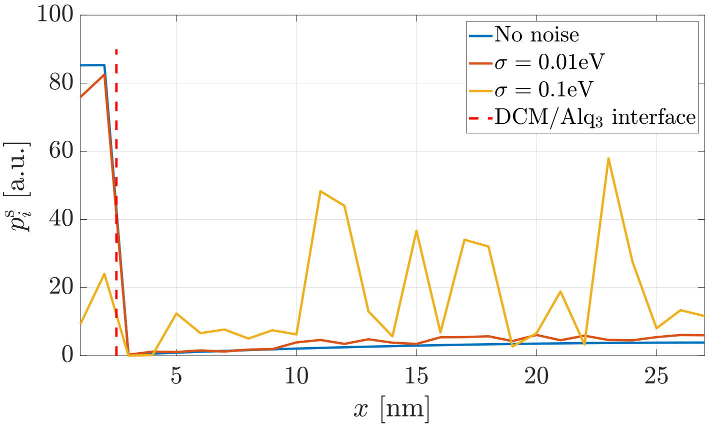

(a) Singlet occupation numbers for the stack in fig. 7.1 with different levels of disorder.

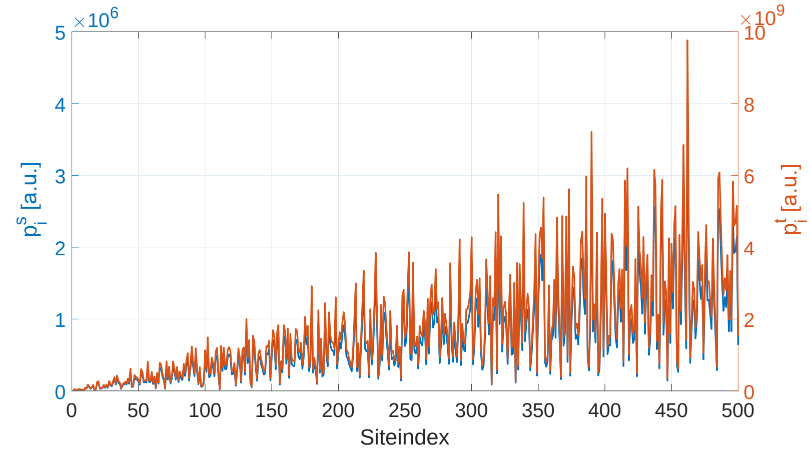

(b) 1D exciton simulation on a different, larger grid with linear generation profile and $\sigma_{E_{\mathrm{b}}} = 0.1\,\mathrm{eV}$.

Figure 7.3: Influence of energetic disorder on 1D grids.

As disorder was not part of the original model in (7.1) noise was set to zero for further simulation. In order to investigate if transport in the ordered case behaves similarly as the experimental results as well as the model applied by Wu et al., singlet occupation numbers were simulated for different Förster radii as listed in tab. 7.2 with 3.3 nm the value obtained in [70]. The resulting exciton numbers were then used to calculate a normalized luminescence intensity using

$$\mathrm{PL}(d) \propto \int_0^d N(x) \frac{1/\tau_r}{\frac{1}{\tau_r}+\frac{1}{\tau_{nr}}+\left(\frac{1}{\tau_r}+\frac{1}{\tau_{nr}}\right)\frac{R_0^4}{x^4}}\,\mathrm{d}x \tag{7.3}$$

The results are shown in fig. 7.4 from which it can be concluded that for the case where R_0^F was chosen according to the experimentally obtained value the normalized luminescence intensities match extraordinarily well.

Table 7.2: Employed Förster variations.

Case-#	R_0^F	Exponent
1	2 nm	4
2	3.3 nm	4
3	6 nm	4

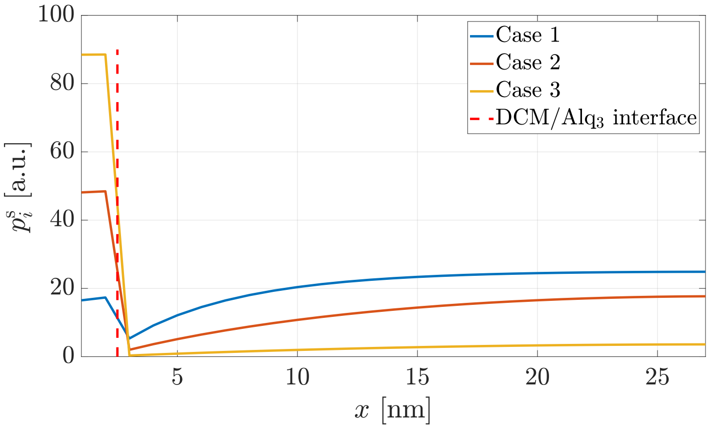

(a) Singlet occupation numbers for the stack in fig. 7.1 with different R_0^F. Note that here x includes the DCM layer unlike in (7.3).

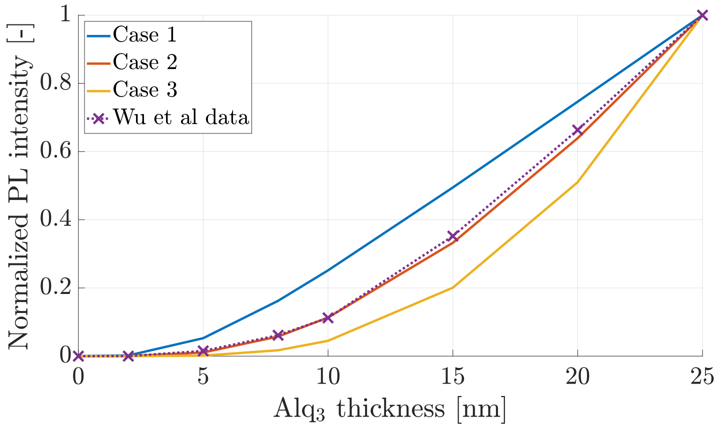

(b) Resulting normalized luminescence, data from [70] are shown by ×.

Figure 7.4: 1D ME results for the PL experiment.

7.2 3D steady-state

The main focus of the work was ultimately on full 3D simulations of the Master equations, and some steady-state results shall be presented in this section. In their original paper presenting the Master equations for excitons Zhou et al. [74] also used a Master equation formulation for the charge carrier transport and used the combined model to simulate a complete 3D OLED stack depicted in fig. 7.5a. This stack has previously been investigated by Bösing et al. [98] and formed the basis for a reference case to simulate and check certain aspects of the mathematical model. In order to evaluate the implementation described in chapter 5 this stack was used as a reference to carry out own simulations, where compared to Zhou et al. [74] the charge carrier densities and potential distribution were simulated by the commercial 1D continuum simulation software setfos and then used as static input data for the ME model (fig. 7.5).

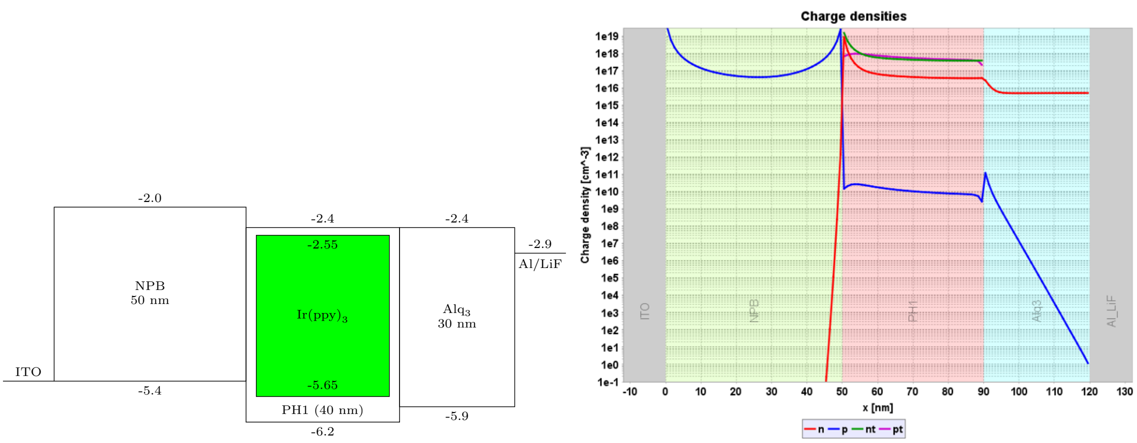

(a) OLED stack as used in [74] and [98]. **(b)** Charge carrier densities as simulated by setfos.

Figure 7.5: Input data for the 3D ME model to simulate a green OLED stack.

In the setfos model the respective energy levels of the different materials were used, where the Ir(ppy)$_3$ guest molecules were modeled as traps in the PH1 layer. The mobilities were then adjusted in order to match the IV-characteristics as presented in [74]. The resulting charge carrier density profile from fig. 7.5b was obtained at a forward-bias of 4 V. The relevant parameters for the exciton model were taken directly from [74].

The simulation was carried out on a $120 \times 30 \times 30$ grid depicted in fig. 7.6a where the numerical characteristics of the solver have already been described in section 6.2.3. Each Newton iteration for high and low carrier densities using the ILUT preconditioner took around 28 s and 15 s, respectively, where in the case of high charge carrier densities the iteration times varied quite strongly over the Newton iterations (see fig. A.1). The simulations were run on an Intel® Core™ i5-6600 CPU with four cores each at 3.30 GHz.

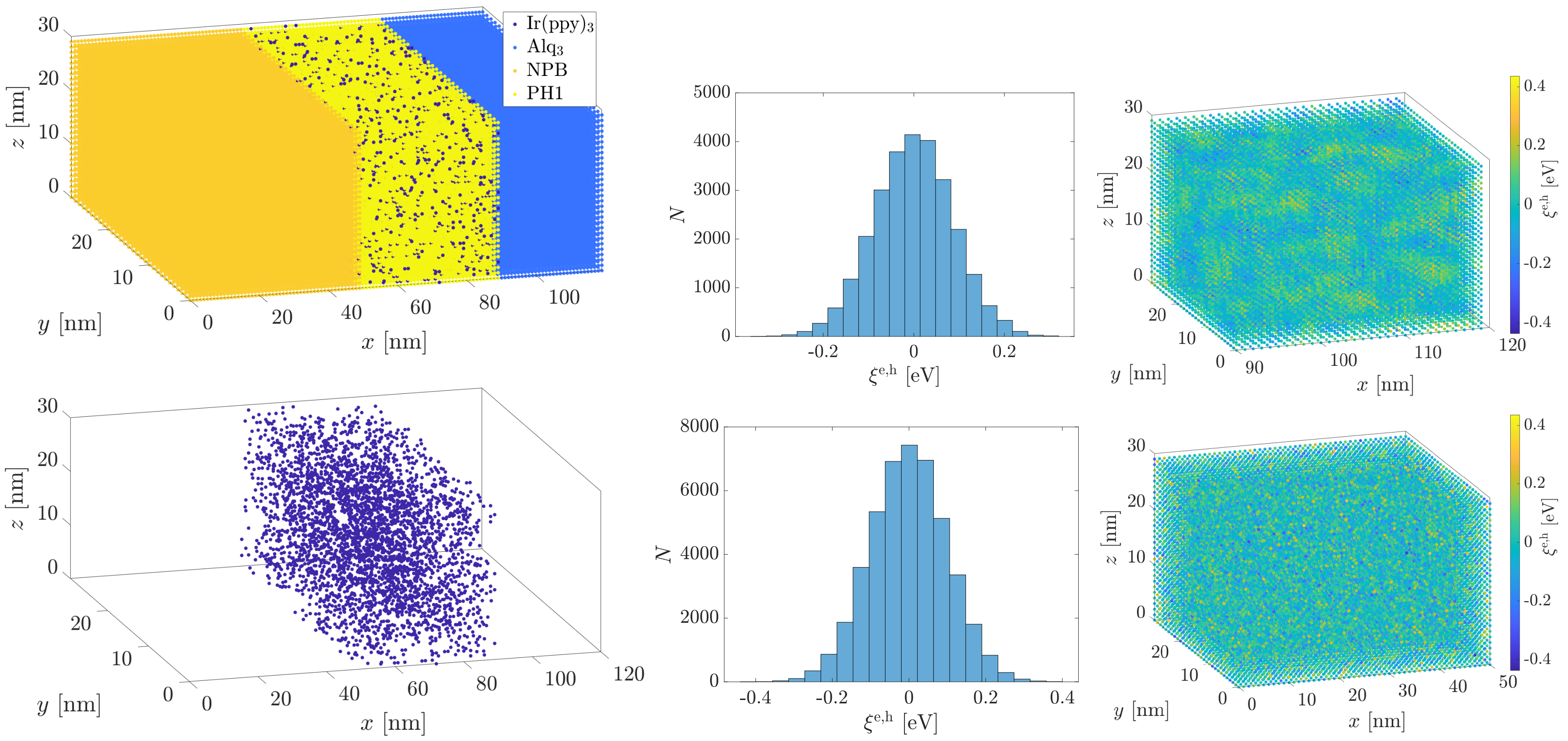

(a) Top: The complete grid. Bottom: Guest molecules ($\rho = 0.1$) in emitter layer made visible.

(b) Top: Random energy component in Alq$_3$ (correlated). Bottom: Random energy component in NPB (uncorrelated).

Figure 7.6: Simulation grid for a green OLED stack.

The resulting triplet densities averaged over the lateral dimensions can be found in fig. 7.7a for high and low carrier densities. The original setfos output corresponds to the high carrier density case which resulted in extremely high exciton densities compared to the values obtained by [74]. The reason for that was found to be an inconsistency between the setfos model for carriers and the applied ME model for excitons, where trap-trap recombination was inactive in setfos leading to a very strong accumulation of carriers on these trap levels. As these corresponded to the guest molecules in the 3D ME model those very high local densities were distributed on the guest sites where they could recombine, leading to a very high generation rate. As an improvised workaround, the carrier densities were scaled by 10^{-5} in order to get consistent recombination with literature.

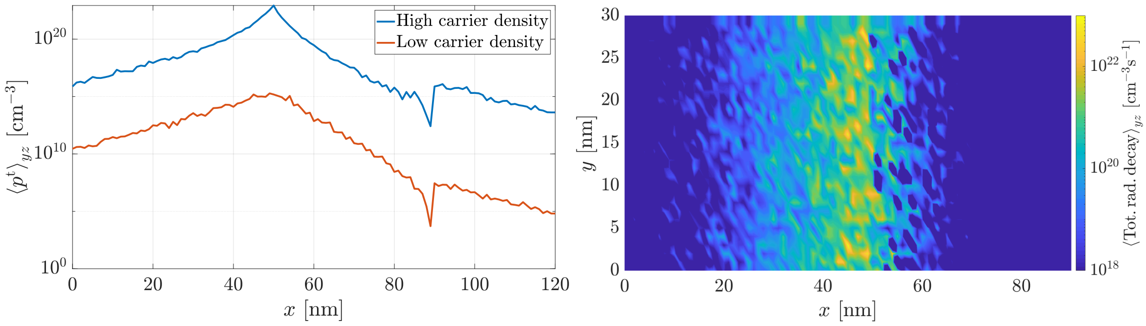

(a) Laterally averaged triplet density for before and after adjustment of carriers.

(b) 2D surface of total radiative decay events.

Figure 7.7: Example results of the 3D steady-state simulation.

Due to strong recombination close to the HTL/EML interface exciton generation in this region is also strong and some excitons are quenched by the HTL which is visible by the increased radiative decay in it. Strongest radiative decay occurs right at the interface where some dark spots inside the EML are visible. Those correspond to z-coordinates where no guest molecule was present due to the relatively low guest density of $\rho = 0.1$. Another interesting result shows when plotting triplet densities vs. triplet energies for different materials as shown in fig. 7.8. While in the Alq$_3$ layer for example transport is not limited, the equilibrium distribution follows a typical Bose-Einstein distribution given by

$$n(E) \propto \frac{1}{\exp\left(\frac{E-\mu}{k_B T}\right) - 1} \tag{7.4}$$

as is to be expected for excitons as they are Bosonic particles. Meanwhile, if the same plot is drawn for the energetic distribution of triplets in Ir(ppy)$_3$, this looks very different as in general an excitonis strongly confined on an Ir(ppy)$_3$ molecule due to the surrounding PH1 states with higher energy. Therefore, these triplets cannot move freely and relax easily towards the states with lower energy.

Finally, to check the correctness of the obtained exciton occupation numbers the balance equations (6.25) - (6.27) can be used to validate equality of total generation to total decay. The simulation was run 10 times and for each instantiation the relative error between total generation (G) and total decay (D) was calculated. The resulting relative errors are depicted

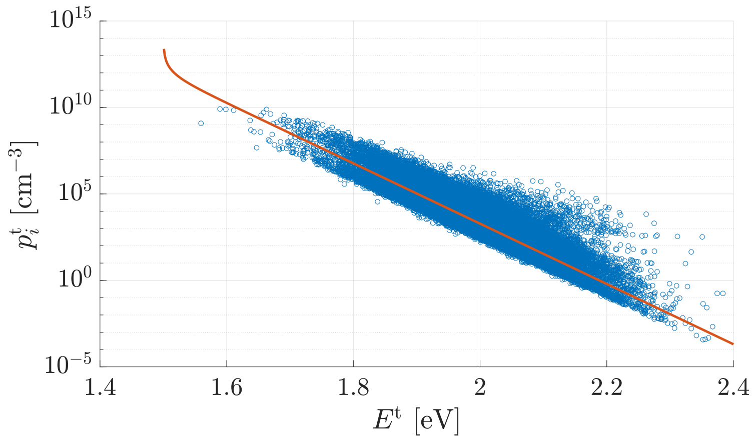

(a) p^{t} vs. E^{t} plot for Alq$_3$. Bose-Einstein distribution in orange.

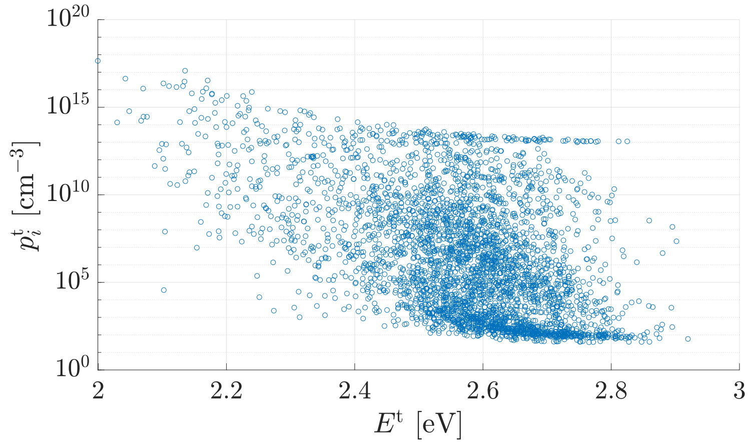

(b) p^{t} vs. E^{t} plot for Ir(ppy)$_3$.

Figure 7.8: Energetic distribution of triplets.

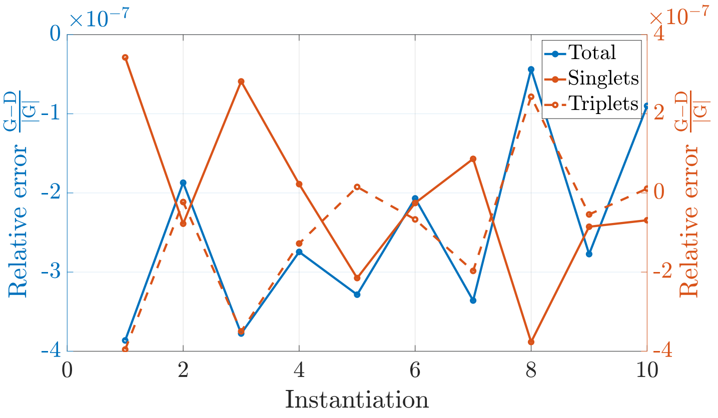

Figure 7.9: Relative mismatch between generation and decay calculated with (6.25) - (6.27) for ten different runs.

in fig. 7.9. In all cases the relative error is very low in the order of $\sim 10^{-7}$ which means the ME model equations were solved correctly by the implemented code.

This is an example which could not easily be reproduced by the continuum approach as used in setfos, due to the fact that layer interfaces there act as no-flow boundaries and the EML would need a very special treatment. To model such a guest-host system the layer would need to feature some intermediate energy levels and the different behavior of the excitons in it would make it necessary to use multiple “virtual” species where these would coexist next to each other in the continuum representing host- and guest-excitations. Transport from host to guest sites would therefore be modeled as some special kind of ISC. Furthermore, any influence of energetic disorder could only be resolved as determined by the PDF and therefore represent some mean case in the stochastic limit, as no actual realization of the random variable occurs.

7.3 3D transient

In order to generate also non-stationary results some examples using transient solvers were simulated. It can be said that transient simulations of the presented model are extremely computationally expensive, as it combines quite large 3-dimensional systems interacting on larger spatial scales with quite stiff equations, making it necessary to use implicit or at least semi-implicit solvers. Even then, often time steps cannot be taken too large which still leads to relatively high number of computed steps for each of which a large system of equation needs to be solved (possibly even more than once).

7.3.1 Influence of R_c

In the first transient simulation discussed here the influence of the cutoff-radius R_c was investigated. In order to achieve this, a grid with dimensions $20 \times 20 \times 20$ was set-up representing a host-guest system with materials equal to the EML in the previously discussed steady-state example. However, now all processes are turned off except Förster/Dexter transport between the sites and radiative decay on the Ir(ppy)$_3$ molecules (no decay on PH1!) and a fixed initial condition of

$$p_i^{\mathrm{s,t}}(0) = \begin{cases} 10^{10}\,\mathrm{cm}^{-3} & \text{if } i \in \mathrm{PH1} \\ 0 & \text{else} \end{cases} \tag{7.5}$$

Therefore, the only change in exciton occupation numbers should be possible by hopping from host to guest molecules where they decay radiatively. This process should become stronger as transport increases which can be used to determine the influence of the cutoff-radius R_c since the temporal evolution of occupation number should converge and stay equal as soon as R_c is large enough such that all the dominant transport paths are taken into account (shown schematically in fig. 7.10). The guest molecules were dispersed in the grid with a density of $\rho = 0.2$ and R_c was varied from 0 to $6a_0$, total simulation time was $10\,\mu\mathrm{s}$ using SDIRK-2a due to its L-stability and possibility to achieve stepsize control with the embedded $\hat{p} = 1$ method. The stepsize controller used $\beta = 10^{-3}$ and $\alpha = 10^{-40}$ such that control was governed by the relative error. These simulations took around $\approx 10\,\mathrm{min}$ each to compute.

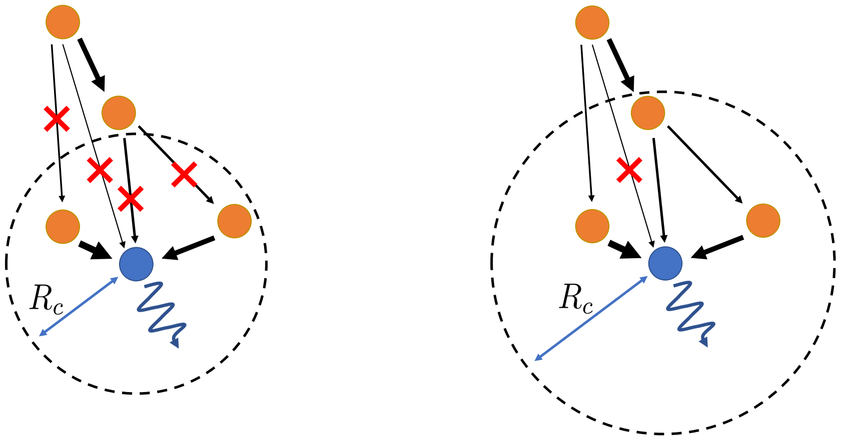

(a) Small R_c neglecting relatively strong transport paths.

(b) Large R_c where all dominant transport paths are taken into account.

Figure 7.10: Transport paths as a function of R_c. PH1 in orange, Ir(ppy)$_3$ in blue and arrow width denotes coupling strength.

The results of the simulation are shown in fig. 7.11. It is interesting to note that the total exciton count quickly converges and increasing R_c over $2a_0$ has no effect anymore, however, as shown in fig. 7.11b, if only the total excitons on PH1 molecules are plotted there is a visible difference between the curves. It is also clear that transport happens very fast and quickly a quasi-equilibrium is reached where exciton loss on PH1 is limited by the radiative decay rate on Ir(ppy)$_3$, however, this quasi-equilibrium depends on the coupling strength. The speed of transport is also visible in fig. 7.11c where the accumulation of excitons on Ir(ppy)$_3$ occurs mainly in the first $< 1\,\mu$s until the quasi-equilibrium is reached (note the finite exciton density in Ir(ppy)$_3$ is due to the detailed balance term). From this data it can be concluded that $R_c = 4a_0$ is a reasonable cutoff-radius, at least for these material parameters.

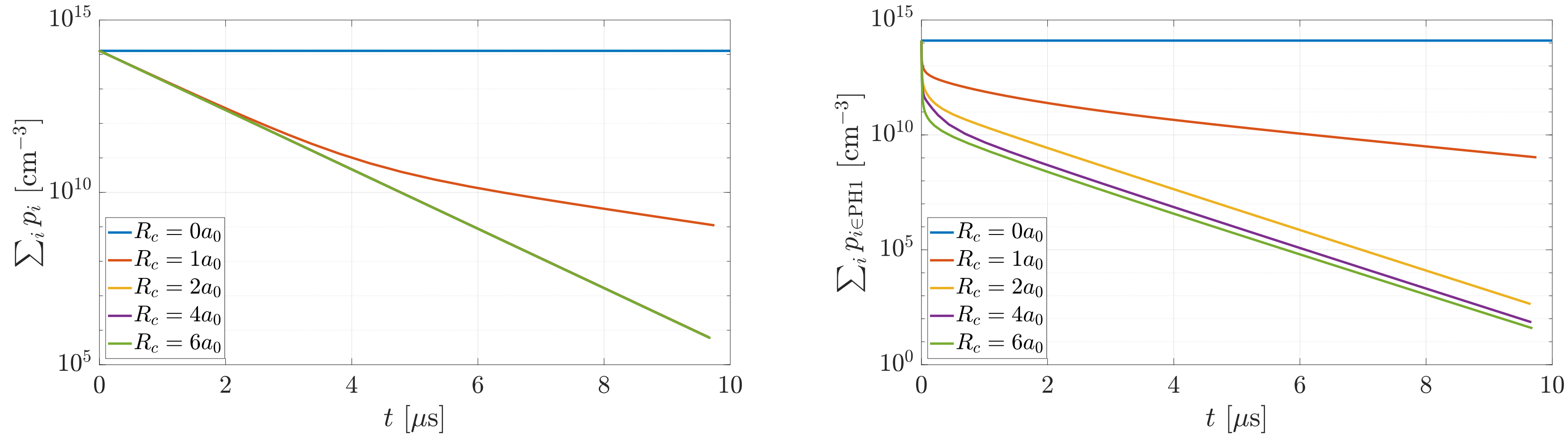

(a) Total exciton count over time.

(b) PH1 exciton count over time.

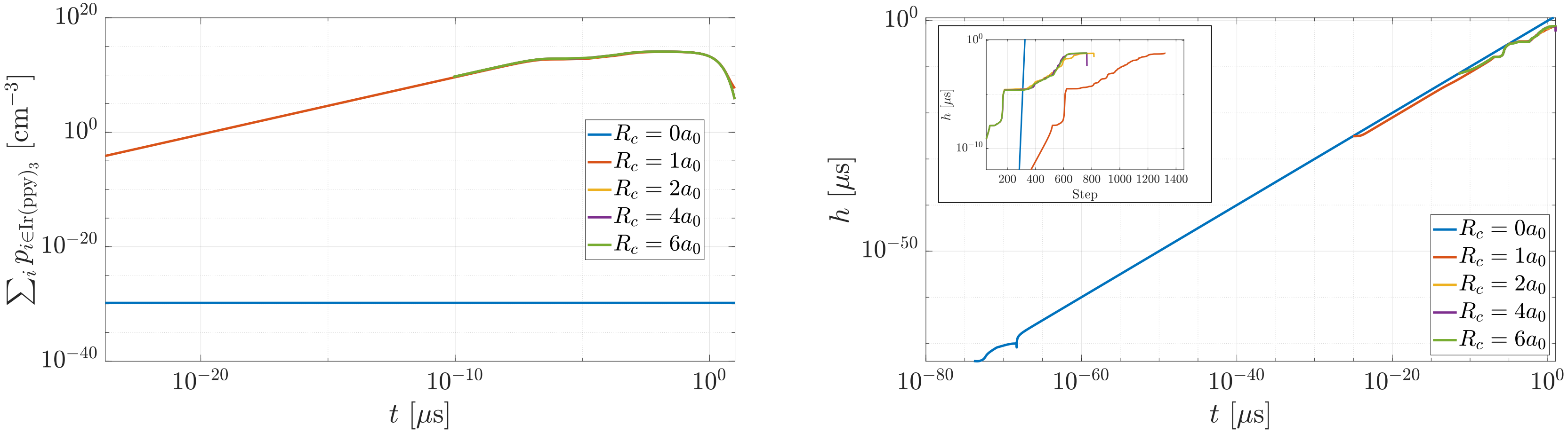

(c) Ir(ppy)$_3$ exciton count over time.

(d) Stepsize h over time. Inset: Stepsize h over integration steps.

Figure 7.11: Results of transient simulation investigating R_c.

7.3.2 OLED turn-on

In order to test the solver in case of transient input parameters, a single-layer OLED device was simulated in setfos subject to a short voltage pulse as depicted in fig. 7.12b. The OLED consisted of a single 120 nm MEH-PPV layer sandwiched between two electrodes made of gold and calcium. The stack with the respective energy layers is shown in fig. 7.12a and the parameters used for the semiconducting layer can be found in tab. 7.3. In this simplified simulation only exciton generation through recombination, exciton transport through the layer and radiative decay have been active and the simulation time was in accordance with the voltage pulse equal to 300 µs. Again, the SDIRK-2a method was used as no nonlinear system of equations needed to be solved (exciton-exciton annihilation was turned off) therefore the good stability properties of the method were a benefit considering quite rapidly changing input data. Note however that for such a simulation with high accuracy it took more than 1.5 hours to compute ≈ 1000 steps.

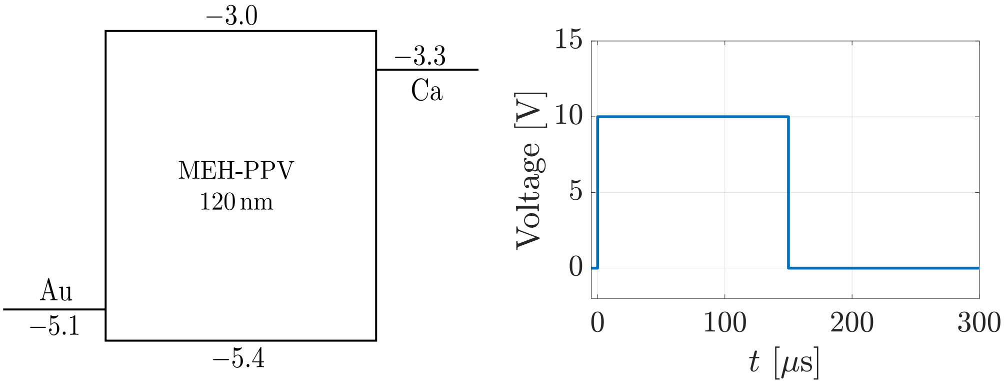

(a) HOMO/LUMO energy levels of the electrodes and semiconductor.

(b) Voltage pulse applied on the OLED.

Figure 7.12: OLED stack and imposed voltage pulse for transient turn-on simulation.

In fig. 7.13a the resulting recombination averaged over the lateral dimensions is plotted over time (carrier densities are anyway taken as constant over the lateral dimensions as there is no guest-host system present). It is clearly visible how recombination starts very strongly close to the cathode at $x = 120$ nm and starts to penetrate more into the material itself with a second smaller peak close to the anode. This pattern persists up to $t = 150$ µs when the voltage is turned off and the carriers start to drift back to their respective electrodes such that recombination at the electrodes stops very quickly, however, in the center of the device where the receding carriers meet recombination persists for longer. This pattern ultimately gives rise to the exciton distribution in fig. 7.13b which ultimately looks very similar to the recombination distribution. However, there are some subtleties which should be noted. First, all patterns are “smeared” out, e.g. the recombination peak at $x = 120$ nm appears much wider into the device, as well as after the voltage is turned off excitons are still present throughout almost the whole layer. Secondly, certain structures emerge due to the energetic disorder present in the material (again $\sigma = 0.1$ eV was assumed), showing as periodic patterns of varying exciton density. It should be kept in mind that this representation has been averaged over the lateral dimension, i.e. these lines of higher exciton densities represent layers with a higher share of states with lower exciton energy. An additional plot for a similar system where this migration to energetically more preferable states is shown can also be found in fig. A.3.

This is an example where the results of the Master equation approach can be well compared to the results obtained by setfos due to the simplicity of the model (no host-guest systems, no interfaces etc.). In 7.13c the temporal singlet distribution as simulated by setfos is shown. The order of magnitude of the two results matches very well throughout time and space, however, there are definitely some differences to mention. The first obvious distinction is the much smoother density in case of the setfos as no actual energetic noise of the exciton energies is included. Furthermore, the exciton density seems to decrease very abruptly as soon as the device is turned off which can be seen by the clear cut at $t = 150\,\mu\text{s}$. This distinction may also result from differences in the numerical integration scheme.

The first approach to this simulation was to use an explicit Cash-Karp method with constant stepsize of $h = 50\,\text{ns}$ to check if the results could be obtained with less accuracy but quicker than with implicit solvers. However, this approach completely failed and the obtained results were dominated by instabilities of the solver where the plot can be found in the appendix in fig. A.2. All areas which are not shown correspond to zero density and are therefore not visible in the logarithmic plot. Keep in mind that most probably the computed densities were even negative and then projected onto 0 as a protective measure.

Table 7.3: Excitonic parameters used for MEH-PPV.

τ	g_{Rec}	$\tau_{\text{r}}^{\text{s}}$	$\tau_{\text{r}}^{\text{t}}$	E_b^{s}	E_b^{t}
1 ns [101]	0.25	20 ns	2 µs	0.6 eV [102]	0.8 eV [102]

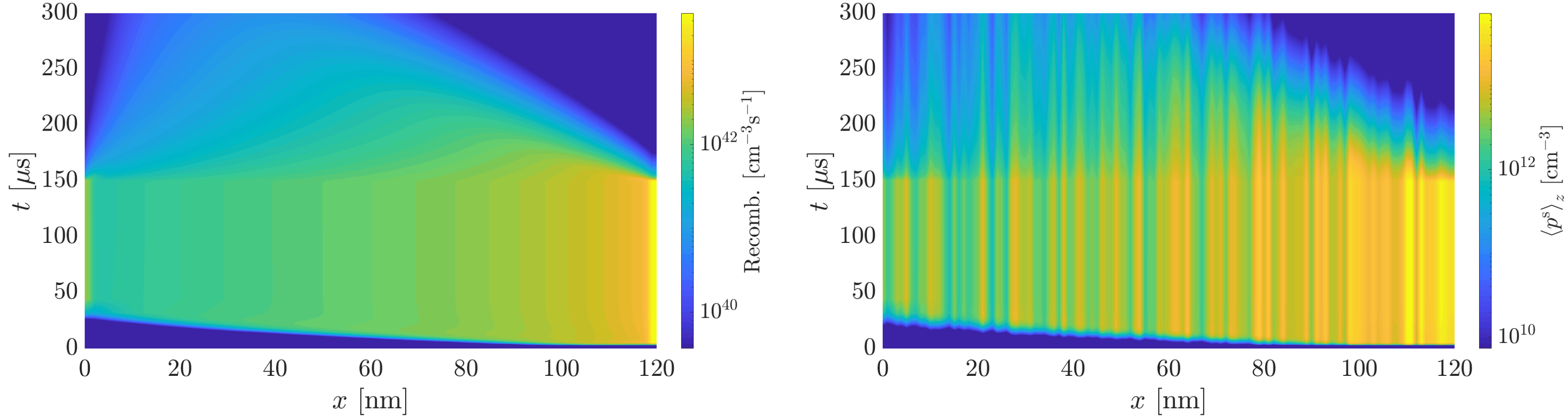

(a) Recombination along x-axis over time.

(b) Singlet distribution laterally averaged over time.

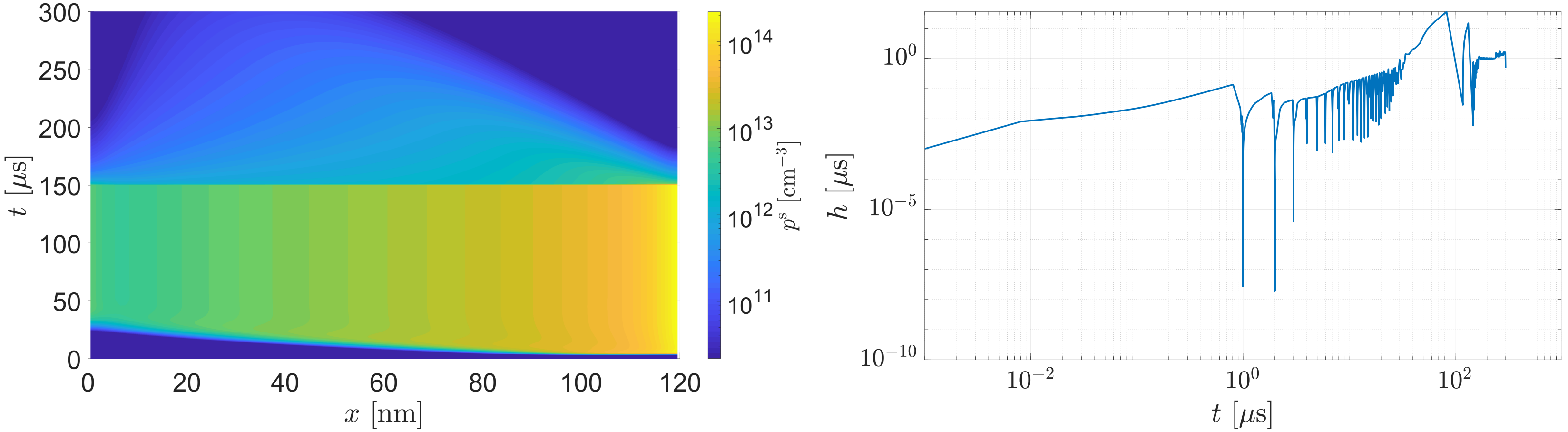

(c) Singlet distribution for the same simulation as computed directly by setfos.

(d) Stepsize h over time.

Figure 7.13: Results of transient simulation concerning OLED turn-on.

Chapter 8

Conclusions and Outlook

As a short recap, the original goals of the work are mentioned again briefly. A model should be set up using the stochastic ME approach including commonly accepted exciton mechanisms and should be implemented as a computational solver to simulate steady-state and transient situations. The solver should then be coupled to the charge carrier simulation by setfos which uses a 1D continuum approach to combine strengths of both methods where useful to support research in organic optoelectronics.

The implemented model as shown in (4.7) and (4.8) includes all mechanisms which are usually dominant in OLED devices such as (non-)radiative decay, (reverse) ISC, SPQ, TPQ and TTA of course alongside generation by charge carrier recombination and optical excitation. In this form also advanced OLED concepts such as TADF and phosphorescent emitters can be simulated quite accurately and material parameters such as lifetimes can be extracted by fitting the simulation result to experimental data. The most important characteristic however which distinguishes this model from e.g. continuum models are the transport terms which allow for physically more accurate transport by hopping from discrete sites to one another extending beyond the nearest neighbor molecule. As was described in section 4.2.5 the continuum approach using a simple diffusion constant D is equivalent for symmetric transport and strongly homogeneous materials. These assumptions do not need to be made if transport is modeled as in the ME approach which allows for more physically correct and easier modeling of multilayer devices and mixed host-guest systems.

As was shown in section 7.2 these conditions are often met in real-world devices where the EML is doped with an emitter material to increase luminescence and where many processes might be strong at interfaces, such as recombination. In these cases, it can be a strong advantage to use a 3D molecular discretization such that interfaces pose no problem and dispersed single guest molecules can be spatially resolved rendering separate exciton species to represent singlets and triplets for each material unnecessary. Different excitonic behavior on different materials is then simply achieved by determining the molecular type of the local grid point. A further result which cannot be obtained in the continuum approach is a specific energetic distribution by examining the respective excitation energies over the grid combined with the local exciton densities, as shown in 7.8 and A.4 where characteristics such as reduced exchange over the sparsely dispersed guest sites arise naturally. The example results provided in chapter 7 for steady-state as well as transient definitely show that the approach yields very good and physically reasonable results.

The model as currently implemented also has some weaknesses conceptually, though. A problem of simple sampling of the DOS and guest distribution can lead to unphysical situations if the grid size is chosen too small, as in these cases the law of large numbers is not fulfilled and the resulting distributions may not accurately represent the underlying PDF. In real devices this will never occur due to the extremely large number of molecules present. An example of such a situation can be seen in fig. 7.7b where dark spots in the radiative decay correspond to molecular chains in z-direction where due to the low guest density and grid size only host molecules were present. Other points are of course the missing exciton dissociation into free carriers which would be of utmost importance if applied to OPV. This together with the currently used rate expression for Dexter transfer would introduce field dependencies of the coupling which would need to be resolved during transient simulations, strongly increasing computational cost (the correct physical modeling of non-local quenching and annihilation would have a similar effect). The current model also assumes strongly localized excitons in ordered small-molecule materials which might also not hold in all situations. If the ME model is applied in 1D some adjustments would definitely need to be made. Taking e.g. the Förster rate dependence as R^{-4} is one of them, as well as investigations into the effect of disorder would be needed due to the very strong confinement caused by disorder if transport is limited to one dimension only.

Most of these mentioned problems might be fixed rather easily. The main disadvantage of the 3D ME approach compared to model used in setfos for the exciton simulation is the computational cost. 3D simulations are definitely feasible on standard computers yet with computation times far beyond what is needed using the 1D continuum approach. This is mostly caused by the combination of 3D grids with long-range interactions leading to large numbers of couplings to be considered. Numerical tricks as considered in this work could not levitate this problem and the functions $\boldsymbol{f}(t, \boldsymbol{p})$ themselves are quite costly to evaluate, even though the assumed time-independence of the transport terms decreased the impact of that fact. Furthermore, the stiffness of the diffusion-dominated ME makes transient simulations generally costly as a large system of equations needs to be solved at each step in order to ensure stability. This fact could make it difficult to finally couple the two models if the coupling goes both ways, as a single iteration for the large ME model takes much more computation time than for the 1D continuum model. If these systems both depend on each other, such a coupling will eliminate the advantage in speed of the continuum solver as computation time will be completely dominated by the 3D ME solver.

For future work some of the mentioned points about the model should be improved. This includes the introduction of physically correct transport parameters which take the exact combination of materials into account as well as an adjustment to the correlation lengths which are currently all equal to the cutoff radius R_c. This may not be justified as disorder correlation scales as $\mathcal{O}\left(R^{-3}\right)$ and possibly farther molecules need to be taken into account than for transport. The introduction of off-diagonal disorder might also be interesting to investigate. Possible additions to the model might be dissociation for OPV and use of location-dependent radiative decay rates due to cavity-effects (Purcell-effect [103]) which can be provided by setfos. In general, the code developed during this work might be implemented directly into setfos to make sure that all modeling parameters are consistent. Some further smaller things might still be considered as well, such as uniting coupled and decoupled solvers and checking the impact of using field-dependent Dexter rates.

Bibliography

[1] Masaki Tanaka, Hiroki Noda, Hajime Nakanotani, and Chihaya Adachi. Effect of Carrier Balance on Device Degradation of Organic Light-Emitting Diodes Based on Thermally Activated Delayed Fluorescence Emitters. *Advanced Electronic Materials*, 51:1800708, 2019. ISSN 2199160X. doi: 10.1002/aelm.201800708.

[2] Zi Shuai Wang, Wei E. I. Sha, and Wallace C. H. Choy. Exciton delocalization incorporated drift-diffusion model for bulk-heterojunction organic solar cells. *Journal of Applied Physics*, 120(21):213101, 2016. ISSN 0065-2385. doi: 10.1063/1.4970958.

[3] Francesco Santoni, Thomas Brown, Francesca Brunetti, Sara Pescetelli, Andrea Reale, Aldo Di Carlo, and Matthias auf der Maur. A universal drift-diffusion simulator and its application to OLED simulations. In Joachim Piprek and Morten Willatzen, editors, *17th International Conference on Numerical Simulation of Optoelectronic Devices*, pages 103–104, Piscataway, NJ, 2017. IEEE. ISBN 978-1-5090-5323-0. doi: 10.1109/NUSOD.2017.8010012.

[4] R. Coehoorn, P. A. Bobbert, and H. van Eersel. Effect of exciton diffusion on the triplet-triplet annihilation rate in organic semiconductor host-guest systems. *Physical Review B*, 99(2), 2019. ISSN 1098-0121. doi: 10.1103/PhysRevB.99.024201.

[5] Oleksandr V. Mikhnenko, Hamed Azimi, Markus Scharber, Mauro Morana, Paul W. M. Blom, and Maria Antonietta Loi. Exciton diffusion length in narrow bandgap polymers. *Energy & Environmental Science*, 5(5):6960, 2012. ISSN 1754-5692. doi: 10.1039/c2ee03466b.

[6] M. Z. Szymanski, B. Luszczynska, and D. Djurado. Modeling the Transient Space-Charge-Limited Current Response of Organic Semiconductor Diodes Using the Master Equation Approach. *IEEE Journal of Selected Topics in Quantum Electronics*, 19(5):1–7, 2013. ISSN 1077-260X. doi: 10.1109/JSTQE.2013.2246775.

[7] J. J. M. van der Holst, M. A. Uijttewaal, B. Ramachandhran, R. Coehoorn, P. A. Bobbert, G. A. de Wijs, and R. A. de Groot. Modeling and analysis of the three-dimensional current density in sandwich-type single-carrier devices of disordered organic semiconductors. *Physical Review B*, 79(8), 2009. ISSN 1098-0121. doi: 10.1103/PhysRevB.79.085203.

[8] Weifeng Zhou, Christoph Zimmermann, and Christoph Jungemann. Numerical Capacitance Analysis of Single-Layer OLEDs Based on the Master Equation. *IEEE Transactions on Electron Devices*, 63(12):4919–4923, 2016. ISSN 0018-9383. doi: 10.1109/TED.2016.2618484.

[9] A. Pochettino and A. Sella. Photoelectric behavior of anthracene. *Acad. Lincei Rend*, 15: 355–363, 1906.

[10] A. Bernanose. Electroluminescence of organic compounds. *British Journal of Applied Physics*, 6(S4):S54–S55, 1955. ISSN 0508-3443. doi: 10.1088/0508-3443/6/S4/319.

[11] C. W. Tang and S. A. VanSlyke. Organic electroluminescent diodes. *Applied Physics Letters*, 51(12):913–915, 1987. ISSN 0003-6951. doi: 10.1063/1.98799.

[12] J. H. Burroughes, D. D. C. Bradley, A. R. Brown, R. N. Marks, K. Mackay, R. H. Friend, P. L. Burns, and A. B. Holmes. Light-emitting diodes based on conjugated polymers. *Nature*, 347 (6293):539–541, 1990. ISSN 0028-0836. doi: 10.1038/347539a0.

[13] Tarek Zaki. *Short-Channel Organic Thin-Film Transistors: Fabrication, Characterization, Modeling and Circuit Demonstration*. Springer Theses, Recognizing Outstanding Ph.D. Research. Springer International Publishing, Cham and s.l., 2015. ISBN 9783319188959. doi: 10.1007/978-3-319-18896-6. URL http://dx.doi.org/10.1007/978-3-319-18896-6.

[14] J. E. Jones. On the Determination of Molecular Fields. II. From the Equation of State of a Gas. *Proceedings of the Royal Society A: Mathematical, Physical and Engineering Sciences*, 106(738):463–477, 1924. ISSN 1364-5021. doi: 10.1098/rspa.1924.0082.

[15] Eric V. Anslyn and Dennis A. Dougherty. *Modern physical organic chemistry.* University Science Books, Mill Valley, California, 2006. ISBN 9781891389313.

[16] Andreas Schenk. Semiconductor Devices - Physical Bases and Simulation: Script, 2017.

[17] Shuichiro Ogawa, editor. *Organic Electronics Materials and Devices.* Springer Japan, Tokyo, 2015. ISBN 978-4-431-55653-4. doi: 10.1007/978-4-431-55654-1.

[18] José C.S. Costa, Ricardo J.S. Taveira, Carlos F.R.A.C. Lima, Adélio Mendes, and Luís M.N.B.F. Santos. Optical band gaps of organic semiconductor materials. *Optical Materials*, 58:51–60, 2016. ISSN 09253467. doi: 10.1016/j.optmat.2016.03.041.

[19] H. Bässler. Charge transport in molecularly doped polymers. *Philosophical Magazine B*, 50(3): 347–362, 1984. ISSN 1364-2812. doi: 10.1080/13642818408238860.

[20] H. Bässler. Localized states and electronic transport in single component organic solids with diagonal disorder. *physica status solidi (b)*, 107(1):9–54, 1981. ISSN 03701972. doi: 10.1002/pssb.2221070102.

[21] Oleksandr V. Mikhnenko. *Dynamics of singlet and triplet excitons in organic semiconductors.* s.n.] and University Library Groningen] [Host], [S.l. and [Groningen, op. 2011. ISBN 9789036752022.

[22] Dunlap, Parris, and Kenkre. Charge-Dipole Model for the Universal Field Dependence of Mobilities in Molecularly Doped Polymers. *Physical review letters*, 77(3):542–545, 1996. doi: 10.1103/PhysRevLett.77.542.

[23] S. V. Novikov, D. H. Dunlap, V. M. Kenkre, P. E. Parris, and A. V. Vannikov. Essential Role of Correlations in Governing Charge Transport in Disordered Organic Materials. *Physical Review Letters*, 81(20):4472–4475, 1998. ISSN 0031-9007. doi: 10.1103/PhysRevLett.81.4472.

[24] Z. G. Yu, D. L. Smith, A. Saxena, R. L. Martin, and A. R. Bishop. Molecular geometry fluctuation model for the mobility of conjugated polymers. *Physical Review Letters*, 84(4): 721–724, 2000. ISSN 0031-9007. doi: 10.1103/PhysRevLett.84.721.

[25] Gernot Frenking. Perspective on "Quantentheoretische Beiträge zum Benzolproblem. I. Die Elektronenkonfiguration des Benzols und verwandter Beziehungen". *Theoretical Chemistry Accounts: Theory, Computation, and Modeling (Theoretica Chimica Acta)*, 103(3-4):187–189, 2000. ISSN 1432-881X. doi: 10.1007/s002149900023.

[26] Rudolf Ernst Peierls. *More surprises in theoretical physics.* Princeton series in physics. Princeton Univ. Pr, Princeton, NJ, 1991. ISBN 0691025223.

[27] U. Heinemeyer, R. Scholz, L. Gisslén, M. I. Alonso, J. O. Ossó, M. Garriga, A. Hinderhofer, M. Kytka, S. Kowarik, A. Gerlach, and F. Schreiber. Exciton-phonon coupling in diindenoperylene thin films. *Physical Review B*, 78(8):926, 2008. ISSN 1098-0121. doi: 10.1103/PhysRevB.78.085210.

[28] Anna Köhler and Heinz Bässler. *Electronic processes in organic semiconductors: An introduction.* Wiley-VCH Verlag GmbH & Co, Weinheim, 2015. ISBN 9783527685141. URL http://search.ebscohost.com/login.aspx?direct=true&scope=site&db=nlebk&AN=968962.

[29] Rudolph A. Marcus. Electron transfer reactions in chemistry. Theory and experiment. *Reviews of Modern Physics*, 65(3):599–610, 1993. ISSN 0034-6861. doi: 10.1103/RevModPhys.65.599.

[30] Holger Frauenrath. Organic Electronic Materials: Synthesis, Properties and Applications, 2018.

[31] Allen Miller and Elihu Abrahams. Impurity Conduction at Low Concentrations. *Physical Review*, 120(3):745–755, 1960. ISSN 0031-899X. doi: 10.1103/PhysRev.120.745.

[32] H. Bässler. Charge Transport in Disordered Organic Photoconductors a Monte Carlo Simulation Study. *physica status solidi (b)*, 175(1):15–56, 1993. ISSN 03701972. doi: 10.1002/pssb.2221750102.

[33] Fraunhofer Institute for Solar Energy Systems, ISE. Photovoltaics Report. URL https://www.ise.fraunhofer.de/content/dam/ise/de/documents/publications/studies/Photovoltaics-Report.pdf.

[34] Ayodhya Nath Tiwari, Yaroslav Romanyuk, and Stephan Bücheler. Solar Cells, 2017.

[35] Julian Burschka, Norman Pellet, Soo-Jin Moon, Robin Humphry-Baker, Peng Gao, Mohammad K. Nazeeruddin, and Michael Grätzel. Sequential deposition as a route to high-performance perovskite-sensitized solar cells. *Nature*, 499(7458):316–319, 2013. ISSN 0028-0836. doi: 10.1038/nature12340.

[36] Martin A. Green, Yoshihiro Hishikawa, Ewan d. Dunlop, Dean H. Levi, Jochen Hohl-Ebinger, Masahiro Yoshita, and Anita W.Y. Ho-Baillie. Solar cell efficiency tables (Version 53). *Progress in Photovoltaics: Research and Applications*, 27(1):3–12, 2019. ISSN 10627995. doi: 10.1002/pip.3102.

[37] Brian O'Regan and Michael Grätzel. A low-cost, high-efficiency solar cell based on dye-sensitized colloidal TiO2 films. *Nature*, 353(6346):737–740, 1991. ISSN 0028-0836. doi: 10.1038/353737a0.

[38] Giles E. Eperon, Samuel D. Stranks, Christopher Menelaou, Michael B. Johnston, Laura M. Herz, and Henry J. Snaith. Formamidinium lead trihalide: a broadly tunable perovskite for efficient planar heterojunction solar cells. *Energy & Environmental Science*, 7(3):982, 2014. ISSN 1754-5692. doi: 10.1039/c3ee43822h.

[39] J. Blochwitz, T. Fritz, M. Pfeiffer, K. Leo, D. M. Alloway, P. A. Lee, and N. R. Armstrong. Interface electronic structure of organic semiconductors with controlled doping levels. *Organic Electronics*, 2(2):97–104, 2001. ISSN 15661199. doi: 10.1016/S1566-1199(01)00016-7.

[40] J. Frenkel. On the Transformation of light into Heat in Solids. I. *Physical Review*, 37(1):17–44, 1931. ISSN 0031-899X. doi: 10.1103/PhysRev.37.17.

[41] M. V. Fischetti. Monte Carlo simulation of transport in technologically significant semiconductors of the diamond and zinc-blende structures. I. Homogeneous transport. *IEEE Transactions on Electron Devices*, 38(3):634–649, 1991. ISSN 0018-9383. doi: 10.1109/16.75176.

[42] Gregory H. Wannier. The Structure of Electronic Excitation Levels in Insulating Crystals. *Physical Review*, 52(3):191–197, 1937. ISSN 0031-899X. doi: 10.1103/PhysRev.52.191.

[43] Vanessa Wood. Solid State Electronics and Optics: Script, 2017.

[44] P. G. Cummins and D. A. Dunmur. The electric permittivity of crystalline anthracene. *Journal of Physics D: Applied Physics*, 7(3):451–454, 1974. ISSN 00223727. doi: 10.1088/0022-3727/7/3/312.

[45] A. S. Davydov. THE THEORY OF MOLECULAR EXCITONS. *Soviet Physics Uspekhi*, 7(2):145–178, 1964. ISSN 0038-5670. doi: 10.1070/PU1964v007n02ABEH003659.

[46] Michael J. Waters, Daniel Hashemi, and John Kieffer. Semiclassical Model for Calculating Exciton and Polaron Pair Energetics at Interfaces. *ARXIV*, 2017.

[47] M. Scheidler, U. Lemmer, R. Kersting, S. Karg, W. Riess, B. Cleve, R. F. Mahrt, H. Kurz, H. Bässler, E. O. Göbel, and P. Thomas. Monte Carlo study of picosecond exciton relaxation and dissociation in poly(phenylenevinylene). *Physical Review B*, 54(8):5536–5544, 1996. ISSN 1098-0121. doi: 10.1103/PhysRevB.54.5536.

[48] Alice Ruini, Marilia J. Caldas, Giovanni Bussi, and Elisa Molinari. Solid state effects on exciton states and optical properties of PPV. *Physical Review Letters*, 88(20):206403, 2002. ISSN 0031-9007. doi: 10.1103/PhysRevLett.88.206403.

[49] Markus Schwoerer and Hans Christoph Wolf. *Organic Molecular Solids.* Wiley-VCH, Hoboken, 2008. ISBN 9783527405404. URL http://search.ebscohost.com/login.aspx?direct=true&scope=site&db=nlebk&db=nlabk&AN=246660.

[50] J. J. M. van der Holst, F. W. A. van Oost, R. Coehoorn, and P. A. Bobbert. Electron-hole recombination in disordered organic semiconductors: Validity of the Langevin formula. *Physical Review B*, 80(23):433, 2009. ISSN 1098-0121. doi: 10.1103/PhysRevB.80.235202.

[51] Hartmut Yersin. Triplet Emitters for OLED Applications. Mechanisms of Exciton Trapping and Control of Emission Properties. In H. Yersin, editor, *Transition Metal and Rare Earth Compounds*, volume 241 of *Topics in Current Chemistry*, pages 1–26. Springer, Berlin and Heidelberg, 2004. ISBN 978-3-540-20948-5. doi: 10.1007/b96858.

[52] Paul Langevin. Recombinaison et mobilites des ions dans les gaz. *Ann. Chim. Phys*, 28(433): 122, 1903.

[53] J. Franck and E. G. Dymond. Elementary processes of photochemical reactions. *Transactions of the Faraday Society*, 21(February):536, 1926. ISSN 0014-7672. doi: 10.1039/tf9262100536.

[54] Edward Condon. A Theory of Intensity Distribution in Band Systems. *Physical Review*, 28(6): 1182–1201, 1926. ISSN 0031-899X. doi: 10.1103/PhysRev.28.1182.

[55] Raymond T. Birge. The Band Spectra of Carbon Monoxide. *Physical Review*, 28(6):1157–1181, 1926. ISSN 0031-899X. doi: 10.1103/PhysRev.28.1157.

[56] Roel Menting. *Lichtinduzierter Energie- und Elektronentransfer in komplexe Bausteinen fur artifizielle Photosynthesesyteme.* Diplomarbeit, Humboldt-Universität zu Berlin, 2010.

[57] Th. Förster. Zwischenmolekulare Energiewanderung und Fluoreszenz. *Annalen der Physik*, 437(1-2):55–75, 1948. ISSN 00033804. doi: 10.1002/andp.19484370105.

[58] Bernard Valeur and Mário Nuno Berberan-Santos. *Molecular fluorescence: Principles and applications.* Wiley-VCH, Weinheim, 2. ed. edition, 2012. ISBN 978-3-527-32837-6.

[59] Vicki Cleave, Goghan Yahioglu, Pierre Le Barny, Richard H. Friend, and Nir Tessler. Harvesting Singlet and Triplet Energy in Polymer LEDs. *Advanced Materials*, 11(4): 285–288, 1999. ISSN 09359648. doi: 10.1002/(SICI)1521-4095(199903)11:4{\textless}285::AID-ADMA285{\textgreater}3.0.CO;2-N.

[60] D. L. Dexter. A Theory of Sensitized Luminescence in Solids. *The Journal of Chemical Physics*, 21(5):836–850, 1953. ISSN 0031-7918. doi: 10.1063/1.1699044.

[61] Alexandra Olaya-Castro and Gregory D. Scholes. Energy transfer from Förster–Dexter theory to quantum coherent light-harvesting. *International Reviews in Physical Chemistry*, 30(1): 49–77, 2011. ISSN 0144-235X. doi: 10.1080/0144235X.2010.537060.

[62] spectral overlap. In Miloslav Nič, Jiří Jirát, Bedřich Košata, Aubrey Jenkins, and Alan McNaught, editors, *IUPAC Compendium of Chemical Terminology.* IUPAC, Research Triagle Park, NC, 2009. ISBN 0-9678550-9-8. doi: 10.1351/goldbook.S05818.

[63] Chihaya Adachi, Marc A. Baldo, Mark E. Thompson, and Stephen R. Forrest. Nearly 100% internal phosphorescence efficiency in an organic light-emitting device. *Journal of Applied Physics*, 90(10):5048–5051, 2001. ISSN 0065-2385. doi: 10.1063/1.1409582.

[64] Ye Tao, Kai Yuan, Ting Chen, Peng Xu, Huanhuan Li, Runfeng Chen, Chao Zheng, Lei Zhang, and Wei Huang. Thermally activated delayed fluorescence materials towards the breakthrough of organoelectronics. *Advanced materials (Deerfield Beach, Fla.)*, 26(47):7931–7958, 2014. doi: 10.1002/adma.201402532.

[65] Daniele Fazzi, Giulia Grancini, Margherita Maiuri, Daniele Brida, Giulio Cerullo, and Guglielmo Lanzani. Ultrafast internal conversion in a low band gap polymer for photovoltaics: experimental and theoretical study. *Physical chemistry chemical physics : PCCP*, 14(18):6367–6374, 2012. doi: 10.1039/c2cp23917e.

[66] Thomas Engel and Philip J. Reid. *Physical chemistry.* Pearson Benjamin Cummings, San Francisco, 2006. ISBN 080533842X.

[67] R. Coehoorn, P. A. Bobbert, and H. van Eersel. Förster-type triplet-polaron quenching in disordered organic semiconductors. *Physical Review B*, 96(18), 2017. ISSN 1098-0121. doi: 10.1103/PhysRevB.96.184203.

[68] H. van Eersel, P. A. Bobbert, R. A. J. Janssen, and R. Coehoorn. Monte Carlo study of efficiency roll-off of phosphorescent organic light-emitting diodes: Evidence for dominant role of triplet-polaron quenching. *Applied Physics Letters*, 105(14):143303, 2014. ISSN 0003-6951. doi: 10.1063/1.4897534.

[69] Noémie Elgrishi, Kelley J. Rountree, Brian d. McCarthy, Eric S. Rountree, Thomas T. Eisenhart, and Jillian L. Dempsey. A Practical Beginner's Guide to Cyclic Voltammetry. *Journal of Chemical Education*, 95(2):197–206, 2018. ISSN 0021-9584. doi: 10.1021/acs.jchemed.7b00361.

[70] Y. Wu, H. R. Wu, Y. C. Zhou, Y. Q. Zhan, J. Zhou, X. M. Ding, and X. Y. Hou. Excitation energy transfer between tris-(8-hydroxyquinoline) aluminum and a red dye. *Applied Physics Letters*, 88(12):123512, 2006. ISSN 0003-6951. doi: 10.1063/1.2188374.

[71] T. A. Beierlein, B. Ruhstaller, D. J. Gundlach, H. Riel, S. Karg, C. Rost, and W. Rieß. Investigation of internal processes in organic light-emitting devices using thin sensing layers. *Synthetic Metals*, 138(1-2):213–221, 2003. ISSN 03796779. doi: 10.1016/S0379-6779(02)01269-9.

[72] Raúl Toral. Introduction to Master Equations, 2014. URL https://ifisc.uib-csic.es/users/raul/CURSOS/SP/Introduction_to_master_equations.pdf.

[73] Crispin W. Gardiner. *Stochastic methods: A handbook for the natural and social sciences.* Springer complexity. Springer, Berlin, 4. ed. edition, 2009. ISBN 9783540707134.

[74] Weifeng Zhou, Christoph Zimmermann, and Christoph A. Jungemann. Simulation of exciton effects in OLEDs based on the master equation. In Franky So, Chihaya Adachi, and Jang-Joo Kim, editors, *Organic Light Emitting Materials and Devices XXI*, page 63, 2017. doi: 10.1117/12.2269972. URL https://www.spiedigitallibrary.org/conference-proceedings-of-spie/10362/2269972/Simulation-of-exciton-effects-in-OLEDs-based-on-the-master/10.1117/12.2269972.full.

[75] Tai-Sang Ahn, Nicholas Wright, and Christopher J. Bardeen. The effects of orientational and energetic disorder on Forster energy migration along a one-dimensional lattice. *Chemical Physics Letters*, 446(1-3):43–48, 2007. ISSN 00092614. doi: 10.1016/j.cplett.2007.08.003.

[76] Nicolaas G. van Kampen. *Stochastic processes in physics and chemistry.* North-Holland personal library. Elsevier, Amsterdam, 3. ed., repr edition, 2008. ISBN 978-0-444-52965-7.

[77] Evelyne Knapp. Numerical methods for comprehensive characterization of charge transport in organic light-emitting devices.

[78] George Marsaglia. Choosing a Point from the Surface of a Sphere. *The Annals of Mathematical Statistics*, 43(2):645–646, 1972. ISSN 0003-4851. doi: 10.1214/aoms/1177692644.

[79] Christoph Kirsch. Script MND2: Mathematik: Numerik und Differenzialgleichungen 2, 2018.

[80] C. G. Broyden. A Class of Methods for Solving Nonlinear Simultaneous Equations. *Mathematics of Computation*, 19(92):577, 1965. ISSN 0025-5718. doi: 10.2307/2003941.

[81] Christopher A. Kennedy and Mark H. Carpenter. Diagonally Implicit Runge-Kutta Methods for Ordinary Differential Equations. A Review.

[82] Y. Saad. *Iterative methods for sparse linear systems.* Society for Industrial and Applied Mathematics (SIAM 3600 Market Street Floor 6 Philadelphia PA 19104), Philadelphia, Pa., 2nd ed. edition, 2003. ISBN 978-0898715347.

[83] Peter Arbenz. FEM and Sparse Linear System Solving: Lecture 10, Nov 24, 2017: Preconditioning, 2017.

[84] Yousef Saad. ILUT: A dual threshold incomplete LU factorization. *Numerical Linear Algebra with Applications*, 1(4):387–402, 1994. ISSN 1070-5325. doi: 10.1002/nla.1680010405.

[85] Ron S. Dembo, Stanley C. Eisenstat, and Trond Steihaug. Inexact Newton Methods. *SIAM Journal on Numerical Analysis*, 19(2):400–408, 1982. ISSN 0036-1429. doi: 10.1137/0719025.

[86] Roger P. Pawlowski, John N. Shadid, Joseph P. Simonis, and Homer F. Walker. Globalization Techniques for Newton–Krylov Methods and Applications to the Fully Coupled Solution of the Navier–Stokes Equations. *SIAM Review*, 48(4):700–721, 2006. ISSN 0036-1445. doi: 10.1137/S0036144504443511.

[87] John Denholm Lambert. *Numerical methods for ordinary differential systems: The initial value problem*. Wiley, Chichester, reprint edition, 1997. ISBN 0 471 92990 5.

[88] Ernst Hairer and Gerhard Wanner. *Solving Ordinary Differential Equations II: Stiff and differential-algebraic problems*, volume 14 of *Springer series in computational mathematics*. Springer Berlin Heidelberg, Berlin, Heidelberg, 2., rev. ed., corrected printing, 1. softcover printing edition, 1996. ISBN 978-3-642-05220-0. doi: 10.1007/978-3-642-05221-7.

[89] John Charles Butcher. *Numerical methods for ordinary differential equations*. Wiley, Chichester, UK, 3rd ed. edition, 2016. ISBN 9781119121534. URL http://onlinelibrary.wiley.com/book/10.1002/9781119121534.

[90] W. Kutta. Beitrag zur näherungweisen Integration totaler Differentialgleichungen. 1901.

[91] Joseph F. Boudreau and Eric S. Swanson. *Applied computational physics*, volume 1. Oxford University Press, Oxford, United Kingdom, first edition edition, 2018. ISBN 978-0-19-870863-6. doi: 10.1093/oso/9780198708636.001.0001.

[92] Olavi Nevanlinna and Aarne H. Sipila. A Nonexistence Theorem for Explicit A-Stable Methods. *Mathematics of Computation*, 28(128):1053, 1974. ISSN 0025-5718. doi: 10.2307/2005364.

[93] P. Ellsiepen and S. Hartmann. Remarks on the interpretation of current non–linear finite element analyses as differential–algebraic equations. *International Journal for Numerical Methods in Engineering*, 51(6):679–707, 2001. ISSN 00295981. doi: 10.1002/nme.179.abs.

[94] Peter Kaps and Peter Rentrop. Generalized Runge-Kutta methods of order four with stepsize control for stiff ordinary differential equations. *Numerische Mathematik*, 33(1):55–68, 1979. doi: 10.1007/BF01396495.

[95] Reda M. El-Shishtawy, Abdullah M. Asiri, Saadullah G. Aziz, and Shaaban A. K. Elroby. Molecular design of donor-acceptor dyes for efficient dye-sensitized solar cells I: A DFT study. *Journal of molecular modeling*, 20(6):2241, 2014. doi: 10.1007/s00894-014-2241-5.

[96] Martine. Meyer, Jean Claude. Mialocq, and Bruno. Perly. Photoinduced intramolecular charge transfer and trans-cis isomerization of the DCM styrene dye: Picosecond and nanosecond laser spectroscopy, high-performance liquid chromatography, and nuclear magnetic resonance studies. *The Journal of Physical Chemistry*, 94(1):98–104, 1990. ISSN 0022-3654. doi: 10.1021/j100364a015.

[97] A. A. Turban, S. L. Bondarev, V. N. Knyukshto, and A. P. Stupak. Quenching of fluorescence for fluoro derivatives of the laser dye DCM in polar solutions. *Journal of Applied Spectroscopy*, 73(5):678–685, 2006. ISSN 0021-9037. doi: 10.1007/s10812-006-0139-4.

[98] Manuel Bösing, Christoph Zimmermann, Florian Lindla, Frank Jessen, Philipp van Gemmern, Dietrich Bertram, Nico Meyer, Dietmar Keiper, M. Heuken, Holger Kalisch, and Rolf H. Jansen. Introduction of Innovative Dopant Concentration Profiles to Broaden the Recombination Zone of Phosphorescent OVPD-Processed Organic Light Emitting Diodes. *MRS Proceedings*, 1154, 2009. ISSN 1946-4274. doi: 10.1557/PROC-1154-B11-05.

[99] M. A. Baldo and S. R. Forrest. Transient analysis of organic electrophosphorescence: I. Transient analysis of triplet energy transfer. *Physical Review B*, 62(16):10958–10966, 2000. ISSN 1098-0121. doi: 10.1103/PhysRevB.62.10958.

[100] Wenming Li, Shanlin Pan, and Lewis J. Rothberg. Emissive efficiency enhancement of Alq 3 and prospects for plasmon-enhanced organic electroluminescence. SPIE Proceedings, page 703224. SPIE, 2008. doi: 10.1117/12.796177.

[101] Peter C. Eklund and Apparao M. Rao. *Fullerene Polymers and Fullerene Polymer Composites*, volume 38 of *Springer Series in Materials Science*. Springer, Berlin and Heidelberg, 2000. ISBN 978-3-642-08441-6. doi: 10.1007/978-3-662-04269-4. URL http://dx.doi.org/10.1007/978-3-662-04269-4.

[102] S. J. Martin, Helen Mellor, Donal D.C. Bradley, and P. L. Burn. Electroabsorption studies of PPV and MEH-PPV. *Optical Materials*, 9(1-4):88–93, 1998. ISSN 09253467. doi: 10.1016/S0925-3467(97)00153-5.

[103] Edward Mills Purcell and H. C. Torrey. Proceedings of the american physical society. *Phys. Rev*, 69(11-12):674, 1946.

Appendix A

A.1 Definition of matrices for decoupled equations

$$(\boldsymbol{W}_{\mathrm{F}}^{\mathrm{s}})_{ij} = \begin{cases} -\sum_{f\neq i} w_{jf}^{\mathrm{F,s}} & \text{if } j = i \\ w_{ji}^{\mathrm{F,s}} & \text{otherwise} \end{cases}$$

$$(\boldsymbol{W}_{\mathrm{F}}^{\mathrm{t}})_{ij} = \begin{cases} -\sum_{f\neq i} w_{jf}^{\mathrm{F,t}} & \text{if } j = i \\ w_{ji}^{\mathrm{F,t}} & \text{otherwise} \end{cases}$$

$$(\boldsymbol{W}_{\mathrm{D}}^{\mathrm{s}})_{ij} = \begin{cases} -\sum_{d\neq i} w_{jd}^{\mathrm{D,s}} & \text{if } j = i \\ w_{ji}^{\mathrm{D,s}} & \text{otherwise} \end{cases}$$

$$(\boldsymbol{W}_{\mathrm{D}}^{\mathrm{t}})_{ij} = \begin{cases} -\sum_{d\neq i} w_{jd}^{\mathrm{D,t}} & \text{if } j = i \\ w_{ji}^{\mathrm{D,t}} & \text{otherwise} \end{cases}$$

$$(\boldsymbol{D}_{\mathrm{Dec}}^{\mathrm{s}})_{ij} = \begin{cases} \frac{1}{\tau_{\mathrm{r},i}^{\mathrm{s}}} + \frac{1}{\tau_{\mathrm{nr},i}^{\mathrm{s}}} & \text{if } j = i \\ 0 & \text{otherwise} \end{cases}$$

$$(\boldsymbol{D}_{\mathrm{Dec}}^{\mathrm{t}})_{ij} = \begin{cases} \frac{1}{\tau_{\mathrm{r},i}^{\mathrm{t}}} + \frac{1}{\tau_{\mathrm{nr},i}^{\mathrm{t}}} & \text{if } j = i \\ 0 & \text{otherwise} \end{cases}$$

$$(\boldsymbol{D}_{\mathrm{ISC}}^{\mathrm{s}})_{ij} = \begin{cases} \frac{1}{\tau_{\mathrm{ISC},i}} & \text{if } j = i \\ 0 & \text{otherwise} \end{cases}$$

$$\begin{aligned} \boldsymbol{M}^{\mathrm{s}} = & \boldsymbol{W}_{F}^{\mathrm{s}} + \boldsymbol{W}_{D}^{\mathrm{s}} - \boldsymbol{D}_{\mathrm{Dec}}^{\mathrm{s}} - \boldsymbol{D}_{\mathrm{ISC}}^{\mathrm{s}} \\ & - \boldsymbol{D}_{\mathrm{SPQ}} - \boldsymbol{D}_{\mathrm{RecB}}^{\mathrm{s}} \end{aligned}$$

$$\begin{aligned} \boldsymbol{M}^{\mathrm{t}} = & \boldsymbol{W}_{F}^{\mathrm{t}} + \boldsymbol{W}_{D}^{\mathrm{t}} - \boldsymbol{D}_{\mathrm{Dec}}^{\mathrm{t}} - \boldsymbol{D}_{\mathrm{ISC}}^{\mathrm{t}} \\ & - \boldsymbol{D}_{\mathrm{TPQ}} - \boldsymbol{D}_{\mathrm{RecB}}^{\mathrm{t}} \end{aligned}$$

$$(\boldsymbol{b}^{\mathrm{s}})_i = \exp\left(\frac{E_{\mathrm{b},i}^{\mathrm{s}} - E_{\mathrm{g},i}}{k_B T}\right)$$

$$(\boldsymbol{D}_{\mathrm{ISC}}^{\mathrm{t}})_{ij} = \begin{cases} \frac{1}{\tau_{\mathrm{ISC},i}} \exp\left(\frac{E_{\mathrm{b},i}^{\mathrm{s}} - E_{\mathrm{b},i}^{\mathrm{t}}}{k_B T}\right) & \text{if } j = i \\ 0 & \text{otherwise} \end{cases}$$

$$(\boldsymbol{D}_{\mathrm{SPQ}})_{ij} = \begin{cases} \frac{p_i^{\mathrm{e}} + p_i^{\mathrm{h}}}{\tau_{\mathrm{SPQ},i}} & \text{if } j = i \\ 0 & \text{otherwise} \end{cases}$$

$$(\boldsymbol{D}_{\mathrm{TPQ}})_{ij} = \begin{cases} \frac{p_i^{\mathrm{e}} + p_i^{\mathrm{h}}}{\tau_{\mathrm{TPQ},i}} & \text{if } j = i \\ 0 & \text{otherwise} \end{cases}$$

$$(\boldsymbol{D}_{\mathrm{RecB}}^{\mathrm{s}})_{ij} = \begin{cases} g_{\mathrm{Rec},i} \frac{1}{\tau_i} \exp\left(-\frac{E_{\mathrm{b},i}^{\mathrm{s}}}{k_B T}\right) & \text{if } j = i \\ 0 & \text{otherwise} \end{cases}$$

$$(\boldsymbol{D}_{\mathrm{RecB}}^{\mathrm{t}})_{ij} = \begin{cases} (1 - g_{\mathrm{Rec},i}) \frac{1}{\tau_i} \exp\left(-\frac{E_{\mathrm{b},i}^{\mathrm{t}}}{k_B T}\right) & \text{if } j = i \\ 0 & \text{otherwise} \end{cases}$$

$$(\boldsymbol{D}_{\mathrm{TTA}})_{ij} = \begin{cases} \frac{1}{\tau_{\mathrm{TTA},i}} & \text{if } j = i \\ 0 & \text{otherwise} \end{cases}$$

$$(\boldsymbol{D}_{\mathrm{p}}^{\mathrm{t}})_{ij} = \begin{cases} p_i^{\mathrm{t}} & \text{if } j = i \\ 0 & \text{otherwise} \end{cases}$$

$$(\boldsymbol{b}^{\mathrm{t}})_i = \exp\left(\frac{E_{\mathrm{b},i}^{\mathrm{t}} - E_{\mathrm{g},i}}{k_B T}\right)$$

$$(\boldsymbol{b}_{\mathrm{Rec}}^{\mathrm{s}})_i = g_{\mathrm{Rec},i} \frac{p_i^{\mathrm{e}} p_i^{\mathrm{h}}}{\tau_i}$$

$$(\boldsymbol{b}_{\mathrm{Rec}}^{\mathrm{t}})_i = (1 - g_{\mathrm{Rec},i}) \frac{p_i^{\mathrm{e}} p_i^{\mathrm{h}}}{\tau_i}$$

$$(\boldsymbol{b}_{\mathrm{Opt}}^{\mathrm{s}})_i = g_{\mathrm{Opt},i} G_i$$

$$(\boldsymbol{b}_{\mathrm{Opt}}^{\mathrm{t}})_i = (1 - g_{\mathrm{Opt},i}) G_i$$

$$(\boldsymbol{d}^2(\boldsymbol{p}^{\mathrm{t}}))_i = (p_i^{\mathrm{t}})^2$$

A.2 Derivation of balance equations

Only the derivation for the total exciton generation and decay balance equation is shown, it goes analogous for the single species. We sum up both equations (4.7) and (4.8)

$$
\begin{aligned}
\frac{\mathrm{d}p_i^{\mathrm{s}}}{\mathrm{d}t} + \frac{\mathrm{d}p_i^{\mathrm{t}}}{\mathrm{d}t} = \frac{\mathrm{d}p_i^{\mathrm{s}} + p_i^{\mathrm{t}}}{\mathrm{d}t} = &\sum_{f\neq i} \left[p_f^{\mathrm{s}}\omega_{fi}^{\mathrm{F,s}} - p_i^{\mathrm{s}}\omega_{if}^{\mathrm{F,s}}\right] + \sum_{d\neq i} \left[p_d^{\mathrm{s}}\omega_{di}^{\mathrm{D,s}} - p_i^{\mathrm{s}}\omega_{id}^{\mathrm{D,s}}\right] \\
&+ \left(\frac{1}{\tau_{\mathrm{r},i}^{\mathrm{s}}} + \frac{1}{\tau_{\mathrm{nr},i}^{\mathrm{s}}}\right)\left(\exp\left(\frac{E_{\mathrm{b},i}^{\mathrm{s}} - E_{\mathrm{g},i}}{k_B T}\right) - p_i^{\mathrm{s}}\right) \\
&+ \frac{p_i^{\mathrm{t}}}{\tau_{\mathrm{ISC},i}} \cdot \exp\left(\frac{E_{\mathrm{b},i}^{\mathrm{s}} - E_{\mathrm{b},i}^{\mathrm{t}}}{k_B T}\right) - \frac{p_i^{\mathrm{s}}}{\tau_{\mathrm{ISC},i}} \\
&- \frac{p_i^{\mathrm{s}}\left(p_i^{\mathrm{e}} + p_i^{\mathrm{h}}\right)}{\tau_{\mathrm{SPQ},i}} + \frac{\left(p_i^{\mathrm{t}}\right)^2}{2\tau_{\mathrm{TTA},i}} \\
&+ g_{\mathrm{Rec},i}\left(\frac{p_i^{\mathrm{e}}p_i^{\mathrm{h}}}{\tau_i} - \frac{p_i^{\mathrm{s}}}{\tau_i}\exp\left(-\frac{E_{\mathrm{b},i}^{\mathrm{s}}}{k_B T}\right)\right) + g_{\mathrm{Opt},i}G_i \\
&+ \sum_{f\neq i} \left[p_f^{\mathrm{t}}\omega_{fi}^{\mathrm{F,t}} - p_i^{\mathrm{t}}\omega_{if}^{\mathrm{F,t}}\right] + \sum_{d\neq i} \left[p_d^{\mathrm{t}}\omega_{di}^{\mathrm{D,t}} - p_i^{\mathrm{t}}\omega_{id}^{\mathrm{D,t}}\right] \\
&+ \left(\frac{1}{\tau_{\mathrm{r},i}^{\mathrm{t}}} + \frac{1}{\tau_{\mathrm{nr},i}^{\mathrm{t}}}\right)\left(\exp\left(\frac{E_{\mathrm{b},i}^{\mathrm{t}} - E_{\mathrm{g},i}}{k_B T}\right) - p_i^{\mathrm{t}}\right) \\
&+ \frac{p_i^{\mathrm{s}}}{\tau_{\mathrm{ISC},i}} - \frac{p_i^{\mathrm{t}}}{\tau_{\mathrm{ISC},i}} \cdot \exp\left(\frac{E_{\mathrm{b},i}^{\mathrm{s}} - E_{\mathrm{b},i}^{\mathrm{t}}}{k_B T}\right) \\
&- \frac{p_i^{\mathrm{t}}\left(p_i^{\mathrm{e}} + p_i^{\mathrm{h}}\right)}{\tau_{\mathrm{TPQ},i}} - \frac{\left(p_i^{\mathrm{t}}\right)^2}{\tau_{\mathrm{TTA},i}} \\
&+ (1 - g_{\mathrm{Rec},i})\left(\frac{p_i^{\mathrm{e}}p_i^{\mathrm{h}}}{\tau_i} - \frac{p_i^{\mathrm{t}}}{\tau_i}\exp\left(-\frac{E_{\mathrm{b},i}^{\mathrm{t}}}{k_B T}\right)\right) + (1 - g_{\mathrm{Opt},i})G_i \\
\overset{SS}{=} \quad & 0
\end{aligned}
\tag{A.1}
$$

Next, this expression is summed over all sites in the grid for the total occupation number

$$
\begin{aligned}
\sum_i^N \frac{\mathrm{d}p_i^{\mathrm{s}} + p_i^{\mathrm{t}}}{\mathrm{d}t} = &\sum_i^N \sum_{f\neq i} \left[p_f^{\mathrm{s}}\omega_{fi}^{\mathrm{F,s}} - p_i^{\mathrm{s}}\omega_{if}^{\mathrm{F,s}}\right] + \sum_i^N \sum_{d\neq i} \left[p_d^{\mathrm{s}}\omega_{di}^{\mathrm{D,s}} - p_i^{\mathrm{s}}\omega_{id}^{\mathrm{D,s}}\right] \\
&+ \sum_i^N \sum_{f\neq i} \left[p_f^{\mathrm{t}}\omega_{fi}^{\mathrm{F,t}} - p_i^{\mathrm{t}}\omega_{if}^{\mathrm{F,t}}\right] + \sum_i^N \sum_{d\neq i} \left[p_d^{\mathrm{t}}\omega_{di}^{\mathrm{D,t}} - p_i^{\mathrm{t}}\omega_{id}^{\mathrm{D,t}}\right] \\
&+ \sum_i^N \left(\frac{1}{\tau_{\mathrm{r},i}^{\mathrm{s}}} + \frac{1}{\tau_{\mathrm{nr},i}^{\mathrm{s}}}\right)\left(\exp\left(\frac{E_{\mathrm{b},i}^{\mathrm{s}} - E_{\mathrm{g},i}}{k_B T}\right) - p_i^{\mathrm{s}}\right) \\
&+ \sum_i^N \left(\frac{1}{\tau_{\mathrm{r},i}^{\mathrm{t}}} + \frac{1}{\tau_{\mathrm{nr},i}^{\mathrm{t}}}\right)\left(\exp\left(\frac{E_{\mathrm{b},i}^{\mathrm{t}} - E_{\mathrm{g},i}}{k_B T}\right) - p_i^{\mathrm{t}}\right) \\
&- \sum_i^N \frac{p_i^{\mathrm{s}}\left(p_i^{\mathrm{e}} + p_i^{\mathrm{h}}\right)}{\tau_{\mathrm{SPQ},i}} - \sum_i^N \frac{p_i^{\mathrm{t}}\left(p_i^{\mathrm{e}} + p_i^{\mathrm{h}}\right)}{\tau_{\mathrm{TPQ},i}} - \sum_i^N \frac{\left(p_i^{\mathrm{t}}\right)^2}{2\tau_{\mathrm{TTA},i}} \\
&+ \sum_i^N g_{\mathrm{Rec},i}\left(\frac{p_i^{\mathrm{e}}p_i^{\mathrm{h}}}{\tau_i} - \frac{p_i^{\mathrm{s}}}{\tau_i}\exp\left(-\frac{E_{\mathrm{b},i}^{\mathrm{s}}}{k_B T}\right)\right) \\
&+ \sum_i^N (1 - g_{\mathrm{Rec},i})\left(\frac{p_i^{\mathrm{e}}p_i^{\mathrm{h}}}{\tau_i} - \frac{p_i^{\mathrm{t}}}{\tau_i}\exp\left(-\frac{E_{\mathrm{b},i}^{\mathrm{t}}}{k_B T}\right)\right) + \sum_i^N G_i \\
\overset{SS}{=} \quad & 0
\end{aligned}
\tag{A.2}
$$

where the inter-system crossing terms cancelled and the optical generation efficiencies added up to $g_{\mathrm{Opt},1} + (1 - g_{\mathrm{Opt},1}) = 1$. The TTA term now stands as a pure decay term as one triplet is lost per annihilation event. In the first two lines we can use the following equivalency due to the double summation

$$\sum_{\substack{i,j\\ j\neq i}}^{N} [a_i b_{ij}] \equiv \sum_{\substack{i,j\\ j\neq i}}^{N} [a_j b_{ji}] \tag{A.3}$$

and therefore, all transport terms cancel (i.e. transport does not create or annihilate any excitons). This leads after some further algebraic permutations to the final balance equation as given in (6.27)

$$\begin{aligned}
&\sum_{i}^{N}\left(\frac{1}{\tau^{\mathrm{s}}_{\mathrm{r},i}}+\frac{1}{\tau^{\mathrm{s}}_{\mathrm{nr},i}}\right)\exp\left(\frac{E^{\mathrm{s}}_{\mathrm{b},i}-E_{\mathrm{g},i}}{k_B T}\right)\\
&+\sum_{i}^{N}\left(\frac{1}{\tau^{\mathrm{t}}_{\mathrm{r},i}}+\frac{1}{\tau^{\mathrm{t}}_{\mathrm{nr},i}}\right)\exp\left(\frac{E^{\mathrm{t}}_{\mathrm{b},i}-E_{\mathrm{g},i}}{k_B T}\right)\\
&+\sum_{i}^{N}\frac{p^{\mathrm{e}}_i p^{\mathrm{h}}_i}{\tau_i}+\sum_{i}^{N} G_i\\
=\;&\sum_{i}^{N}\left(\frac{1}{\tau^{\mathrm{s}}_{\mathrm{r},i}}+\frac{1}{\tau^{\mathrm{s}}_{\mathrm{nr},i}}\right)p^{\mathrm{s}}_i+\sum_{i}^{N}\left(\frac{1}{\tau^{\mathrm{t}}_{\mathrm{r},i}}+\frac{1}{\tau^{\mathrm{t}}_{\mathrm{nr},i}}\right)p^{\mathrm{t}}_i\\
&+\sum_{i}^{N} g_{\mathrm{Rec},i}\frac{p^{\mathrm{s}}_i}{\tau}\exp\left(-\frac{E^{\mathrm{s}}_{\mathrm{b},i}}{k_B T}\right)+\sum_{i}^{N}(1-g_{\mathrm{Rec},i})\frac{p^{\mathrm{t}}_i}{\tau}\exp\left(-\frac{E^{\mathrm{t}}_{\mathrm{b},i}}{k_B T}\right)\\
&+\sum_{i}^{N}\left[\left(p^{\mathrm{e}}_i+p^{\mathrm{h}}_i\right)\left(\frac{p^{\mathrm{s}}_i}{\tau_{\mathrm{SPQ},i}}+\frac{p^{\mathrm{t}}_i}{\tau_{\mathrm{TPQ},i}}\right)\right]+\sum_{i}^{N}\frac{\left(p^{\mathrm{t}}_i\right)^2}{2\tau_{\mathrm{TTA},i}}
\end{aligned} \tag{A.4}$$

A.3 Scalar ODE solution derivation

Dahlquist

The Dahquist test equation is easily solved by separation of variables

$$\frac{\mathrm{d}y}{\mathrm{d}t} = \lambda y \tag{A.5}$$

$$\Leftrightarrow \quad \int \frac{1}{y}\mathrm{d}y = \int \lambda \mathrm{d}t \tag{A.6}$$

$$\Leftrightarrow \quad \ln(y) = \lambda t + C \tag{A.7}$$

$$\Rightarrow \quad y = A\exp(\lambda t) \tag{A.8}$$

Example from [79]

The given ODE

$$\frac{\mathrm{d}y}{\mathrm{d}t} = \frac{2}{t}y + y^2 - 1 \tag{A.9}$$

is a linear inhomogeneous ODE of first order with non-constant coefficients. The general solution is given by

$$y = C\exp\left(-\int f(t)\mathrm{d}t\right) + \exp\left(-\int f(t)\mathrm{d}t\right)\int g(t)\exp\left(\int f(t)\mathrm{d}t\right)\mathrm{d}t \tag{A.10}$$

with

$$f(t) = -\frac{2}{t} \tag{A.11}$$

$$g(t) = t^2 - 1 \tag{A.12}$$

Inserting (A.11) and (A.12) into (A.10) the integrals evaluate to

$$\int f(t)\mathrm{d}t = -2\int \frac{2}{t}\mathrm{d}t \qquad = -2\ln(t) + C_1 \tag{A.13}$$

$$\int g(t)\exp\left(\int f(t)\mathrm{d}t\right)\mathrm{d}t = \int \exp\left(C_1\right) - \frac{1}{t^2}\exp\left(C_1\right)\mathrm{d}t = \exp\left(C_1\right)\left(t + \frac{1}{t}\right) + C_2 \tag{A.14}$$

which leads to the final solution

$$y = t^3 + t^2\left(\frac{C}{\exp(C_1)} + \frac{C_2}{\exp(C_1)}\right) + t = t^3 + At^2 + t \tag{A.15}$$

Riccati

The Riccati equation

$$\frac{\mathrm{d}y}{\mathrm{d}t} = \frac{4}{t^2} - \frac{6}{t}y + y^2 \tag{A.16}$$

can be solved by transforming the equation into different ODE of second order

$$\frac{\mathrm{d}^2u}{\mathrm{d}t^2} + \frac{6}{t}\frac{\mathrm{d}u}{\mathrm{d}t} + \frac{4}{t^2}u = 0 \tag{A.17}$$

By taking the ansatz $u = t^r$ this becomes

$$r(r-1)t^{r-2} + 6rt^{r-2} + 4t^{r-2} = 0 \overset{t\neq 0}{\Longrightarrow} r(r-1) + 6r + 4 = 0 \tag{A.18}$$

with the solutions $r_1 = -1$ and $r_2 = -4$. Because (A.17) is linear in u the solution can be constructed as a linear combination by

$$u(t) = C_1t^{-1} + C_2t^{-4} \tag{A.19}$$

The solution to the original Riccati equation can now be obtained by back-transformation

$$y = -\frac{{}^{\mathrm{d}u}/_{\mathrm{d}t}}{u} = \frac{C_1t^{-2} + 4C_2t^{-5}}{C_1t^{-1} + C_2t^{-4}} \overset{A={}^{C_2}/_{C_1}}{\Longrightarrow} y = \frac{t^{-2} + 4At^{-5}}{t^{-1} + At^{-4}} \tag{A.20}$$

A.4 Butcher tableaus

The Butcher tableaus for the different methods are given here as implemented.

A.4.1 Explicit

Euler

$$\begin{array}{c|c} 0 & \\ \hline & 1 \end{array}$$

Heun (trapezoidal rule)

$$\begin{array}{c|cc}
0 & & \\
\frac{1}{2} & 1 & \\
\hline
 & \frac{1}{2} & \frac{1}{2}
\end{array}$$

RK32

$$\begin{array}{c|ccc}
0 & & & \\
\frac{1}{2} & \frac{1}{2} & & \\
1 & -1 & 2 & \\
\hline
 & \frac{1}{6} & \frac{2}{3} & \frac{1}{6}
\end{array}$$

Classic Runge-Kutta

$$\begin{array}{c|cccc}
0 & & & & \\
\frac{1}{2} & \frac{1}{2} & & & \\
\frac{1}{2} & 0 & \frac{1}{2} & & \\
1 & 0 & 0 & 1 & \\
\hline
 & \frac{1}{6} & \frac{1}{3} & \frac{1}{3} & \frac{1}{6}
\end{array}$$

Heun-Euler

$$\begin{array}{c|cc}
0 & & \\
1 & 1 & \\
\hline
 & \frac{1}{2} & \frac{1}{2} \\
 & 1 & 0
\end{array}$$

Cash-Karp

$$\begin{array}{c|cccccc}
0 & & & & & & \\
\frac{1}{5} & \frac{1}{5} & & & & & \\
\frac{3}{10} & \frac{3}{40} & \frac{9}{40} & & & & \\
\frac{3}{5} & \frac{3}{10} & -\frac{9}{10} & \frac{6}{5} & & & \\
1 & -\frac{11}{54} & \frac{5}{2} & -\frac{70}{27} & \frac{35}{27} & & \\
\frac{7}{8} & \frac{1631}{55296} & \frac{175}{512} & \frac{575}{13824} & \frac{44275}{110592} & \frac{253}{4096} & \\
\hline
 & \frac{37}{378} & 0 & \frac{250}{621} & \frac{125}{594} & 0 & \frac{512}{1771} \\
 & \frac{2825}{27648} & 0 & \frac{18575}{48384} & \frac{13525}{55296} & \frac{277}{14336} & \frac{1}{4}
\end{array}$$

A.4.2 SDIRK

SDIRK2a

$$\begin{array}{c|cc}
1-\frac{\sqrt{2}}{2} & 1-\frac{\sqrt{2}}{2} & \\
1 & \frac{\sqrt{2}}{2} & 1-\frac{\sqrt{2}}{2} \\
\hline
 & \frac{\sqrt{2}}{2} & 1-\frac{\sqrt{2}}{2} \\
 & 1-(2-\frac{5}{4}\sqrt{2}) & 2-\frac{5}{4}\sqrt{2}
\end{array}$$

SDIRK4

$$
\begin{array}{c|ccccc}
\frac{1}{4} & \frac{1}{4} & & & & \\
\frac{3}{4} & \frac{1}{2} & \frac{1}{4} & & & \\
\frac{11}{20} & \frac{17}{50} & -\frac{1}{25} & \frac{1}{4} & & \\
\frac{1}{2} & \frac{371}{1360} & -\frac{137}{2720} & \frac{15}{544} & \frac{1}{4} & \\
1 & \frac{25}{24} & -\frac{49}{48} & \frac{125}{16} & -\frac{85}{12} & \frac{1}{4} \\
\hline
 & \frac{25}{24} & -\frac{49}{48} & \frac{125}{16} & -\frac{85}{12} & \frac{1}{4} \\
 & \frac{59}{48} & -\frac{17}{96} & \frac{225}{32} & \frac{85}{12} & 0
\end{array}
$$

Implicit midpoint rule

$$
\begin{array}{c|c}
\frac{1}{2} & \frac{1}{2} \\
\hline
 & 1
\end{array}
$$

Implicit Euler

$$
\begin{array}{c|c}
1 & 1 \\
\hline
 & 1
\end{array}
$$

A.4.3 ESDIRK

Implicit trapezoidal rule

$$
\begin{array}{c|cc}
0 & & \\
1 & \frac{1}{2} & \frac{1}{2} \\
\hline
 & \frac{1}{2} & \frac{1}{2}
\end{array}
$$

ESDIRK43

$$
\begin{array}{c|cccccc}
1 & & & & & & \\
\frac{1}{2} & \frac{1}{4} & \frac{1}{4} & & & & \\
\frac{2-\sqrt{2}}{4} & \frac{1-\sqrt{2}}{8} & \frac{1-\sqrt{2}}{8} & \frac{1}{4} & & & \\
\frac{5}{8} & \frac{5-7\sqrt{2}}{64} & \frac{5-7\sqrt{2}}{64} & \frac{7\left(1+\sqrt{2}\right)}{32} & \frac{1}{4} & & \\
\frac{26}{5} & \frac{-13796-54539\sqrt{2}}{125000} & \frac{-13796-54539\sqrt{2}}{125000} & \frac{506605+132109\sqrt{2}}{437500} & \frac{166\left(-97+376\sqrt{2}\right)}{109375} & \frac{1}{4} & \\
1 & \frac{1181-987\sqrt{2}}{13782} & \frac{1181-987\sqrt{2}}{13782} & \frac{47\left(-267+1783\sqrt{2}\right)}{273343} & \frac{-16\left(-22922+3525\sqrt{2}\right)}{571953} & \frac{-15625\left(97+376\sqrt{2}\right)}{90749876} & \frac{1}{4} \\
\hline
 & \frac{1181-987\sqrt{2}}{13782} & \frac{1181-987\sqrt{2}}{13782} & \frac{47\left(-267+1783\sqrt{2}\right)}{273343} & \frac{-16\left(-22922+3525\sqrt{2}\right)}{571953} & \frac{-15625\left(97+376\sqrt{2}\right)}{90749876} & \frac{1}{4} \\
 & \hat{b}_1 & -\frac{480923228411}{4982971448372} & \frac{6709447293961}{12833189095359} & \frac{3513175791894}{6748737351361} & -\frac{498863281070}{6042575550617} & \frac{2077005547802}{8945017530137}
\end{array}
$$

with $\hat{b}_1 = 1 - \sum_{i=2}^{n} \hat{b}_i$.

A.4.4 ROW

GRK4A

$$\begin{array}{c|cccc}
0 & & & & \\
0.438 & 0.438 & & & \\
0.796920457938 + 0.0730795420615 & 0.796920457938 & 0.0730795420615 & & \\
0.796920457938 + 0.0730795420615 & 0.796920457938 & 0.0730795420615 & 0 & \\
\hline
 & 0.199293275701 & 0.482645235674 & 0.0680614886256 & 0.25 \\
 & 0.346325833758 & 0.285693175712 & 0.367980990530 & 0
\end{array}$$

$$\gamma = \begin{array}{cccc}
0.395 & & & \\
-0.767672395484 & 0.395 & & \\
-0.851675323742 & 0.522967289188 & 0.395 & \\
0.288463109545 & 0.0880214273381 & -0.337389840627 & 0.395
\end{array}$$

GRK4T

$$\begin{array}{c|cccc}
0 & & & & \\
0.462 & 0.462 & & & \\
-0.0815668168327 + 0.961775150166 & -0.0815668168327 & 0.961775150166 & & \\
-0.0815668168327 + 0.961775150166 & -0.0815668168327 & 0.961775150166 & 0 & \\
\hline
 & 0.217487371653 & 0.486229037990 & 0 & 0.296283590357 \\
 & -0.717088504499 & 1.77617912176 & -0.0590906172617 & 0
\end{array}$$

$$\gamma = \begin{array}{cccc}
0.231 & & & \\
-0.270629667752 & 0.231 & & \\
0.311254483294 & 0.00852445628482 & 0.231 & \\
0.282816832044 & -0.457959483281 & -0.111208333333 & 0.231
\end{array}$$

A.5 ILUT solution times 3D steady-state

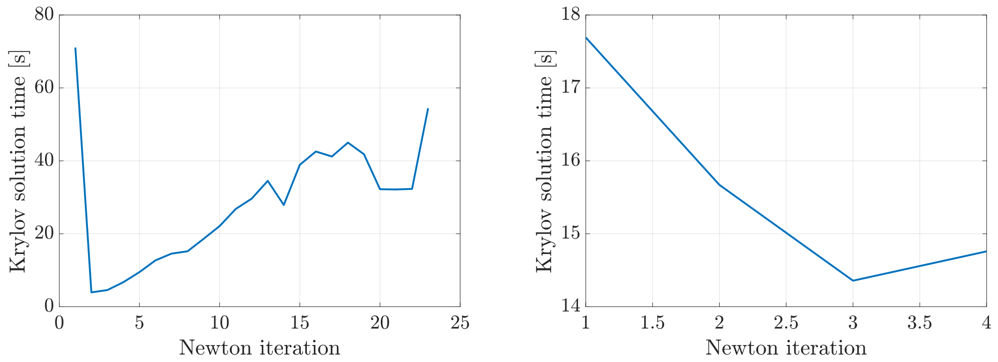

(a) Krylov solution times per Newton iteration using ILUT for high carrier densities.

(b) Krylov solution times per Newton iteration using ILUT for low carrier densities.

Figure A.1: Krylov solution times for a 3D steady-state example.

A.6 Additional transient simulation results

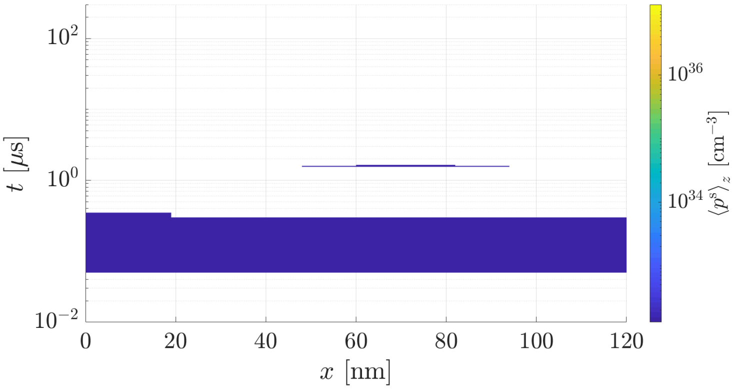

Figure A.2: Same simulation as in sec. 7.3.2 with explicit Cash-Karp method. $h = 50\,\text{ns} = \text{const.}$.

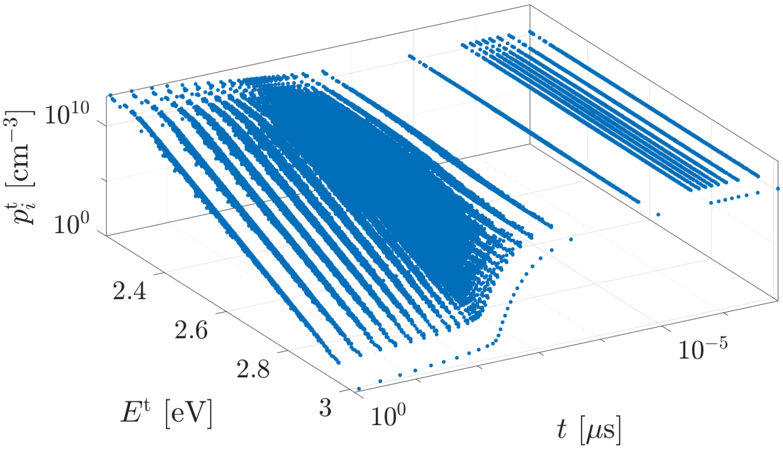

Figure A.3: Transient simulation on a homogeneous grid with all decay and source mechanisms deactivated. Initial value was $p_i = 10^{10}\,\text{cm}^{-3}$ everywhere with subsequent exciton motion resulting in a distribution similar to the expected Bose-Einstein distribution.

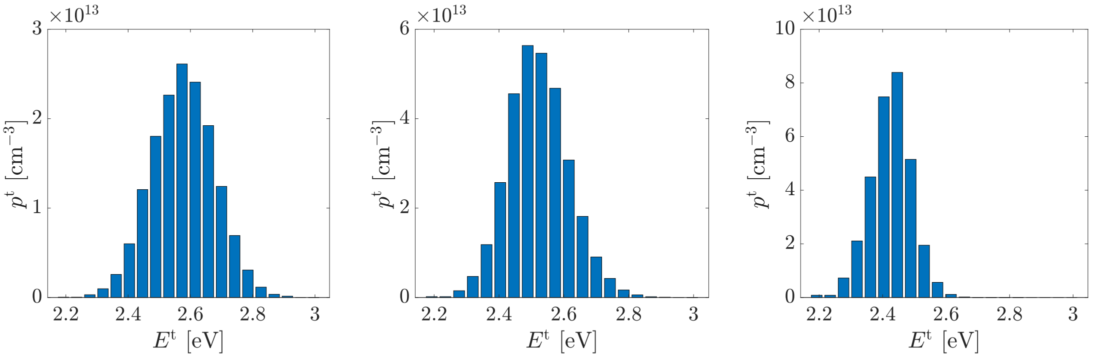

(a) $t = 0\,\mu\text{s}$. **(b)** $t = 1 \times 10^{-4}\,\mu\text{s}$. **(c)** $t = 4 \times 10^{-4}\,\mu\text{s}$.

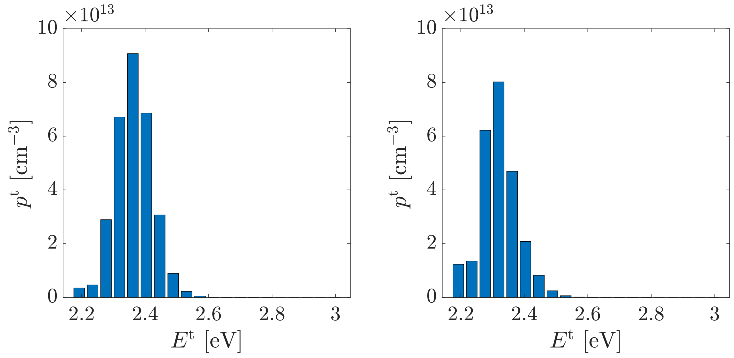

(d) $t = 6 \times 10^{-3}\,\mu\text{s}$. **(e)** $t = 0.9\,\mu\text{s}$.

Figure A.4: Transient evolution of the triplet density over triplet energy. The Gaussian form is approximately maintained.